Department of Precision and Microsystems Engineering

The Dynamics of Floating Ring Bearings used in Automotive Turbochargers

Name:	Roel Visser

Report no:	EM 11.019
Coach:	dr. ir. D. de Klerk
Professor:	prof. ir. D.J. Rixen
Specialisation:	Engineering Mechanics
Type of report:	Masters Thesis
Date:	Delft, June 10, 2011

The Dynamics of Floating Ring Bearings used in Automotive Turbochargers

MSc. Thesis

R.J. Visser BSc.
R.J.Visser@student.tudelft.nl

Delft University of Technology
Faculty of Mechanical, Maritime and Materials Engineering
Section Engineering Mechanics
Delft, The Netherlands

Almere, The Netherlands

June 10, 2011

Abstract

The use of turbochargers in passenger vehicles is becoming more and more popular due to downsizing of engines. One of the quality criteria for a turbocharger is a low noise level; noise which originates from the vibrations of the turbocharger. To investigate the sources and levels of the noise a parametrized model is wanted which can be used for the analysis of its dynamic behavior. In this thesis the focus has been laid on the hydrodynamic radial bearings, so called floating ring bearings (FRBs).

The influences included in the numerical model are the forces originating from the pressure distribution in the oil films, viscous forces, gravity and unbalance of the turbine rotor system. The calculation of the pressure distribution in the two oil films is based on the short length bearing Reynolds equation. Thermal influences other than the influence on oil viscosity are not taken into account. A demonstrator has been designed and fabricated which allows measurement of shaft motion and FRB rotation speed. The demonstrator is used to compare the results of measurements with the demonstrator with numerical simulations of the demonstrator to validate the numerical FRB model.

A numerical model is evaluated where the shaft is simulated as a point mass. Results of this model show whirling behavior of the shaft and floating ring and also a jump which indicates a change of mode shape of the system. This jump and whirling behavior is also seen in measurements of turbocharger shaft motion. Although this is a different system which makes this simulation and the measurement incomparable, it does confirm that the subsynchronous vibrations which have been measured originate from the bearing system of the turbocharger. A sensitivity analysis has been performed to investigate the influence of different FRB parameters on the dynamic behavior. This analysis showed that the whirl and floating ring rotational frequencies were only affected for a minor amount. The jump frequency appears to be the most sensitive to changes in bearing configuration.

Experiments have been performed using a demonstrator. Controllable shaft speeds up to 40.000 RPM have been achieved with the demonstrator. The results of simulation and measurements do not match, but the shape of the measured shaft motion shows odd behavior which may indicate that the demonstrator is far from the ideal situation which has been simulated. The measurement concept for measuring ring rotational speed has been validated and floating ring rotational speeds of up to 27% of the shaft rotational speed have been measured. The measured floating ring rotational speed showed to be non-monotonic.

Although the numerical model has not been validated by the demonstrator simulation and measurements, the point mass simulation does show behavior which is also seen in the results of turbocharger shaft motion measurements. The origin of the whirl frequencies has been identified and jumping behavior is seen in both the model and turbocharger shaft motion measurements.

Acknowledgments

After I got my BSc degree it was not hard for me to choose a MSc track; it was clear for me that I had a preference for dynamics. When I had to choose a final MSc project and this project was offered, a nice challenge was presented to me. It was a real project, things were done which were not done before. The skills learned the past few years were put to the test, but I have also learned a lot. I have not only learned more academic skills, but also manufacturing skills during the build of the test setup.

I want to thank everybody who helped me and contributed to my project, especially Rob, who kept my mind sharp, and Robin for helping me out greatly during the build of the test setup. Not to forget, I want to thank the friends I have made at MEE for making it a great time!

Thesis outline

This section gives an overview of the structure of this thesis.

Chapter 1 In the first chapter of this thesis the reader will be introduced to the topic of this research. The context of the research will be explained to answer the question why it has been done. Furthermore the goals and scope are treated.

Chapter 2 The physics which have been taken into account in the model of the floating ring bearing are discussed in this chapter. The mathematical background of the physical effects and the way this has been implemented in Matlab are presented.

Chapter 3 A demonstrator has been designed and built to validate the theoretical floating ring bearing model. The design of this test setup and its measurement points are presented.

Chapter 4 The results of simulations and experiments are shown in this chapter. The first simulation results are from a simulation where a situation with constant shaft rotational speed has been simulated. This simulation is done to validate the model. Secondly, a simulation of the floating ring bearing with the shaft modeled as a point mass is performed. The third simulation is a simulation of the test setup presented in chapter three and the results of the measurements are shown in section four. A comparison between a turbocharger shaft motion measurement and the shaft as point mass simulation and a comparison between the theoretical and experimental demonstrator results are presented and the chapter closes with a sensitivity analysis using the shaft as point mass model.

Chapter 5 In the final chapter the conclusions of the research are summed up and suggestions for further research are given.

Contents

1 Introduction **1**

1.1 The working principle of a turbocharger 3

1.2 Research context 4

1.3 Turbocharger bearings 5

1.4 Goals and scope of this research 7

1.5 Literature on Floating Ring Bearings 9

1.6 Coordinates, parameters and variables used throughout this thesis 10

2 Modeling the floating ring bearing **13**

2.1 Modeling steps for time integration 15

2.2 FRB model 17

2.2.1 Dynamics in translational direction 17

2.2.2 Dynamics in rotational direction 22

2.3 Thermal aspects 24

2.4 Implementation in Matlab 25

2.4.1 Implementation of the physics in Matlab 25

2.4.2 Time step control of the ODE solver 28

2.4.3 Calculation of waterfall plots 28

3 **Experimental approach** **31**

3.1 Demonstrator design 33

3.2 Test setup 36

4 **Results and discussion** **39**

4.1 Model verification 41

4.2 Point mass simulation 46

4.2.1 Waterfall plots 46

4.2.2 Body displacement and velocity 50

4.2.3 Peak pressure development and fluid film forces 53

4.3 Demonstrator simulation 56

4.3.1 Demonstrator model 56

4.3.2 Waterfall plots 59

4.3.3 Body displacement and velocity 59

4.3.4 Peak pressure development and fluid film forces 63

4.3.5 Comparison with the point mass simulation 64

4.4 Experimental results 65

4.4.1 Motion analysis 65

4.4.2 Frequency content analysis 69

4.5 Results discussion 74

4.5.1 Comparison: Point mass simulation and turbocharger measurements 74

4.5.2 Comparison: Theoretical and experimental demonstrator results 76

4.6 Sensitivity analysis 80

5 **Conclusions and recommendations** **83**

5.1 Conclusions 85

5.2 Recommendations 85

A Turbocharger nomenclature **91**

A.1 Turbo nomenclature 93

A.2 Cartridge nomenclature 95

A.3 Floating ring geometry nomenclature 96

B Modeling details **97**

B.1 Journal bearing nomenclature 99

B.2 Fluid film forces 99

B.2.1 The fluid film pressure equation 100

B.2.2 Forces acting on the journal 101

B.3 Forces in and on the floating ring bearing 102

B.3.1 Pressure film force 102

B.3.2 Gravitational force 103

B.3.3 Unbalance force 103

B.3.4 Viscous drag force 104

C Measurement equipment details **105**

D Theoretical modeling **109**

D.1 Demonstrator simulation FEM matrices 111

D.2 Sensitivity analysis waterfall plots 112

E Additional experimental results **117**

Nomenclature

Unless specified otherwise, the meaning of the symbols used in this thesis are listed in this section.

Symbol	Description	Unit
A	Area	m^2
C	Clearance	m
D	Bearing diameter	m
e	Eccentricity	m
$\mathbf{F}$	Force vector	-
FRB	Floating Ring Bearing	-
I_{zz}	Mass moment of inertia around the z-axis	kg m^2
L	Bearing width	m
$\mathbf{M}$	Mass matrix	-
p	Pressure	Pa
R	Radius	m
u	Translational speed	m/s
$\mathbf{u}$	Vector with degrees of freedom	-

Greek symbols

Symbol	Description	Unit
ϵ	Eccentricity	-
μ	Dynamic viscosity	Pa s
ω	Rotational speed	rad/s
τ	Shear stress	Pa
Θ	Angular degree of freedom	rad

Subscripts

Symbol	Description
a	Atmospheric
b	Bearing housing
g	Gravitational
i	Inner
o	Outer
r	Floating ring
s	Shaft
u	Unbalance
v	Viscous
x	X-direction
y	Y-direction

Chapter 1

Introduction

This chapter forms the introduction of this Master's thesis. The chapter starts with an introduction to turbochargers in section 1.1. In this section the working principle of a turbocharger is explained. The context in which this research is done is explained in section 1.2. The bearings which are used in turbochargers are discussed in section 1.3. In section 1.4, the goals of this research will be presented. Literature on the subject is summarized in section 1.5 and the first chapter ends with a description of the coordinate system and some of the parameter names used in this thesis.

1.1 The working principle of a turbocharger

Turbochargers have been around since the early 1900s and are used to increase the power output of a combustion engine. A turbocharger essentially consists of a compressor and a turbine on one shaft, as can be seen in figure 1.1. Hot gases which are formed by the combustion of fuel in the cylinders of the engine enter the turbocharger at the turbine side, drive the turbine and exit the turbocharger. Because the turbine is connected to the compressor, ambient air is sucked in at the compressor side. The air is compressed and is led to the air intake manifold of the engine. The compressed air contains more oxygen per volume, which can be used for combustion. This higher oxygen level can be used to increase the power output of a car. Turbochargers are also used in aviation, among other industries. Turbochargers in helicopters, for example, can compress air at high altitudes with lower atmospheric pressure to provide the necessary oxygen needed by the engine.

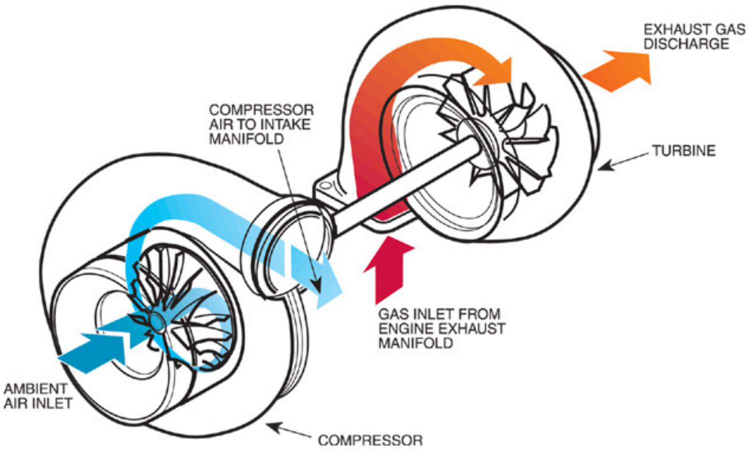

Figure 1.1: The working principle of a turbocharger [3]

In the automotive industries the use of turbochargers is becoming more and more popular. Due to the environmental trend, car manufacturers want to use engines with a lower cylinder volume, but they do not want to sacrifice power. By combining smaller engines with a turbocharger, energy which would otherwise would be lost can be reused and the power of the engine can be increased.

1.2 Research context

Passengers cars are designed to get users of it safely and comfortably from point A to B. Comfort contains many different aspects; the car should react well to road variations, there should be enough leg space, the noise should be as low as possible, etc.. In passenger cars noise is minimized for the comfort of the users and one of the sources of noise is the turbocharger. It is possible to adjust the design of the car and add damping in the transfer path from turbocharger to the cabin, but it is better to handle the problem at its source.

In the turbocharger vibrations originate from the rotor-bearing assembly. These vibrations are led to the cartridge[1], which in turn excites the air around it. The pulsating air is interpreted by the human ear as sound. At a certain point during the production of a turbocharger the vibrations of the cartridge are measured at predefined rotation speeds. The amplitude of the vibrations has to be below a certain level to be acceptable and serves as a measure of noise. If the amplitude is larger than the threshold value there is too much unbalance in the rotating parts of the cartridge. Unbalance of the rotor can be interpreted as a misalignment of the rotor axis of rotation and the center of mass of the rotor. The further the center of mass is from the axis of rotation, the more unbalance a rotor has. To lower the amplitude of the vibrations measured on the cartridge, material is removed from the rotor assembly to reduce the unbalance until the cartridge meets the vibration criteria. This process is called balancing.

A useful tool in identifying sources of noise in a turbocharger is the waterfall plot. In this plot the frequency content of the measured vibrations at different turbocharger operating speeds can be seen. A waterfall plot of a measurement of the acceleration levels of a complete turbocharger during run-up is shown in figure 1.2. The figure shows the frequency content of the vibrations of the turbocharger for a certain range of operation speeds. The waterfall plot can be divided in three frequency zones. For a specific operation speed, the synchronous frequency is the frequency which matches the operational speed of the turbocharger. For example, the synchronous frequency of 60.000RPM is $\frac{60.000}{60} = 1000\text{Hz}$. The subsynchronous frequency zone contains the frequencies of the vibration which are lower than the synchronous frequency and the supersynchronous frequency zone contains frequencies which are higher than the synchronous frequency. These frequency zones are visualized in figure 1.3.

In general, the three different frequency zones contain vibrations from three different sources. Vibrations in the synchronous zone are caused by the unbalance in the rotor of the turbocharger. Since the unbalance force originates in the

---

[1] Turbocharger nomenclature can be found in appendix A

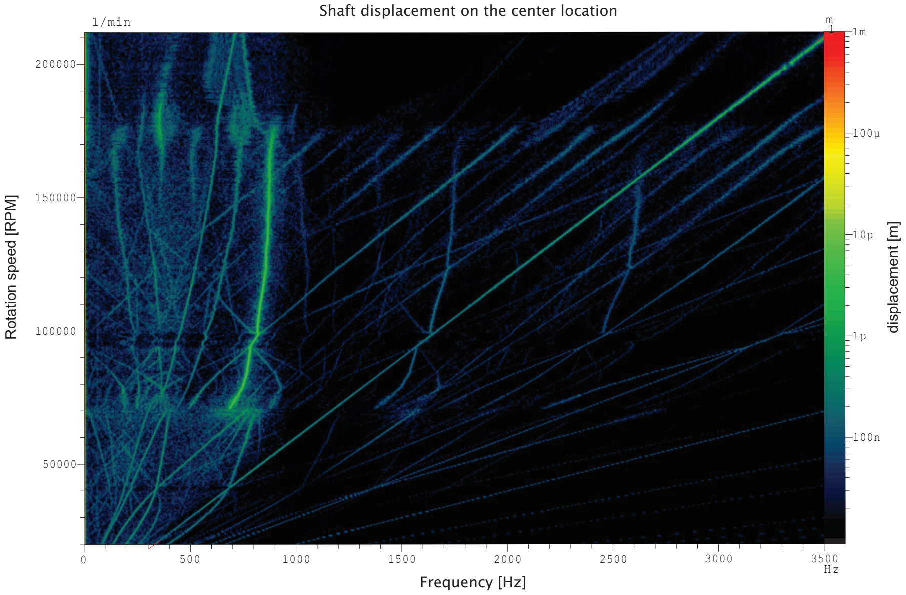

Figure 1.2: Waterfall plot of a vibration measurement of a turbocharger by Eling [1].

rotor it has the same frequency as the rotational speed of the rotor. The subsynchronous noise originates from the bearing system. It is caused by instabilities of the oil films in the thin film bearings [14]. The supersynchronous vibrations can be caused by, for example, turbine pulsation. If the turbine wheel has 11 blades, it can be expected that a vibration of 11 times the rotational frequency will be measured due to the amount of pulses on the turbine wheel during one rotation of the rotor.

An accurate parametrized model of a turbocharger is desired to be able to predict the behavior of turbochargers. In the design phase changes to e.g. geometry and lubricant properties can be simulated to see which effect they have on the dynamic behavior of the turbocharger. Simulation can aid in improving the quality and characteristics of the turbocharger, which in turn may improve the reputation of the manufacturer.

1.3 Turbocharger bearings

Turbocharger manufacturers can use different bearing concepts to support the turbocharger rotor. Because of the high rotational speeds of turbochargers, which can be well over 200.000 RPM, the most common method of supporting the rotor is using thin film fluid bearings. The main reason for using these kind of bearings is the low cost. Figure 1.4 shows two types of thin film fluid bearings; the journal bearing and the floating bearing. As can be seen, the

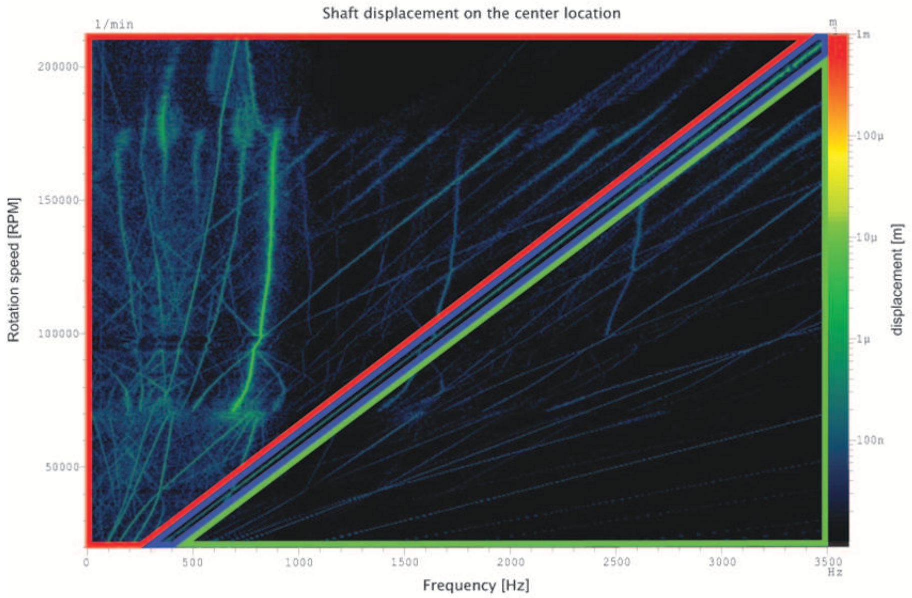

Figure 1.3: Frequency zones in a waterfall plot. Blue: Synchronous, Red: Subsynchronous, Green: Supersynchronous

difference is that the floating bearing has an intermediate sleeve or ring which causes the bearing to have two lubricant films. The floating bearing can thus be a floating ring bearing $\left(\frac{L}{D} < 1\right)$ or a floating sleeve bearing $\left(\frac{L}{D} > 1\right)$. In this thesis floating ring bearings are treated.

In high-speed operation, overheating of journal bearings can be a problem. This problem can be countered by increasing the clearance between the shaft and bearing house, so the oil flow can be increased. This in turn leads to a higher cooling capacity. Increasing the clearance has negative effects, like a decreased load-carrying capacity and increased sensitivity for oil whirl, which is an orbital movement of the shaft in the oil film [11, 12]. Shaw [15] compares the characteristics of journal bearings and floating bearings. He observes that floating bearings have a better cooling capacity and generate less heat than equivalent journal bearings. The speed of the floating ring or sleeve depends mainly on the ratio of the radii of the different components and the ratio of the clearances.

Figure 1.5 shows the inside of a cartridge. The cartridge contains three bearings; two radial bearings and one axial bearing. The radial bearings provide a low friction support of the shaft. The axial bearing protects the rotor against shocks and prevents the rotating parts from making physical contact with its housing. Pressurized lubricant enters the bearing house and flows to the three bearings. In case of the radial bearings, the lubricant is distributed to the inner film through the holes in the floating rings. Figure 1.6 shows a cross section of the radial bearing, showing the connection between inner and outer film. The working principle of the floating ring bearing relies on pressure build up of the two lubricant films due to the relative motion of the solid parts of the bearing.

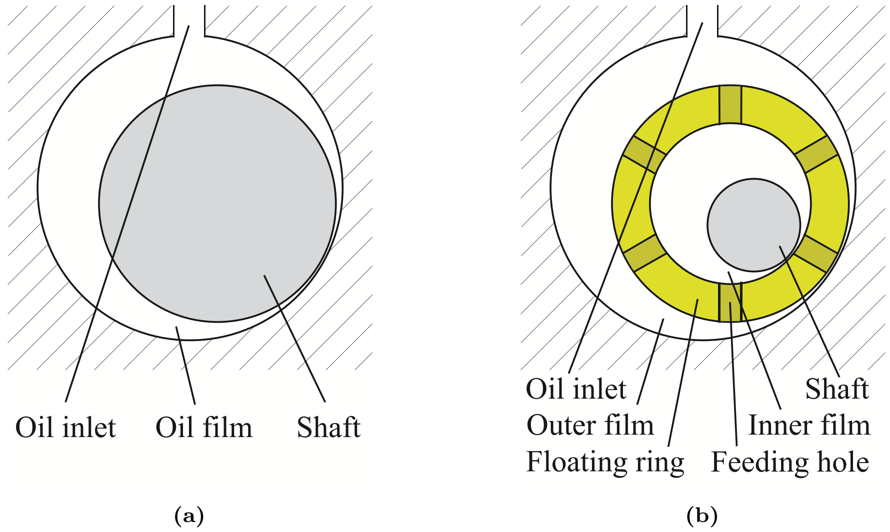

(a) **(b)**

Figure 1.4: Journal bearing (left) and floating bearing (right). Dimensions are not to scale for display purposes.

Under normal operation the ring nor the shaft makes physical contact with another solid part.

1.4 Goals and scope of this research

To create understanding of the dynamics in a turbocharger, the SIM-T (Silence in Mitsubishi Turbochargers) project has been started at Mitsubishi Heavy Industries Equipment Europe (MEE). The goal of this project is to create understanding of turbocharger dynamics by creating a theoretical model of a turbocharger and by performing experiments to identify the dynamic behavior. A global overview of the SIM-T project can be seen in figure 1.7. By using the results gained from simulations and experiments, information is obtained about the turbocharger dynamics and can be used to create a better product and better support to the customers of MEE.

As mentioned in section 1.2, turbocharger behavior may be improved if the design engineers would have tools to simulate the turbocharger dynamic behavior. Eling [1] simulated the rotor of a turbocharger and determined the eigenfrequencies and mode shapes of a specific turbocharger. One of the aspects which can improve his model is to replace the simple bearing model he used with a more realistic bearing model. The goal of the research discussed in this thesis is to

create a more realistic floating ring bearing model to simulate the dynamic behavior of floating ring bearings.

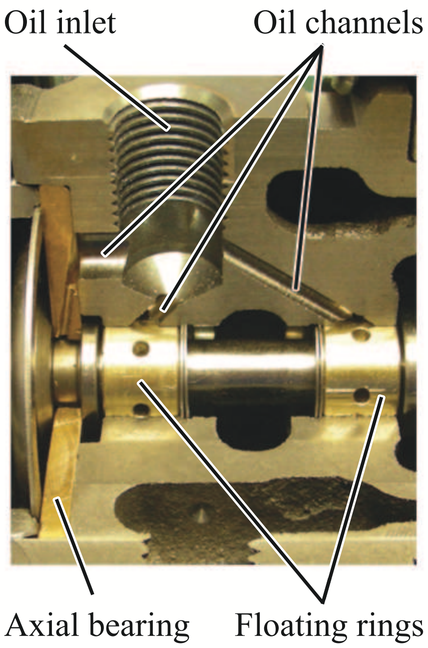

Figure 1.5: The turbocharger bearing system

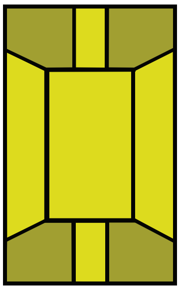

Figure 1.6: Schematic bearing cross section

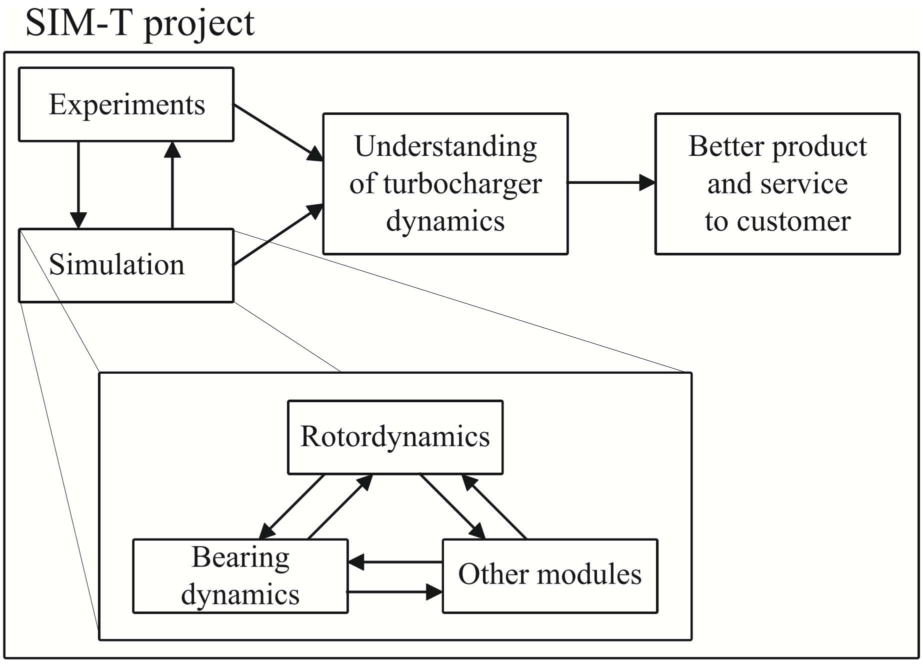

Figure 1.7: Overview of the SIM-T project

By focusing on short length bearings, with a length to diameter ratio which is smaller than one, assumptions are made which make the computations less complex but also make them unsuitable for simulation of floating sleeve bearings. In this thesis the temperature effects, which may be an influential variable, are not taken into account. The only influence of temperature which is included in the bearing model is the effect of temperature on oil viscosity. The feeding holes in the floating ring have the function to supply the inner oil film with oil. An effect which may occur is "communication" between the inner and outer oil films; the pressure in the oil film on one side of the feeding hole may influence the pressure in the oil film on the other side of the feeding hole. This effect is not taken into account, the two oil films are independent of each other.

A test setup is created to measure the bearing behavior. To verify the model, the results of the measurements are compared to a finite element model of the test setup.

1.5 Literature on Floating Ring Bearings

Journal bearings and floating ring bearings have been a subject of research for many years. In 1947, Shaw and Nussdorfer [15] described the characteristics of a full-floating sleeve bearing and compared it with an equivalent journal bearing. They observed that the characteristics of the full-floating bearing are mainly dependent of the ratio of the clearances and the ratio of radii of the components.

Compared to an equivalent journal bearing, the full-floating bearing generates less heat.

Modeling of the thermal behavior has proven to be essential for accurate FRB behavior simulation. The temperature of the inner and outer film may differ from each other and the temperature may even be non-constant within a film. Since temperature influences the viscosity and clearances of the bearing, it is imaginable that the behavior of the FRB is dependent of temperature. Trippett and Li [16] compared measurement data of the rotational speed of the floating ring of a FRB with an isothermal and a thermal model. The results show that the floating ring speed increases linearly with shaft speed when an isothermal model is used. The measurement data shows that this is not true; the ring speed becomes almost constant when the shaft speed is increased. Finite element modeling of a FRB shows that the temperature in the inner film is higher than in the outer film and that the temperature in the middle of the oil film is lower than when the oil exits the bearing [4].

Eling [1] describes the structural dynamics of a turbocharger. The different mode shapes of the turbocharger rotor are described and concluded that the rotor vibrations in the radial direction contribute the most to the noise generated by a turbocharger; axial and torsional vibrations of the rotor are of minor importance. Schweizer [14] mentions in his article how the radial vibration modes are excited. Schweizer describes how instabilities of the inner and outer oil films may excite the different mode shapes of the turbocharger rotor.

1.6 Coordinates, parameters and variables used throughout this thesis

An overview of the coordinates, parameters and variables used in this thesis is shown in figure 1.8. The dimensions are not to scale because of display purposes. The legend for figure 1.8 can be found in table 1.1.

The coordinate system used is a right-handed coordinate system with the x-direction pointing down, the y-direction pointing to the right and the z-axis coming out of the paper. The origin of the system is located in the center of the bearing housing.

The location of the center of the shaft is defined by $e_{x,s}$ and $e_{y,s}$, while the center of the ring is located at the coordinates $e_{x,r}$ and $e_{y,r}$. All units are according to the SI unit standard, with the exception being the unit revolutions per minute (RPM) for the rotational speeds of the turbocharger rotor and the floating ring. RPM is commonly used in daily life and the automotive industry.

A nomenclature list of all symbols and its units used throughout this thesis can be found on page ix.

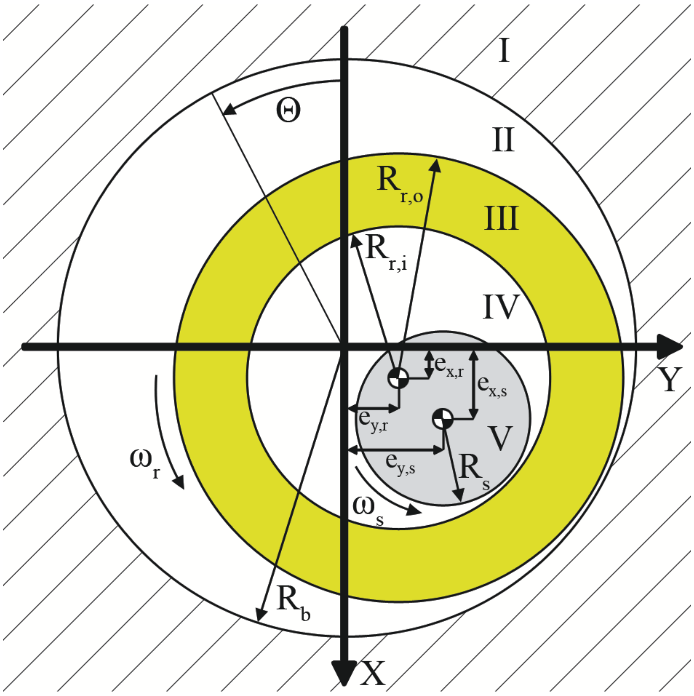

Figure 1.8: An overview of the coordinates, parameters and variables used in this thesis

Table 1.1: Legend to figure 1.8

I	Bearing housing
II	Outer oil film
III	Floating ring
IV	Inner oil film
V	Rotating shaft
$e_{x,r}$	Displacement of the ring in x-direction
$e_{y,r}$	Displacement of the ring in y-direction
e_{x_s}	Displacement of the shaft in x-direction
$e_{y,s}$	Displacement of the shaft in y-direction
R_b	Bearing housing radius
$R_{r,o}$	Outer ring radius
$R_{r,i}$	Inner ring radius
R_s	Shaft radius
ω_s	Shaft rotational speed
ω_r	Ring rotational speed

Chapter 2

Modeling the floating ring bearing

In the previous chapter an introduction to this research has been given. To improve the current turbocharger model and create more understanding of turbocharger dynamics, a better floating ring bearing model is needed. This chapter describes how the floating ring bearing is modeled. Section 2.1 globally describes which steps are taken by the model to perform time integration. In section 2.2 the dynamic equations used in the model are derived. Section 2.3 describes the thermal influences which have been taken into account. How the model is implemented in Matlab is described in section 2.4.

2.1 Modeling steps for time integration

To integrate the non-linear bearing behavior over time, several calculation steps are made. This section describes these steps.

Parameters
At the start of the integration of a time step the parameters are loaded. Figure 2.1 shows the physical parameters needed as input for the simulation.

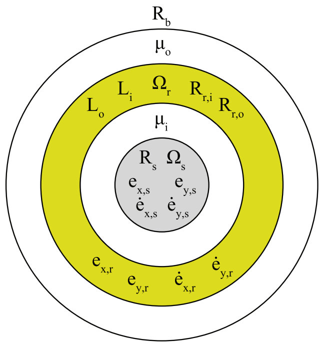

Figure 2.1: Model parameters

Calculate the pressure profiles
The first calculation step of the integration is the calculation of the pressure profiles in the inner and outer lubricant films. These pressure films exert forces on the shaft and floating ring which can be calculated by integrating the pressure film over the area it is working on.

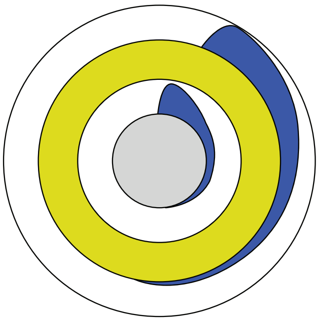

Figure 2.2: Pressure distribution in the oil films

Numerical integration
The system of equations is described by the mass matrix **M** and the force vector **F**, which contains all external forces, for example the forces originating from the oil film pressure. The components of the force vector may be dependent of displacement $\mathbf{u}(\mathrm{t})$, velocity $\dot{\mathbf{u}}(\mathrm{t})$ and shaft and floating ring rotational speeds $\omega_s(\mathrm{t})$ and $\omega_r(\mathrm{t})$.

$$\mathbf{M}\ddot{\mathbf{u}}(\mathrm{t}) = \mathbf{F}(\mathbf{u}(\mathrm{t}), \dot{\mathbf{u}}(\mathrm{t}))$$

Results
The integration of the set of equations yields a new configuration of the system, i.e. new positions and speeds of the shaft and floating ring. This new configuration serves as initial condition for the next time step. For the next time step the process is repeated.

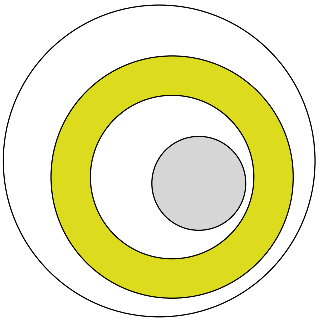

Figure 2.3: The new calculated configuration of the FRB

2.2 FRB model

This section describes the modeling of the FRB. The description of the model is split up in two parts; 2.2.1 describes the translational dynamics, while section 2.2.2 describes the rotational dynamics of the floating ring.

2.2.1 Dynamics in translational direction

The pressure distribution in the fluid films of a floating ring bearing can be calculated by using equation 2.1, in which Δe_x, Δe_y, $\Delta \dot{e}_x$, $\Delta \dot{e}_y$ and $\Delta\omega$ are time-dependent and are respectively the relative displacement in x- and y-direction, the relative velocity in x- and y-direction and the relative rotational speed of the inner body compared to the outer body. For example, $\Delta e_x = e_{x,\text{inner body}} - e_{x,\text{outer body}}$.

$$p\left(\Theta,z,t\right) - p_a = 6\mu \frac{\left(\Delta\dot{e}_x + \Delta e_y \frac{\Delta\omega}{2}\right)\cos\Theta + \left(\Delta\dot{e}_y - \Delta e_x \frac{\Delta\omega}{2}\right)\sin\Theta}{\left(C + \Delta e_x \cos\Theta + \Delta e_y \sin\Theta\right)^3}\left(z^2 - \left(\frac{L}{2}\right)^2\right) \tag{2.1}$$

Equation 2.1 is derived from the Reynolds equation. The derivation can be found in appendix B.2. Using this equation, the pressure distributions in the inner and outer film can be calculated. When calculating the pressure distribution in the outer film, the floating ring can be considered as the inner body while the bearing housing can be considered as the outer body. Because the bearing housing is considered as fixed, the displacement, velocity and rotational speed of the outer body equal zero. This leads to equation 2.2.

$$p_{out}\left(\Theta,z,t\right) - p_a = 6\mu_o \frac{\left(\dot{e}_{x,r} + e_{y,r}\frac{\omega_r}{2}\right)\cos\Theta + \left(\dot{e}_{y,r} - e_{x,r}\frac{\omega_r}{2}\right)\sin\Theta}{\left(C_o + e_{x,r}\cos\Theta + e_{y,r}\sin\Theta\right)^3}\left(z^2 - \left(\frac{L_o}{2}\right)^2\right) \tag{2.2}$$

For the calculation of the inner film pressure distribution the rotating shaft is considered as the inner body, while the floating ring is considered as the outer body and both can have non-zero valued displacements, velocities and rotational speeds. This results in equation 2.3 for calculating the pressure distribution in the inner film.

$$\begin{aligned} p_{in}\left(\Theta,z,t\right) - p_a = 6\mu_i &\left[\frac{\left(\left(\dot{e}_{x,s} - \dot{e}_{x,r}\right) + \left(e_{y,s} - e_{y,r}\right)\frac{\omega_s - \omega_r}{2}\right)\cos\Theta}{\left(C_i + \left(e_{x,s} - e_{x,r}\right)\cos\Theta + \left(e_{y,s} - e_{y,r}\right)\sin\Theta\right)^3} + \right. \\ &\left. \frac{\left(\left(\dot{e}_{y,s} - \dot{e}_{y,r}\right) - \left(e_{x,s} - e_{x,r}\right)\frac{\omega_s - \omega_r}{2}\right)\sin\Theta}{\left(C_i + \left(e_{x,s} - e_{x,r}\right)\cos\Theta + \left(e_{y,s} - e_{y,r}\right)\sin\Theta\right)^3}\right]\left(z^2 - \left(\frac{L_i}{2}\right)^2\right) \end{aligned} \tag{2.3}$$

As can be seen in the pressure distribution equations, the pressure distribution is dependent of

- displacement ($e_{x,s}$, $e_{y,s}$, $e_{x,r}$, $e_{y,r}$),
- translational speed ($\dot{e}_{x,s}$, $\dot{e}_{y,s}$, $\dot{e}_{x,r}$, $\dot{e}_{y,r}$),
- rotational speed (ω_s, ω_r),
- geometry (L_i, L_o, C_i, C_o) and
- lubricant viscosity ($\mu_i\left(T_i\right), \mu_o\left(T_o\right)$).

Because the pressure distribution is dependent of both displacement and velocity, it contains stiffness and damping properties. An example of a pressure profile which may be obtained by evaluation of equations 2.2 and 2.3 is shown in figure 2.4. This figure shows a pressure profile which contains both positive and negative pressures. When the pressure drops below zero, it is assumed that cavitation occurs; a phase transition of the oil from a fluid state to a vapor state. In reality the pressure in the cavitated region can not be lower than vacuum, but because the pressure in the fluid region of the oil film are expected to be much larger than vacuum the pressure in the cavitated region is set to zero. This means that the cavitated region of the pressure film will not provide any supporting force.

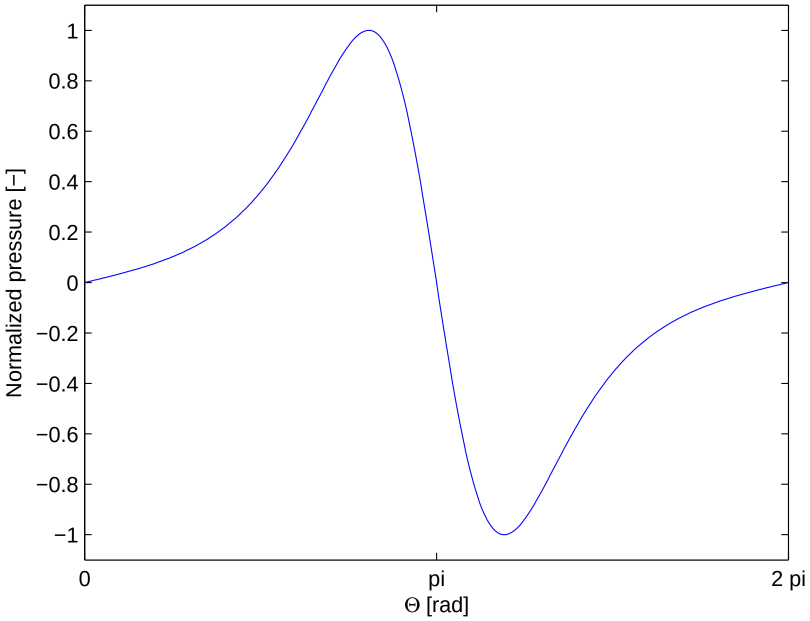

Figure 2.4: Example of the shape of the pressure profile in an oil film

Besides the effect on the oil film pressure, cavitation also affects the viscous drag which acts between the shaft and floating ring and the floating ring and bearing housing. Since the vaporized oil has a significantly lower viscosity than the fluid oil, the assumption is made that the viscous drag is only caused by the part of the oil film which is in fluid state. The viscous drag will contribute in a small amount to the forces in translational direction, but is the main force which causes the floating ring to rotate. The rotational dynamics concerning the floating ring will be discussed in section 2.2.2.

In the following paragraphs the properties of the oil films and the forces present in the floating ring bearing will be described. For details on these properties and forces, appendices B.2 to B.3 can be consulted.

Pressure film force

The pressure distribution functions can be integrated with respect to area to obtain the force caused by the film pressure. This results in the forces $F_{x,s,p}$ and $F_{y,s,p}$ working on the shaft and the forces $F_{x,r,p}$ and $F_{y,r,p}$ working on the floating ring.

The three time-dependent variables which influence the pressure distribution, influence it in a different way. To illustrate this, the pressure profile in three situations has been simulated. In all situations the inner body has a displacement unequal to zero. In addition, in the first situation the inner body has a rotational speed, in the second situation a speed in radial direction and in the third situation the inner body has a tangential speed. An overview of the different situations is shown in table 2.1. The resulting pressure profiles are shown in figure 2.5.

Table 2.1: Overview of the properties of the simulated situations shown in figure 2.5

Situation	e_x	e_y	$\dot{e}_x$	$\dot{e}_y$	ω
Pure rotational speed	> 0	0	0	0	> 0
Pure radial speed	> 0	0	> 0	0	0
Pure tangential speed	> 0	0	0	> 0	0

Since $e_x > 0$ and $e_y = 0$, the smallest gap between the inner and outer body is located at $\Theta = \pi$. The figure shows that in the case of pure rotational speed, the pressure distribution is only non-zero for $\Theta < \pi$. This results in a force which is roughly in the same direction as the rotational direction of the shaft. When the shaft only has a radial speed, a force is generated in the opposite direction of the speed. This is also the case when the shaft only has a tangential speed; this generates a force which is roughly in the opposite direction of the speed. Summarizing,

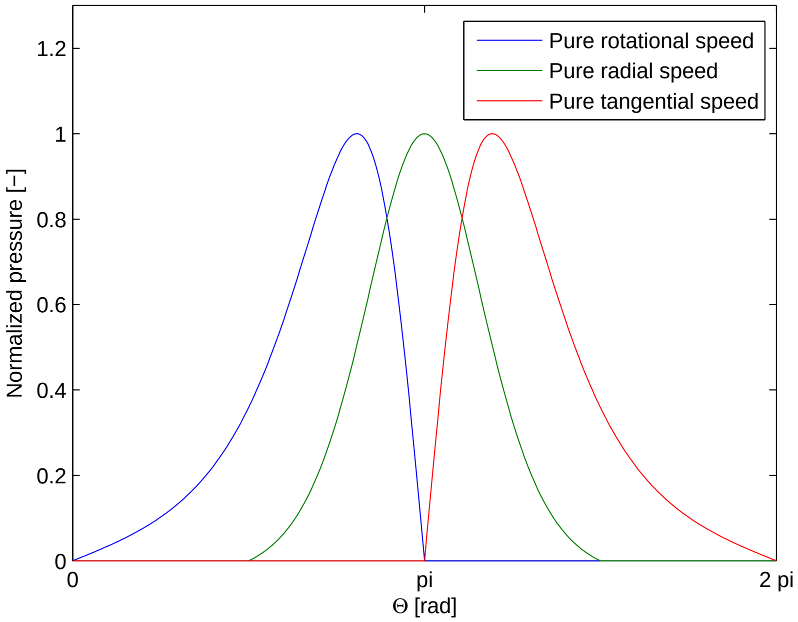

Figure 2.5: Body position, velocity and rotational speed all influence the pressure film in a different way.

- rotation of the inner body relative to the outer body generates a driving force which induces motion of the inner body,
- radial speed of the inner body relative to the outer body generates a force which counters the relative radial motion of the inner body and
- tangential speed of the inner body relative to the outer body generates a force which counters the relative tangential motion of the inner body.

During operation the pressure distributions in the oil films are a combination of these three effects.

Gravitational force

Although of minor influence in translational direction, the gravitational effects of the shaft and floating ring are included. The gravitational forces work only in the x-direction and therefore has only two non-zero components; $F_{x,s,g}$ and $F_{x,r,g}$.

Unbalance force

Since it is almost impossible to perfectly balance the rotor assembly of a turbocharger, there will always be an unbalance residue. The amplitude of the force generated by the unbalance is a centrifugal force which is described by

$$|F_{s,u}| = mr\omega_s^2 \tag{2.4}$$

In this equation, mr represents the amount of unbalance and has a value in the order of $10^{-8}\text{kg} \cdot \text{m}$. This unbalance value may be very small, but with the high speeds a turbocharger can achieve, the amplitude of the force may reach approximately 15N at a turbocharger speed of 250.000RPM. Since unbalance has a fixed physical location within the rotor, the unbalance force direction rotates when the shaft rotates.

Viscous drag

The shear stress between two surfaces is described by equation 2.5 [17]. As can be seen in this equation, the shear stress depends on the viscosity, relative speed and gap between the two surfaces.

$$\tau\left(\Theta\right) = \mu \frac{du}{dh\left(\Theta\right)} \tag{2.5}$$

Integration of the shear stress over the area results in a force. The viscous shear force is a drag force, which means it works in one direction when looking at a surface in radial direction. In translational direction this results in forces which can act in both positive and negative directions, as can be seen in figure 2.6. The figure also shows another effect which is the result of cavitation. In the region where the oil pressure is below the vapor pressure p_v, the oil has turned from a fluid state to a vapor. Since the viscosity of the vapor is far lower than the fluid pressure, the viscosity is set to zero and the viscous drag forces in the vapor region are neglected.

$$\mu = \begin{cases} 0 & \text{when} \quad p\left(\Theta\right) < p_v \\ \mu\left(T\right) & \text{when} \quad p\left(\Theta\right) > p_v \end{cases} \tag{2.6}$$

System of equations

Now the forces which work on the floating ring and shaft are known, the system of equations regarding the translational dynamics can now be described by

$$\mathbf{M}\ddot{\mathbf{u}} = \underbrace{\mathbf{F_p}\left(\mathbf{u},\, \dot{\mathbf{u}},\, \omega\right)}_{\text{Pressure film}} + \underbrace{\mathbf{F_g}}_{\text{Gravity}} + \underbrace{\mathbf{F_u}\left(\omega\right)}_{\text{Unbalance}} + \underbrace{\mathbf{F_v}\left(\mathbf{u},\, \dot{\mathbf{u}},\, \omega\right)}_{\text{Viscous drag}} \tag{2.7}$$

The displacement vector $\mathbf{u}$ and mass matrix $\mathbf{M}$ are described by equations 2.8 and 2.9. The left hand side of the equation does not contain stiffness or damping terms. This is because the stiffness and damping forces of the oil films are already counted for in the pressure film force vector $\mathbf{F_p}$.

$$\mathbf{u} = \begin{bmatrix} e_{x,s} \\ e_{y,s} \\ e_{x,r} \\ e_{y,r} \end{bmatrix} \tag{2.8}$$

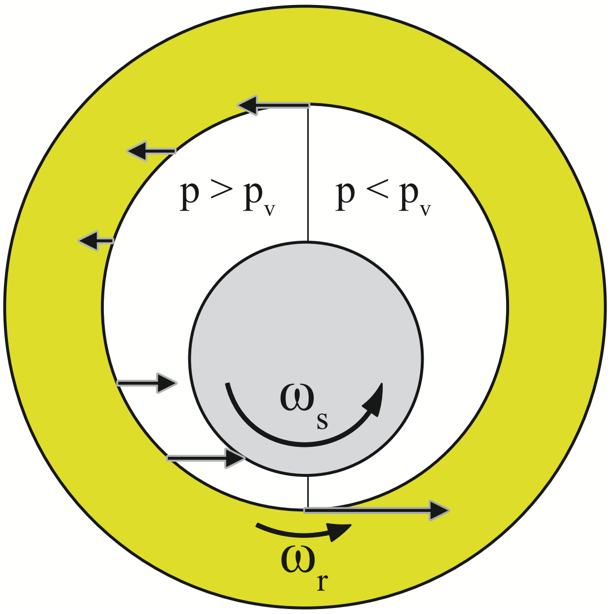

Figure 2.6: Amplitude and sign of horizontal viscous drag forces working on the inner surface of the floating ring. In the cavitated area ($p < p_v$) viscous drag forces are neglected.

$$\mathbf{M} = \begin{bmatrix} m_s & 0 & 0 & 0 \\ 0 & m_s & 0 & 0 \\ 0 & 0 & m_r & 0 \\ 0 & 0 & 0 & m_r \end{bmatrix} \tag{2.9}$$

2.2.2 Dynamics in rotational direction

In this section the dynamics in rotational direction are described. Because the shaft has a prescribed rotational speed, there is only one degree of freedom in rotational direction; the angle of the floating ring. The angle of the floating ring is not very interesting. The derivative of the angle, the rotational speed, is much more interesting and also influences the pressure distributions in the oil films. The floating ring rotates due to the torque generated by the shear force between the shaft and inner ring surface. The shear force between the outer ring and bearing housing surfaces counteracts the torque generated in the inner oil film. Recalling equations 2.5 and 2.6, the shear stress between two surfaces is given by

$$\tau\left(\Theta\right) = \mu \frac{du}{dh\left(\Theta\right)} \tag{2.5}$$

with

$$\mu(T,\Theta) = \begin{cases} 0 & \text{when} \quad p(\Theta) \leq 0 \\ \mu(T) & \text{when} \quad p(\Theta) > 0 \end{cases} \tag{2.6}$$

The average shear stress between two surfaces is

$$\bar{\tau} = du \frac{\int_0^{2\pi} \frac{\mu(T,\Theta)}{dh(\Theta)} d\Theta}{2\pi} \tag{2.10}$$

The shear force, or viscous drag force, can now be calculated by multiplying the average shear stress with the area it is working on. The force contributing to the viscous torque is visualized in figure 2.7. The torque generated by the viscous drag force is obtained by multiplying it with the radius it is working on.

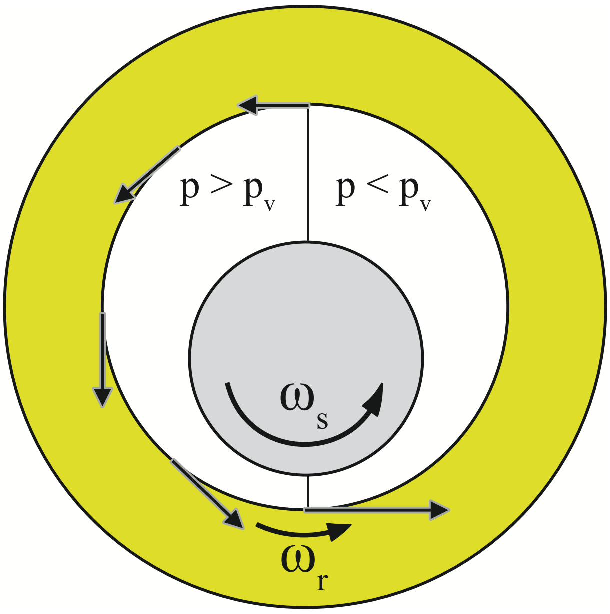

Figure 2.7: Viscous torque originates from viscous drag forces, which act tangential to the surface of the ring. Only the viscous torque in the inner oil film is shown in this figure.

$$F_v = A\bar{\tau} = 2\pi RL\bar{\tau} \tag{2.11}$$

$$M_v = RF_v = 2\pi R^2 L\bar{\tau} \tag{2.12}$$

Substitution of equation 2.10 in equation 2.12 and substituting appropriate expressions for du and $h(\Theta)$ leads to expressions of viscous torque on the inner and outer surfaces of the floating ring, respectively equations 2.13 and 2.14.

$$
\begin{aligned}
M_{i,v} =& R_{r,i}^2 L_i \mu_i \left(\omega_s R_s - \omega_r R_{r,i}\right) \cdot \ldots \\
& \int_0^{2\pi} \frac{1}{C_i + \left(e_{x,s} - e_{x,r}\right) cos\left(\Theta\right) + \left(e_{y,s} - e_{y,r}\right) sin\left(\Theta\right)} d\Theta
\end{aligned}
\tag{2.13}
$$

$$
M_{o,v} = -R_{r,o}^2 L_o \mu_o \omega_r R_{r,o} \int_0^{2\pi} \frac{1}{C_o + e_{x,r} cos\left(\Theta\right) + e_{y,r} sin\left(\Theta\right)} d\Theta \tag{2.14}
$$

Since the shaft will always have a higher rotational speed than the floating ring, the torque working on the inside of the floating ring always serves as a driving force which makes the floating ring rotate. The torque working on the outer surface of the floating ring always serves as a drag force, slowing the rotation of the floating ring down.

2.3 Thermal aspects

As mentioned in section 1.5, Trippett and Li [16] found that an isothermal model is not suitable for accurate predictions on the behavior of FRB's . The temperature dependence of the viscosity of a 5W-30 oil [2], a common motor oil, is shown in figure 2.8.

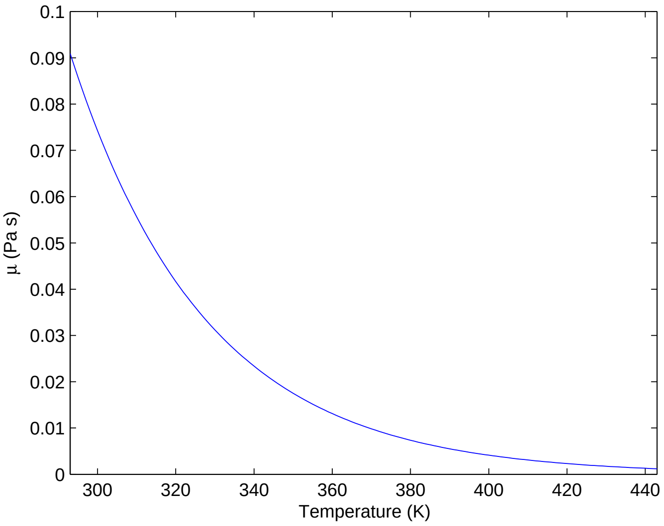

Figure 2.8: Temperature dependency of Mobil 1 5W-30 oil viscosity

Knoll et al. show the temperature distribution within a FRB with a finite element model.[4] The results show how the temperature changes in both radial and axial directions. As mentioned in section 1.4 an extensive thermal model is out of the scope of this thesis. Instead, only the oil viscosity is temperature dependent in this model.

2.4 Implementation in Matlab

The physics which have been discussed in this chapter are implemented in a Matlab code to simulate the FRB behavior in the time domain. In this section Matlab related topics are discussed. In section 2.4.1 is described how the physics are implemented in a Matlab routine; the section describes the sequence of steps which are taken. How the time step is controlled during integration of the system of equations is shown in section 2.4.2. After simulation, the waterfall plot is a tool which is used frequently to analyze the dynamic behavior which has been simulated. How the waterfall plots are calculated is described in section 2.4.3.

2.4.1 Implementation of the physics in Matlab

Matlab version R2010b has been used for evaluation of the theoretical FRB model. Figure 2.9 shows an overview of which steps are taken during the simulation. Several simulation parameters can be altered which control the length of the simulation. The simulated time is defined by the domain $[0, t_{max}]$, with a constant time step Δt between saved simulation points.

- At the start of the simulation of a time step, the starting conditions for the differential equation solver (ODE solver) are loaded. The vector with starting conditions contains the positions and velocities of the shaft $(e_{x,s}, e_{y,s}, \dot{e}_{x,s}, \dot{e}_{y,s})$ and position, rotation, velocities and rotational speed of the floating ring $\left(e_{x,r}, e_{y,r}, \phi, \dot{e}_{x,r}, \dot{e}_{y,r}, \dot{\phi} = \omega_r\right)$. At $t = 0$ this vector is filled with zeros. At other time steps the results of the previous time step serve as starting condition for the next time step.

- After the starting conditions for the ODE solver have been determined, the ODE solver is started to solve the system of equations for the time range $[t, t + \Delta t]$. The ODE solver has to integrate the system for a time length Δt, but splits it in smaller time steps δt. The value of δt is determined by the error of the results which is calculated by the ODE solver. If the error is too large, the calculations are redone using a smaller δt. This error control is described in more detail in section 2.4.2.

- When the ODE solver is started, first all the parameters are loaded, which may be time-dependent. After the parameters are loaded the shaft rotational frequency is calculated which is a function of time. In the simulations performed in this thesis, the shaft rotational frequency is linearly dependent on time, as shown in equation 2.15. Unless otherwise specified, the simulations have been done with $\omega_{s,start} = 0 \frac{rad}{s}$ and $\frac{d\omega_s}{dt} = 2618 \frac{rad}{s^2}$, or $25000 \frac{RPM}{s^2}$.

$$\omega_s\left(t\right) = \omega_{s,start} + \frac{d\omega_s}{dt} t \tag{2.15}$$

- With the configuration at a certain time step, which is defined by the starting conditions of the ODE solver, the forces which are working on the system can be calculated. First the pressure distributions in the inner and outer film and the resulting forces on the shaft and floating ring are calculated. Secondly, the magnitude and the angle β of the unbalance force is calculated. At $t = 0$, the unbalance direction is in the direction of the positive x-axis, or $\theta = \pi$. The unbalance forces are then calculated by

  $$F_{x,u} = \cos(\beta)\,|F_u| \tag{2.16}$$

  $$F_{y,u} = \sin(\beta)\,|F_u| \tag{2.17}$$

  After the unbalance forces are calculated, the viscous drag forces and torque are calculated. The forces which are calculated are the viscous drag force in x- and y-directions which originate from the outer film and viscous drag forces in x- and y-directions which originate from the inner film. Furthermore, the torque caused by the viscous drag working on the inner and outer surfaces of the floating ring is calculated.

- When all the mentioned forces which participate in the dynamics have been calculated, the system of equations is formed and solved. The force vector $\mathbf{F}(\mathbf{u}, \dot{\mathbf{u}})$ contains all the forces working on the different degrees of freedom and is a function of $\mathbf{u}$ and $\dot{\mathbf{u}}$. This means that the force vector changes during a solution step of the ODE solver. The system of equations is shown in equation 2.18.

  $$\mathbf{M}\ddot{\mathbf{u}} = \mathbf{F}(\mathbf{u}, \dot{\mathbf{u}}) \tag{2.18}$$

  Because the system of equations contains the second derivative of the degrees of freedom vector, the order has to be reduced to create a first order differential equation. By defining the vector $\mathbf{z}$ as in equation 2.19, the second order system of differential equations as shown in equation 2.18 is reduced to the first order system of differential equations shown in equation 2.20.

  $$\mathbf{z} = \begin{bmatrix} \mathbf{u} \\ \dot{\mathbf{u}} \end{bmatrix} \tag{2.19}$$

  $$\begin{bmatrix} \mathbf{I} & 0 \\ 0 & \mathbf{M} \end{bmatrix} \dot{\mathbf{z}} = \begin{bmatrix} 0 & \mathbf{I} \\ 0 & 0 \end{bmatrix} \mathbf{z} + \begin{bmatrix} 0 \\ \mathbf{F}(\mathbf{z}) \end{bmatrix} \tag{2.20}$$

  This first order system of differential equations is solved using an ODE solver in Matlab.

- The ODE solver returns a matrix which contains solutions for the vector $\mathbf{z}$ at different points in time in the interval $[t, t + \Delta t]$. For example, the matrix which has been returned as output of the ODE solver could be a 20 by 10 matrix if the vector $\mathbf{z}$ is a vector of length 10 and the ODE solver needed 20 time steps δt to solve the system of equations for the mentioned time interval. The last entry of each degree of freedom is saved to different vectors; one vector for each degree of freedom. After this solution is saved the ODE solver is started again for the next time interval. This start-stop routine of the ODE solver results in vectors which contain entries which have an equal time spacing Δt between them. After a specified number of entries in the vectors with results, the vectors are saved to a file on the hard disk and the vectors are cleared to prevent memory issues.

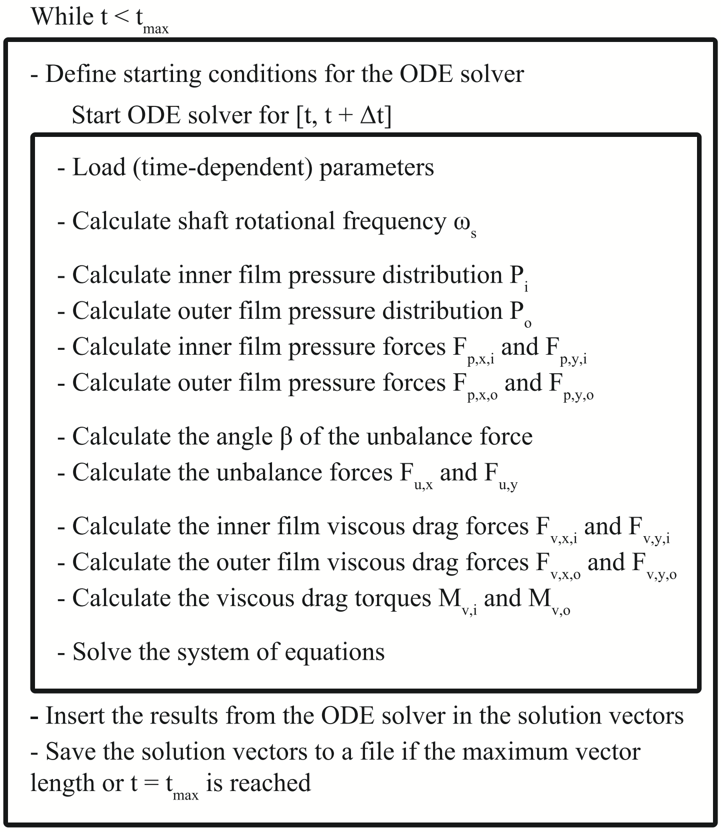

Figure 2.9: Schematic overview of the steps taken by the Matlab model

2.4.2 Time step control of the ODE solver

Integration of the system of equations is done using the ode15s ODE solver in Matlab. This solver is used for solving stiff problems; problems which need a very small time step to lead to a converging solution. The solution at each time step has to meet certain error criteria. The criteria which are used by Matlab are explained below and can also be found in the Matlab manual [7].

Error criteria can be defined which should be met by the solver before a solution is accepted. These criteria are the relative error and the absolute error. The relative error defines how many digits of a solution should be correct, taking the order of the solution into account. The relative error of a solution on a time step is set to 10^{-3}. This means that the error e of solution y at step i should meet the requirement

$$|e\left(i\right)| < 10^{-3} \cdot |y\left(i\right)| \tag{2.21}$$

If, for example, the solution is $|y\left(i\right)| = 1 \cdot 10^{-5}$, then the error should be smaller than $10^{-3} \cdot 10^{-5} = 10^{-8}$.

The absolute error defines the maximum amount of digits which should be correct, regardless of the order of the solution. The order of the expected displacements is 10^{-5}, which is the order of the size of the gaps between the structural parts. The maximum value of the absolute error is chosen 10^{-10}.

$$|e\left(i\right)| < 10^{-10} \tag{2.22}$$

To avoid unnecessary accuracy and therefore unnecessary computational time, the solution at a time step is accepted when the largest of the two error criteria is met. When neither of the criteria is met a new solution of the system of differential equations will be calculated, but a smaller time step than during the previous attempt will be used. When the time step is too small, i.e. the magnitude of the time step is smaller than the smallest number the computer can handle, an error is returned to the user.

2.4.3 Calculation of waterfall plots

A valuable tool to investigate dynamics is the waterfall plot. A waterfall plot gives a good overview of the frequency content as a function of shaft rotational speed, as was seen in figure 1.2. The simulated time signal of the different degrees of freedom can be used to calculate waterfall plots. To create this waterfall plot, fast Fourier transforms (FFT's) have to be calculated. FFT's are calculated for the total shaft frequency range, from the minimum rotational frequency up to the maximum rotational frequency with step size ΔRPM between FFT's. The FFT's are calculated using Matlab's fft function.

The quality and resolution of the waterfall plot are influenced by the length of the time block which is used to calculate the FFT of that time block and the step size ΔRPM. The resolution in vertical direction can be controlled by increasing or decreasing ΔRPM. A smaller value for ΔRPM means more FFT's are calculated and therefore a better resolution in vertical direction is achieved. The resolution of the frequency axis (horizontal axis in this thesis) is determined by

$$\Delta f = \frac{1}{t_{block}} \tag{2.23}$$

In this equation t_{block} is the length of the time block in seconds. The time signal y_{FFT,ω_s} which is used for calculating the FFT around a shaft speed ω_s is defined by

$$y_{FFT,\omega_s} = y\left[t\left(\omega_s\right) - \frac{t_{block}}{2}, t\left(\omega_s\right) + \frac{t_{block}}{2}\right] \tag{2.24}$$

Equation 2.23 implies that a longer time block leads to a better resolution on the frequency axis. However, because the shaft rotational speed increases linearly with time, a longer time block means that more information of other shaft speeds is included. Examples of this effect are shown in table 2.2. Results in this table show that when a smaller Δf is used or when a faster run-up is simulated, the range of shaft speeds included in the time data needed for the FFT is larger. Each shaft speed has its own dynamic behavior, with different peak frequencies. Because these frequencies are close, but not equal, the peaks will be "smudged" if the bandwidth of frequencies is too large. To reduce the influence of the data which is not exactly at the time of interest, a Hanning window is applied on the time data before the FFT is calculated.

Table 2.2: Examples of the influence of shaft speed increase step size and frequency resolution on the data range which is used for calculating a FFT

$\omega_s\,[Hz]$	$\frac{d\omega}{dt}\left[\frac{Hz}{s}\right]$	$\Delta f\,[Hz]$	$t_{block}\,[s]$	ω_s range $[Hz]$
1000	100	10	0.1	$[995 - 1005]$
1000	200	10	0.1	$[990 - 1010]$
1000	100	5	0.2	$[990 - 1010]$
1000	200	5	0.2	$[980 - 1020]$

Chapter 3

Experimental approach

In this chapter the experimental approach is highlighted. The goals of these experiments are to

- compare the theoretical results of the demonstrator model to the experimental results
- measure the frequency content of the movement of the floating ring bearing
- measure the rotational speed of the floating ring bearing

In section 3.1 the design of the demonstrator is discussed. Section 3.2 shows the test setup as it has been used.

3.1 Demonstrator design

A cross section of the design of the demonstrator, without the drive, is shown in figure 3.1 and its components are named in table 3.1.

Measurement points

Besides the shaft rotational speed, there are six measurement points which can be used in the demonstrator. Four of these measurements points are used to measure shaft motion and are two pairs of orthogonal measurements points; shaft motion is measured at two points along the shaft in X- and Y-direction. The other two sensors are placed orthogonally to measure the motion of the FRB. As an addition to FRB motion, the rotational speed of the FRB can be measured because the lubricant feeding holes can be detected.

The shaft and FRB motion sensors used are eddy-current sensors. Micro-Epsilon, a manufacturer of eddy-current sensors, describes the working principle of these sensors on page 2 of the technical note “Precise Non-contact displacement sensor” as: “The eddy current measurement principle is an inductive measuring method based on the extraction of energy from an oscillating circuit. This energy is required for the induction of eddy currents in electrically conductive materials. A coil is supplied with an alternating current, which causes a magnetic field to form around the coil. If an electrically conducting object is placed in this magnetic field, eddy currents are induced, which form an electromagnetic field according to Faraday’s Induction Law. This field acts against the field of the coil, which causes a change in the impedance of the coil. The controller calculates the impedance by considering the change in amplitude and phase position of the sensor coil.”. [8]

The shaft motion can easily be measured by placing an eddy-current sensor close to the shaft at the desired location. The measurement of FRB motion, however, is harder to do with eddy-current sensors. Because it is undesired to drill a hole through all of the bearing housing and thereby disturbing the

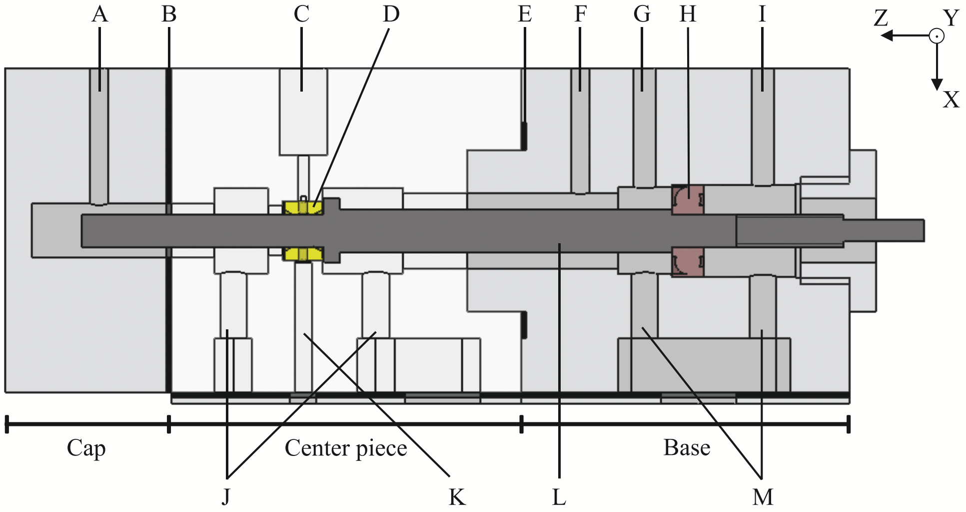

Figure 3.1: Cross section of the demonstrator without motor

Table 3.1: Demonstrator component names

A	Shaft motion sensor mounting; end of shaft side
B	Rubber seal between cap and center piece
C	Floating ring bearing lubricant inlet mounting
D	Floating ring bearing
E	Rubber seal between center piece and base
F	Shaft motion sensor ball bearing side
G	Ball bearing lubricant inlet mounting
H	Super precision ball bearing
I	Ball bearing lubricant inlet mounting
J	Lubricant outlet; FRB side
K	Floating ring vibration and rotational speed sensor mounting
L	Shaft
M	Lubricant outlet; ball bearing side

oil film, the measurement principle eddy-current sensors rely on, is used in the opposite way. As described, an object has to be electrically conductive to be detected by an eddy-current sensor. The recommended minimum thickness of the target material to be detectable is given by equation 3.1 [6].

$$\text{minimum target thickness} = 3\delta \tag{3.1}$$

with

$$\delta = 0.0503\sqrt{\frac{\rho}{f\mu_r}} \tag{3.2}$$

A material's skin-depth, calculated by equation 3.2, is dependent of the material's electrical resistivity ρ, the material's magnetic permeability μ_r and the oscillation frequency f of the eddy-current sensor. When the electrical resistivity of a target material is very high, or the magnetic permeability is very low, an eddy-current sensor will have difficulties detecting it.

By drilling a sensor hole which does not go all the way through the bearing house and using a bearing house material which is hard to detect for the sensor, the sensor will be able to "see through" the remainder of the bearing housing. This is visualized in figure 3.2, which shows a cross section of the demonstrator at the FRB. The names of the labeled components can be found in table 3.1.

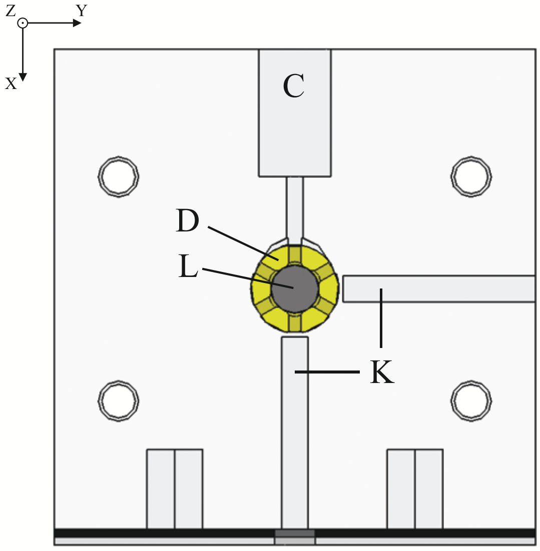

Figure 3.2: Cross section of the demonstrator at the FRB, showing the orthogonal sensor mounting holes

The material chosen for the bearing housing is a polycarbonate, which has a high electrical resistivity and a low magnetic permeability. Evaluation of equation

3.1 indicates that the thickness of this material should be large to be able to detect it with an eddy-current sensor. By leaving 0.5mm of material between the sensor head and the oil film, the oil film will not be disturbed and the sensor will not be able to detect the polycarbonate. The sensor can still detect the only electrical conductive object in its range; the floating ring.

3.2 Test setup

An overview of the demonstrator and its drive are shown in figure 3.3a. A close up of the demonstrator is shown in figure 3.3b. The drive is a modified DV6D type turbocharger. This turbocharger is modified so it can be connected to the demonstrator by means of a coupling and can be driven by compressed air. Controllable shaft rotational speeds up to approximately 40.000 RPM, or 667 Hz, are achieved.

The measurable quantities are

- shaft displacement at the ball bearing side in x-direction
- shaft displacement at the ball bearing side in y-direction
- floating ring displacement in x-direction
- floating ring displacement in y-direction
- shaft displacement at the end of the shaft in x-direction
- shaft displacement at the end of the shaft in y-direction
- shaft rotational speed
- acceleration of the cartridge

Although the demonstrator is designed to be able to measure displacement of the floating ring in two directions, only one of these displacements could be used simultaneously due to the availability of sensors. Details on the measurement equipment can be found in appendix C.

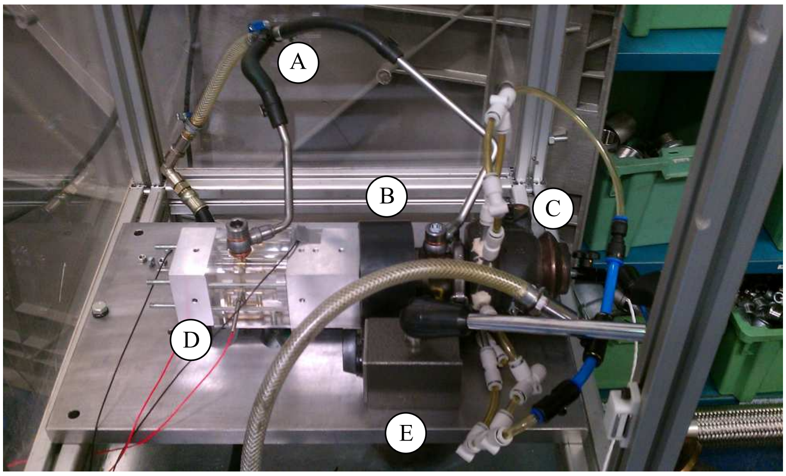

(a) Overview of the test setup; labeled are the (a) oil supply , (b) coupling protection cover, (c) modified turbine housing with pneumatic feed tubing, (d) demonstrator and (e) stand which hold the shaft rotational speed sensor

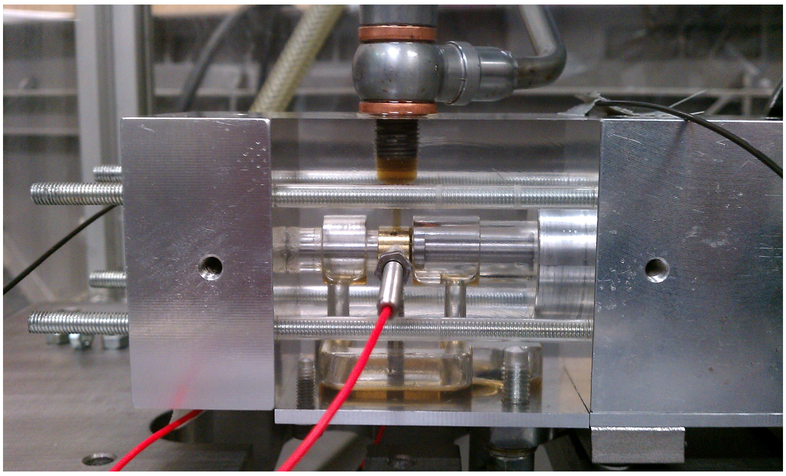

(b) Close up of the demonstrator which shows the floating ring on the shaft with an eddy-current sensor which measures the floating ring displacement in y-direction

Figure 3.3: The test setup used for the experiments; additional measurement equipment and oil pump are not shown

Chapter 4

Results and discussion

In this chapter the results of simulations and experiments are presented. In section 4.1 a simple situation is simulated to check the results of the theoretical FRB model. In this simulation the shaft of the FRB is modeled as a point mass and the configuration is under a constant load. In the second section, 4.2, the point mass model which was used in the first section is used for a run-up simulation. In this simulation realistic parameters are used.

The demonstrator, which is used for model validation, is simulated with a finite element model. The results of a run-up simulation with this model are shown in section 4.3. The results of the experiments with the demonstrator are shown in section 4.4.

The results of the simulations and experiments are compared and discussed in section 4.5. This chapter is closed with the results of a sensitivity analysis in section 4.6. The results in this section have been obtained by using the point mass simulation from sections 4.1 and 4.2, but using different parameters.

An overview of this chapter is shown below in table 4.1.

Table 4.1: Overview of the results obtained by simulation and experiments

	Simulation results	Experimental results
Model verification	§4.1	-
Point mass simulation	§4.2	-
Demonstrator	§4.3	§4.4
Sensitivity analysis	§4.6	-

4.1 Model verification

In figure 4.1 a FRB model with the shaft represented by a point mass is shown. This means shaft influences, like rotordynamics of the shaft or rotor and bending forces of the shaft are not present in this simulation. Figure 4.1 shows the coordinates $e_{x,r}$, $e_{y,r}$, $e_{x,s}$ and $e_{y,s}$ and center of masses m_s and m_r of the model. In this section the results of a simple situation are shown and is meant to check whether the simulation results are the results which would be expected. The parameters used in this simulation are shown in table 4.2. As can be seen in this table, the shaft rotational speed is constant and no unbalance is present. The mass of the shaft and floating ring are increased to increase bearing load, which is chosen for verification purposes; if the combination of bearing parameters and bearing load is chosen right the bearing behavior will not become unstable, which is desired for model verification.

The simulation with constant shaft rotational frequency has been performed for the time range $[0 - 4]$s. The starting position of both the shaft and the floating ring is in the origin [0, 0]. The result of the displacement of the system is shown in figure 4.2. In this figure $e_{s^*} = e_s - e_r$ and stands for the displacement of the shaft within the floating ring. In other words, the displacement of the shaft with the center of the floating ring as origin. It is seen that the shaft and floating

Table 4.2: Parameter values used in the point mass simulation of section 4.2

Parameter	Value	Unit
ω_s	2	Hz
Shaft unbalance	0	kg·m
m_s	$200 \cdot 10^{-3}$	kg
m_r	$100 \cdot 10^{-3}$	kg
I_r	$7.03 \cdot 10^{-8}$	kgm^2
L_i	$4 \cdot 10^{-3}$	m
L_o	$7 \cdot 10^{-3}$	m
C_i	$15 \cdot 10^{-6}$	m
C_o	$36 \cdot 10^{-6}$	m
R_s	$3 \cdot 10^{-3}$	m
$R_{r,o}$	$5.5 \cdot 10^{-3}$	m
μ_i	$12 \cdot 10^{-3}$	Pa·s
μ_o	$12 \cdot 10^{-3}$	Pa·s

ring first “fall down”, before moving to a more or less stable position. In figure 4.3 the magnitude of the velocities of the shaft and floating ring are displayed. Since the velocities are very low, the system has almost reached an equilibrium position.

If the system is in an equilibrium position, the sum of the forces in all directions should be zero. The forces caused by the pressure in the oil films in x- and y-direction are shown in figures 4.4a and 4.4b. The load in the x-direction is caused by the gravitational forces of the shaft and floating ring, which have a magnitude of

$$F_{x,s,g} = 0.2 \cdot 9.81 = 1.962\text{N} \tag{4.1}$$

$$F_{x,s,r} = 0.1 \cdot 9.81 = 0.981\text{N} \tag{4.2}$$

The pressure film force on the surface of the shaft is -1.959N in the x-direction. This force works in the negative x-direction, because the gravitational force of the shaft works in the positive x-direction. The magnitude of the pressure film force is almost equal to the gravitational force. The remaining 0.003N is partly supported by the viscous drag force and is partly a remainder of the dynamic effects which are still present in the system. The same holds for the pressure film force working on the outer surface of the floating ring. The pressure distribution in the outer oil film generates -2.933N. The outer film has to support both the weight of the floating ring as the force caused by the inner oil film, which is 2.943N combined. The remaining 0.01N is again a combination of viscous drag force and dynamic effects. In the y-direction the forces are not equal to zero.

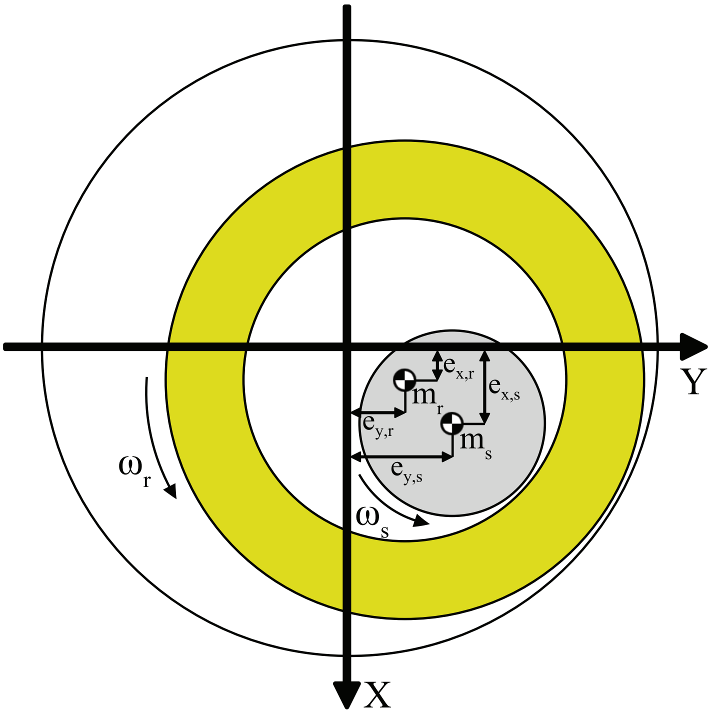

Figure 4.1: Point mass model coordinates

The explanation of this is the same as the explanation for the remainder of the forces in vertical direction.

The maximum pressures in time in both oil films are shown in figure 4.5. Both oil films have converged to a constant pressure after reaching a peak pressure. This peak pressure is caused by the impact of the "falling" shaft and floating ring masses, which had their initial position in the origin. The pressures shown in this figure are only the peak pressure in the oil films. Therefore, an increase in peak pressure does not necessary mean a higher force generated by the oil films. This is seen in the simulated situation; figure 4.4a shows that the pressure film forces in vertical direction converge much faster than the peak pressures.

When the system which is under a constant load reaches its equilibrium position, the rotational speed of the floating ring converges to a constant value as is seen in figure 4.6.

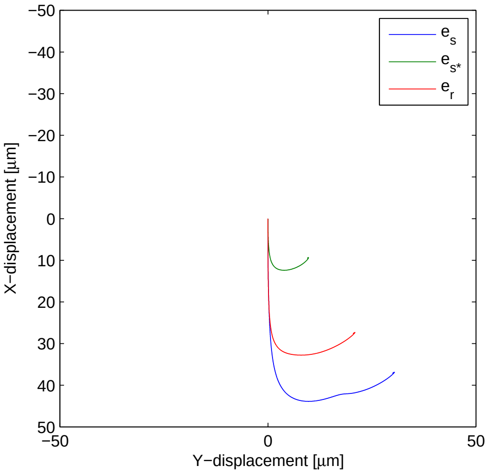

Figure 4.2: Displacement of the shaft, shaft relative to the floating ring and floating ring resulting from the verification simulation

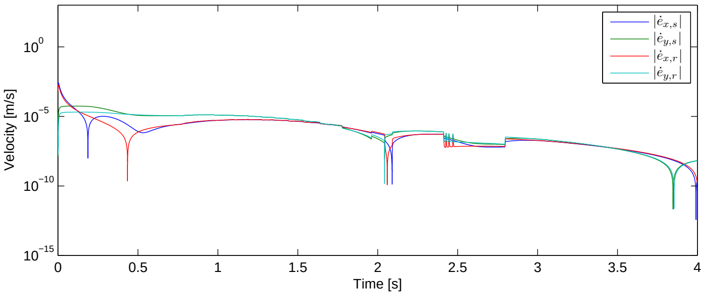

Figure 4.3: Absolute velocities of the shaft and floating ring in x- and y-direction

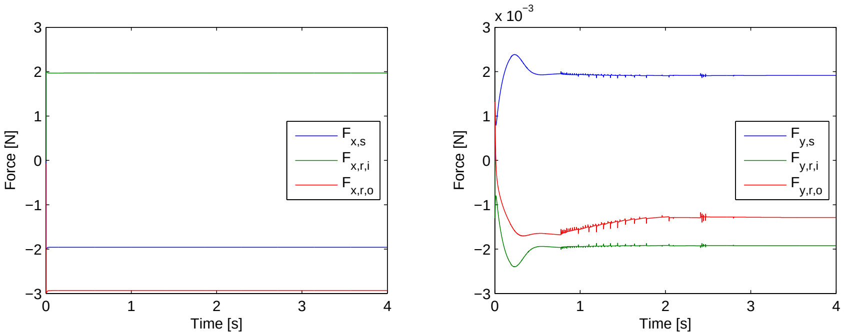

(a) Pressure film forces in x-direction **(b)** Pressure film forces in y-direction

Figure 4.4: Velocities of the shaft and floating ring in radial and tangential directions

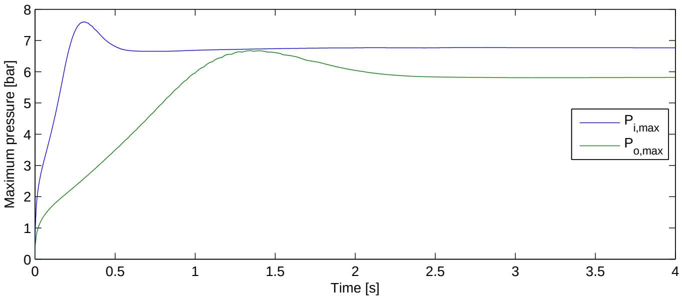

Figure 4.5: Peak pressures in the oil films of the verification simulation

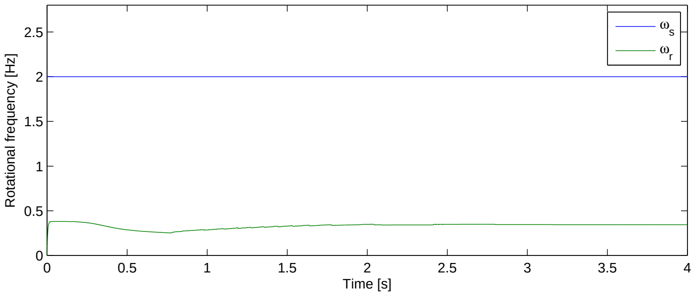

Figure 4.6: Rotational speeds of the shaft and floating ring

4.2 Point mass simulation

In this section the results of a FRB simulation with the shaft represented by a point mass are shown. This is the same model as shown in figure 4.1 in the previous section. The parameters which are used in this simulation are the same as in a turbocharger and are shown in table 4.3. In this simulation the magnitude of the point mass is chosen to be half the weight of a turbocharger's turbine-rotor assembly, which is supported by two FRB's in a turbocharger.

Table 4.3: Parameter values used in the point mass simulation of section 4.2

Parameter	Value	Unit
ω_s	$0 - 3750$	Hz
Shaft unbalance	$2 \cdot 10^{-8}$	kg·m
m_s	$35 \cdot 10^{-3}$	kg
m_r	$3.47 \cdot 10^{-3}$	kg
I_r	$7.03 \cdot 10^{-8}$	kgm^2
L_i	$4 \cdot 10^{-3}$	m
L_o	$7 \cdot 10^{-3}$	m
C_i	$15 \cdot 10^{-6}$	m
C_o	$36 \cdot 10^{-6}$	m
R_s	$3 \cdot 10^{-3}$	m
$R_{r,o}$	$5.5 \cdot 10^{-3}$	m
μ_i	$12 \cdot 10^{-3}$	Pa·s
μ_o	$12 \cdot 10^{-3}$	Pa·s

This section is divided in three subsections. In section 4.2.1 waterfall plots of the simulation are discussed. These waterfall plots give insight in the frequency content at different operating speeds.

4.2.1 Waterfall plots

To obtain an overview of the dynamic behavior of the system, waterfall plots are made. Figure 4.7 shows the waterfall plot of the movement of the shaft with three frequency lines labeled which have a major contribution to the dynamic behavior. As explained in section 1.2, the synchronous frequency line originates from the unbalance which is present in the shaft and therefore has a frequency which is equal to the frequency of the shaft.

The other two frequency lines are located in the subsynchronous area and are labeled 'Whirl 1' and 'Whirl 2'. As the name indicates, these frequencies are whirl frequencies; frequencies of limit cycle motions of one body within another. Whirling is visualized in figure 4.8. At a certain rotation speed of the shaft, whirl 1 suddenly disappears. This phenomenon will be referred to as jumping and the rotational speed at which this happens will be referred to as the jump speed. The jump speed also marks the point where the mode shape of the system changes from the first to the second mode shape.

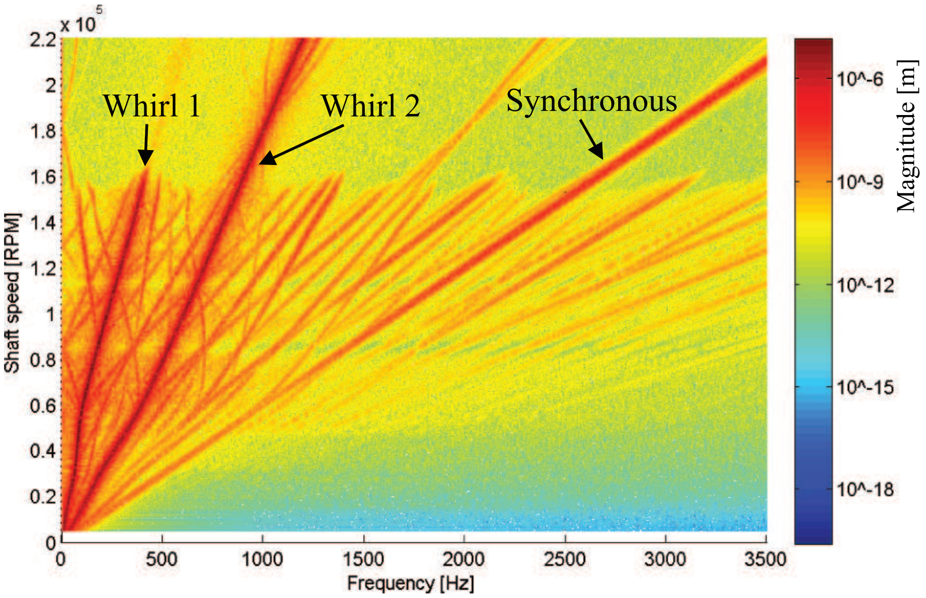

Figure 4.7: Waterfall plot of the position of the shaft in x-direction

Waterfall plots of the position of the floating ring and the position of the shaft with respect to the floating ring, respectively figures 4.9 and 4.10, give more insight in the origin of the whirl 1 and whirl 2 lines. Figure 4.9 shows that the first mode shape is dominated by the whirl 1 frequency line, which leads to the conclusion that the whirl 1 frequency line is the whirl frequency of the floating ring inside the bearing housing in the first mode shape. After the jump the whirl frequency of the floating ring changes to whirl 2.

Figure 4.10 shows the waterfall plot of the position of the shaft relative to the floating ring. This is the position of the shaft seen from a local coordinate system which has its origin in the center of the floating ring; $e_{x,s*} = e_{x,s} - e_{x,r}$ and $e_{y,s*} = e_{y,s} - e_{y,r}$ are the local coordinates of the shaft inside the floating ring. In both modes the whirl 2 frequency line describes the major component of the movement of the shaft relative to the floating ring.

The first mode shape can be visualized as follows: the floating ring whirls inside the bearing housing while the shaft whirls inside the floating ring with a frequency which is higher than the floating ring whirl frequency. In the second mode shape the whirl frequency of the shaft and floating ring is equal. This also means that the mean phase between the eccentricity directions of the floating ring and the shaft inside the floating ring is almost constant in the second mode shape.

The two different mode shapes are shown in figures 4.11a and 4.11b. The effect of different whirling frequencies of the shaft and floating ring is visible in figure

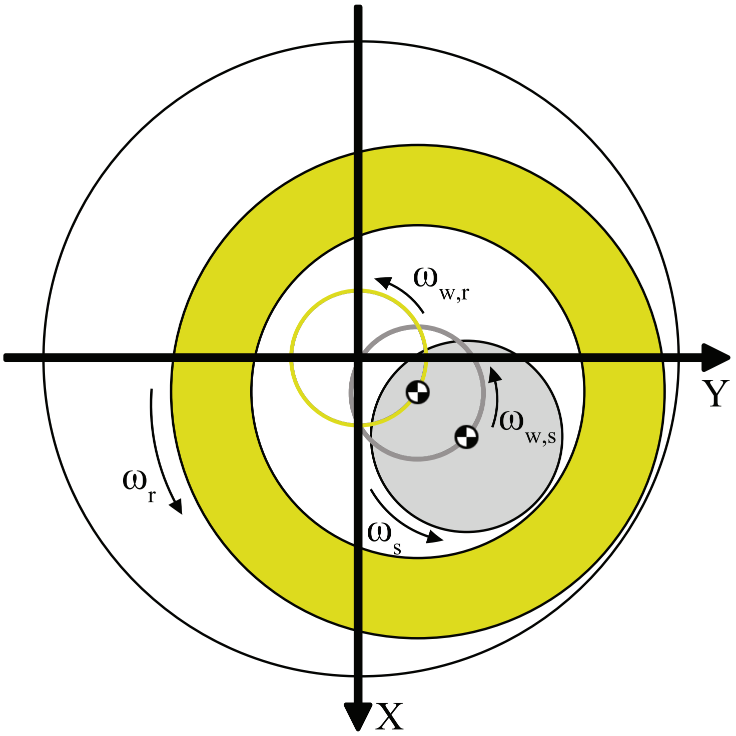

Figure 4.8: Graphical interpretation of whirling. The shaft follows the gray orbit within the floating ring with a rotational frequency of $\omega_{w,s}$. The floating ring moves according to the yellow orbit within the bearing housing with a rotational frequency of $\omega_{w,r}$

4.11a. The displayed values are the eccentricities in the x- and y-directions. Eccentricity is a dimensionless quantity which can have values between 0, which means centered operation, to 1, which means physical contact between shaft and floating ring or floating ring and bearing housing. The eccentricity of the shaft with respect to the global coordinate system is denoted by ϵ_s, ϵ_r is the eccentricity of the ring with respect to the global coordinate system. The third eccentricity, ϵ_{s*}, is the eccentricity of the shaft with respect to a local coordinate system which has its origin in the center of the floating ring. Equations 4.3 to 4.5 describe the eccentricities in mathematical form.

$$\epsilon_s = \frac{\sqrt{e_{x,s}^2 + e_{y,s}^2}}{C_i + C_o} \tag{4.3}$$

$$\epsilon_r = \frac{\sqrt{e_{x,r}^2 + e_{y,r}^2}}{C_o} \tag{4.4}$$

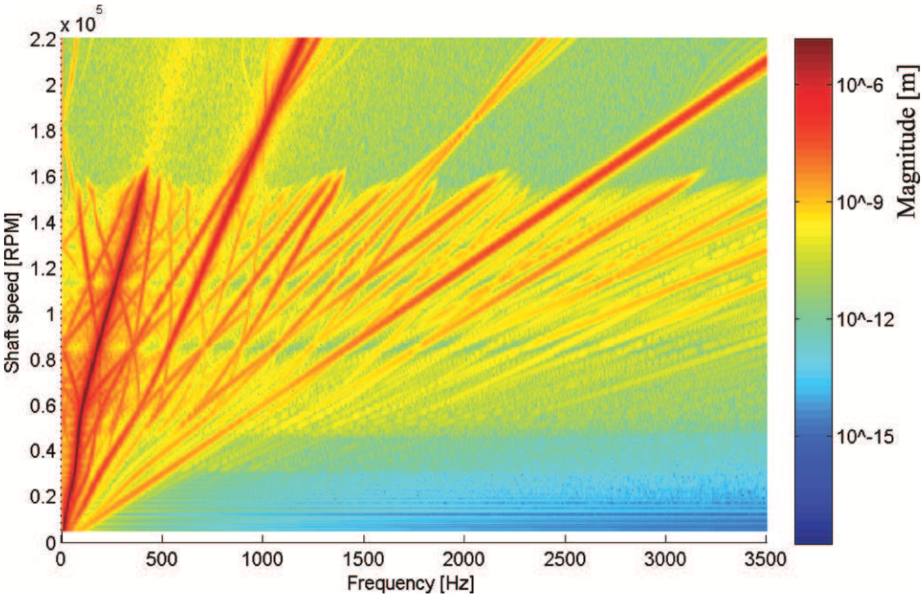

Figure 4.9: Waterfall plot of the position of the floating ring

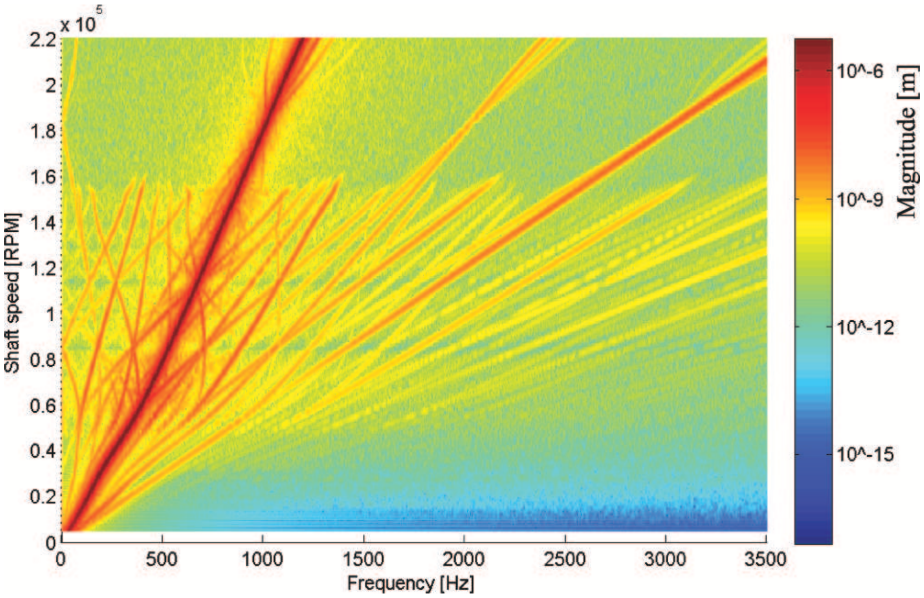

Figure 4.10: Waterfall plot of the position of the shaft relative to the floating ring

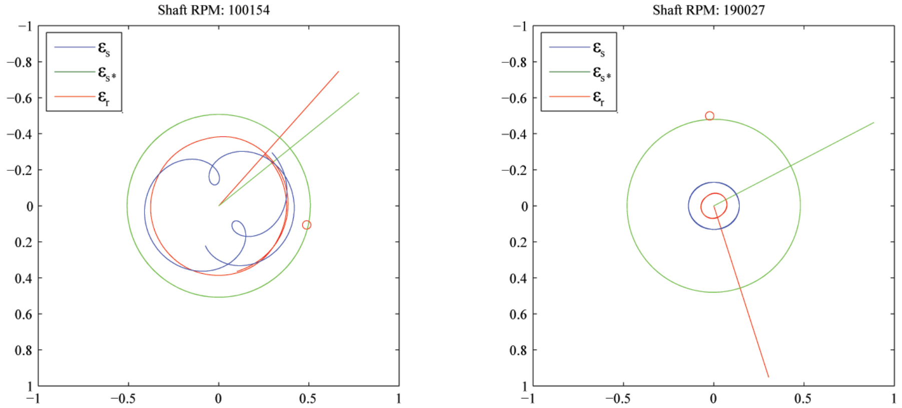

(a) Trace of the movement while the system is in the first mode shape

(b) Trace of the movement while the system is in the second mode shape

Figure 4.11: Movement of the different bodies in the first and second mode shapes. The red circle indicates the direction of the unbalance force at the time step of this configuration. The blue and green lines represent the directions of respectively ϵ_s and ϵ_{s^*}.

$$\epsilon_{s*} = \frac{\sqrt{\left(e_{x,s} - e_{x,r}\right)^2 + \left(e_{y,s} - e_{y,r}\right)^2}}{C_i} \tag{4.5}$$

4.2.2 Body displacement and velocity

The eccentricities of the shaft and ring are visualized in figure 4.12. The jumping behavior is visible in this figure. In the speed region of the first mode shape a heavily oscillating ϵ_s is seen. This oscillation is caused by the fact that ϵ_s is a combination of ϵ_r and ϵ_{s*}. As explained in the previous section, the whirling frequency of the shaft inside the floating ring is higher than the whirling speed of the floating ring in the bearing housing. Because the whirling frequencies are not equal, ϵ_s shows oscillating behavior. When the system is in the speed range of the second mode shape the whirling frequencies are equal and ϵ_s shows stable behavior.

The floating ring speed ratio, FRSR, is described by equation 4.6 and the results from the simulation are shown in figure 4.13. At 30kRPM the FRSR shows a local maximum and a local minimum at 55kRPM. This local minimum and maximum FRSR is caused by the fact that at those rotational speeds a local minimal and maximal difference between ϵ_{s*} and ϵ_r occurs, as seen in figure 4.12. When ϵ_r increases, the viscous moment working on the outer surface of the floating ring increases, which means more friction. When ϵ decreases, the friction becomes less. The same holds for ϵ_{s*}. When $\epsilon s*$ increases, the driving moment on the inner surface of the floating ring increases and it decreases when ϵ_{s*} decreases.

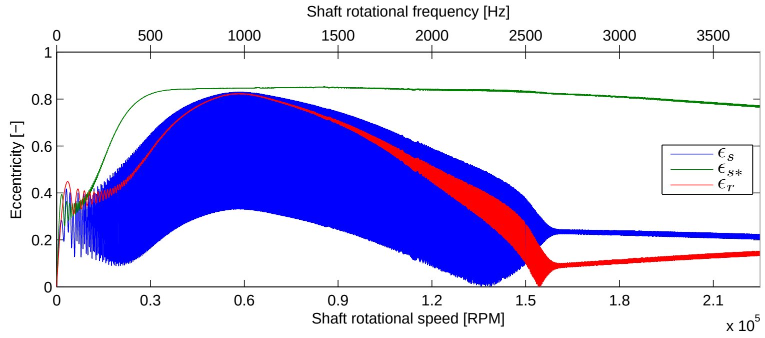

Figure 4.12: Eccentricities of the shaft (ϵ_s), floating ring (ϵ_r) and shaft relative to floating ring (ϵ_{s^*}) versus shaft rotational speed

$$FRSR = \frac{\omega_r}{\omega_s} \tag{4.6}$$

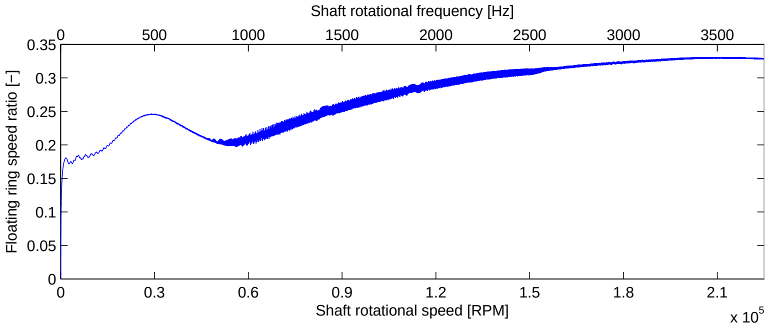

Figure 4.13: Ratio of the speed of the floating ring to the speed of the shaft

The velocities of the shaft and floating ring are split up in a tangential and a radial component. The radial and tangential velocities of the shaft relative to the floating ring can be seen in figures 4.14a and 4.14b. In the radial direction the velocity of the shaft oscillates around 0, which indicates that the position of the shaft relative to the floating ring vibrates in radial direction. The tangential velocity originates from the whirling behavior which has a frequency and a radius of the limit cycle. The magnitude of the tangential velocity keeps increasing with increasing shaft rotational speed, but the slope is getting smaller.

The tangential and radial velocities of the floating ring are shown in figure 4.14c and 4.14d. The effect of the jumping is clearly seen in both radial and tangential velocities. As can be seen in figure 4.12, the eccentricity of the ring has less oscillation after the jump, which explains why the radial velocity is smaller after the jump.

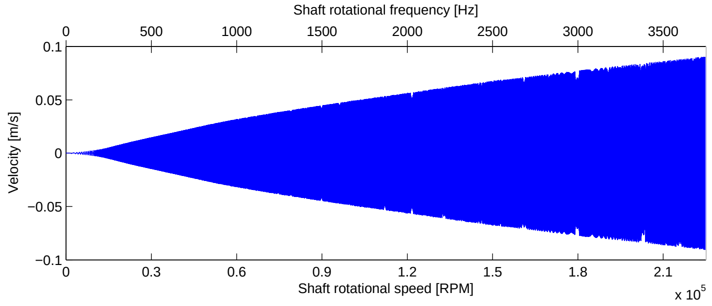

(a) Velocity of the shaft relative to the floating ring in radial direction

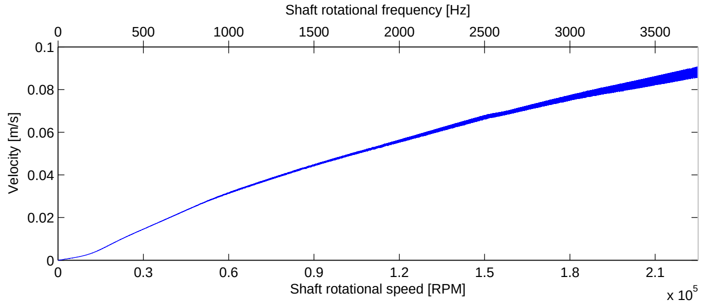

(b) Velocity of the shaft relative to the floating ring in tangential direction

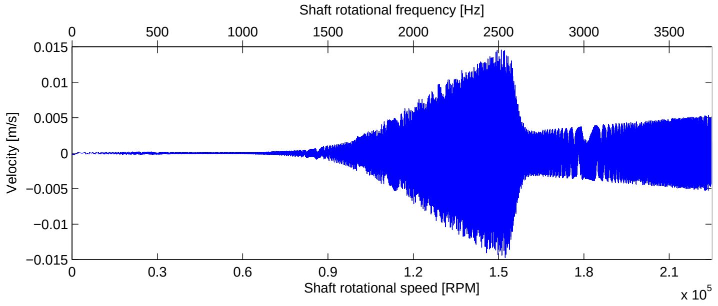

(c) Velocity of the floating ring in radial direction

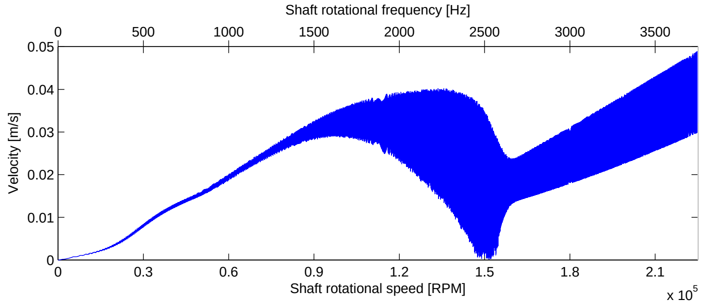

(d) Velocity of the floating ring in tangential direction

Figure 4.14: Velocities of the shaft and floating ring in radial and tangential directions

4.2.3 Peak pressure development and fluid film forces

The development of the peak pressures in the inner and outer film versus the shaft rotational speed is shown in figure 4.15. The pressures in the oil films may reach 55 bar and it is clear that in this simulation the inner oil film always has a higher maximum pressure than the outer oil film in the simulated situation. The effect of the different movement modes is also seen in the development of the maximum pressures. The effect of the transition from the first to second move is visible, but does not appear to have a large effect the visible trend. After the jump the peak pressure in the inner film keeps increasing and continues to have large fluctuations. The outer peak pressure displays similar behavior, but the maximum pressure after the jump does not rise above the maximum pressure before the jump.

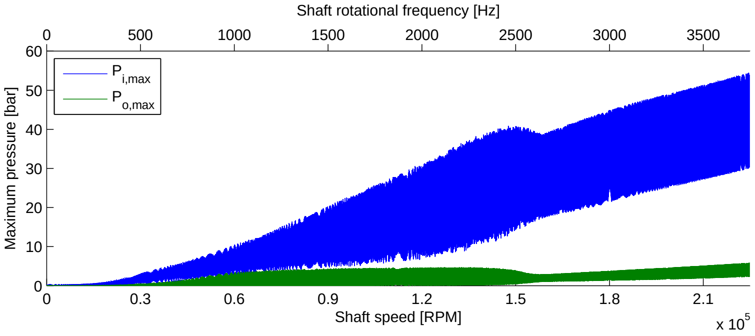

Figure 4.15: Maximum pressure in the inner and outer oil films versus shaft rotational speed

The forces which result from the pressure distribution in the oil films are shown in figure 4.16. The three forces which are displayed in this figure are the force F_s working on the shaft, $F_{r,i}$ working on the inner side of the floating ring and $F_{r,o}$ which is working on the outer side of the floating ring. These three forces can not be distinguished in the figure because the magnitudes of these three forces are very close to each other.

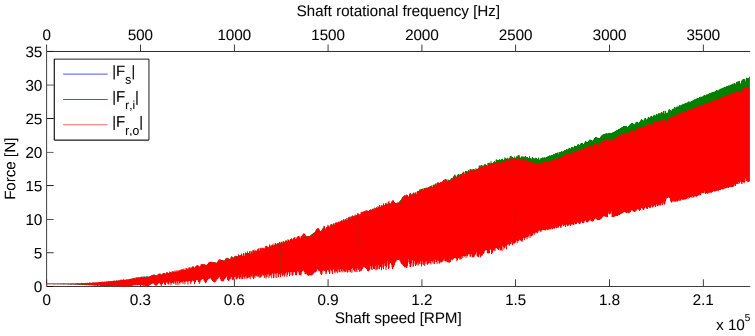

Figure 4.16: Magnitude of the fluid film forces versus shaft rotational speed

Figure 4.17 shows the pressure profiles at two points in the simulation. Figures

4.17a, 4.17c and 4.17e show the configuration of the system and pressure profiles at a point in the simulation when the system is in the first mode. Figures 4.17b, 4.17d and 4.17f show the configuration of the system and pressure profiles at a point in the simulation when the system is in the second mode.

Comparing the pressure profiles of the inner and outer oil films in both situations, shows that the peak pressure in the inner film is approximately ten times higher than the peak pressure in the outer film. Figure 2.5 showed the influences of rotational speed, radial and tangential velocity on the pressure profile when the displacement of the inner body was fixed. At the moment the simulation has been stopped while the system is in the first mode, both the inner and outer pressure profiles mainly show characteristics of pressure generation due to the rotational speed of the shaft. The specific moment shown during the second mode mainly shows the characteristics of pressure generation due to radial velocity.

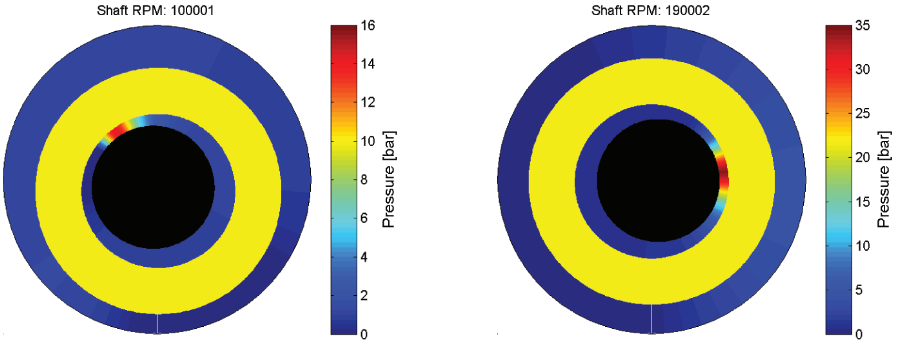

(a) Example state of the system in the first movement mode. The rotating shaft is shown in black, the floating ring in yellow.

(b) Example state of the system in the second movement mode. The rotating shaft is shown in black, the floating ring in yellow.

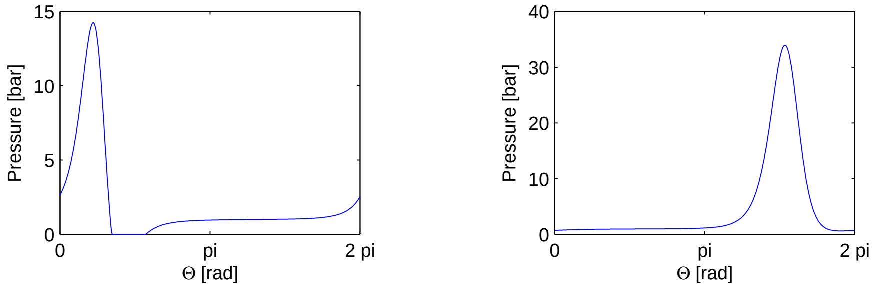

(c) Pressure at the centerline of the inner oil film in the first mode

(d) Pressure at the centerline of the inner oil film in the second mode

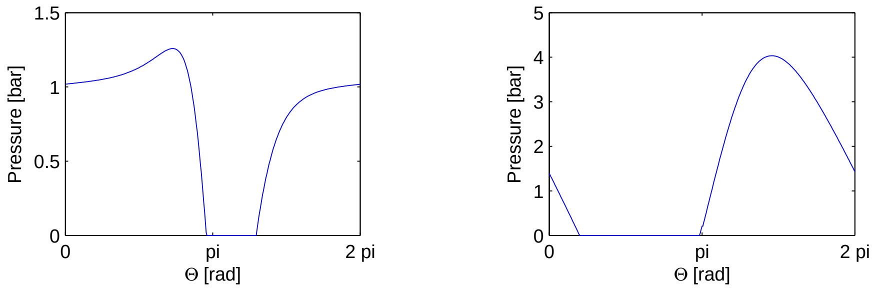

(e) Pressure at the centerline of the outer oil film in the first mode

(f) Pressure at the centerline of the outer oil film in the second mode

Figure 4.17: Example of pressure distributions in the oil films in the two movement modes

4.3 Demonstrator simulation

In order to validate the floating ring bearing model a demonstrator is created and its results are compared to a theoretical representation of the setup. In this section, the theoretical model of the demonstrator and its results are discussed. In section 4.3.1 the theoretical model is explained. In the sections 4.3.2, 4.3.3 and 4.3.4 respectively the waterfall plots, movement of the bodies and the pressure and force development are discussed. In the final section, 4.3.5, a comparison of the waterfall plots of the point mass simulation and demonstrator simulation is made.

4.3.1 Demonstrator model

The model of the demonstrator is limited to a finite element model of the shaft and assuming a support which only allows rotation around the z-axis. A simple representation of the finite element model of the shaft compared to the schematic representation of the demonstrator is shown in figure 4.18. Characteristic points are connected by vertical lines and the colors indicate different sets of physical attributes; cross-section area A, area moment of inertia I and radius R.

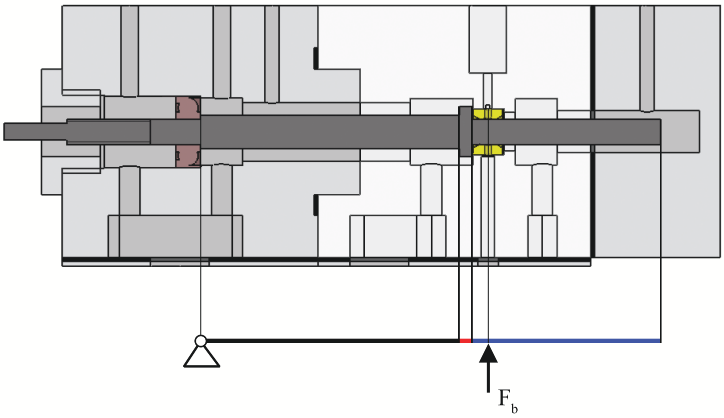

Figure 4.18: The finite element model compared to the demonstrator. The different colors represent different sets of physical parameters; different values for A, I and R.

The demonstrator shaft is modeled as a beam with different cross-sections and is supported by a hinge joint (all translational degrees of freedom fixed) and a reaction force from the FRB. The hinge joint is chosen to represent the ball bearing support because the shaft has some freedom in the rotational directions in the test setup. The expected rotational movement of the shaft at the location of the ball bearing is within this freedom and therefore the ball bearing is modeled as a hinge joint. Since the FRB model does not take tilting of the shaft within the floating ring into account, the reaction force of the FRB is modeled as a point force.

The physical parameters which have been used in the simulation are shown in table 4.4. Figure 4.19 shows some of the geometrical quantities.

Table 4.4: Parameter values used in the demonstrator simulation

Parameter	Value	Unit
L_1	$61.7 \cdot 10^{-3}$	m
R_1	$4 \cdot 10^{-3}$	m
L_2	$6 \cdot 10^{-3}$	m
R_2	$6 \cdot 10^{-3}$	m
L_3	$45 \cdot 10^{-3}$	m
R_3	$3 \cdot 10^{-3}$	m
ρ	7800	kg·m^{-3}
E	$210 \cdot 10^{9}$	Pa
m_r	$3.47 \cdot 10^{-3}$	kg
I_r	$7.03 \cdot 10^{-8}$	kgm^2
L_i	$4 \cdot 10^{-3}$	m
L_o	$7 \cdot 10^{-3}$	m
C_i	$30 \cdot 10^{-6}$	m
C_o	$50 \cdot 10^{-6}$	m
$R_{r,o}$	$5.5 \cdot 10^{-3}$	m
μ_i	$12 \cdot 10^{-3}$	Pa·s
μ_o	$12 \cdot 10^{-3}$	Pa·s

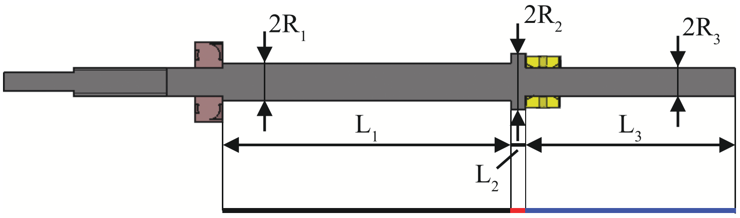

Figure 4.19: Nomenclature of some of the values listed in table 4.4

The finite element model is built out of ten nodes and nine elements, which is shown in figure 4.20. The different colors represent different sets of physical properties. These properties are listed in table 4.5 and are equal to the actual dimensions of the demonstrator. Each node has four degrees of freedom; displacement in x- and y-directions and rotation around the x- and y-axes. Displacement in axial direction is assumed zero and rotation around the z-axis is prescribed by the shaft rotational speed.

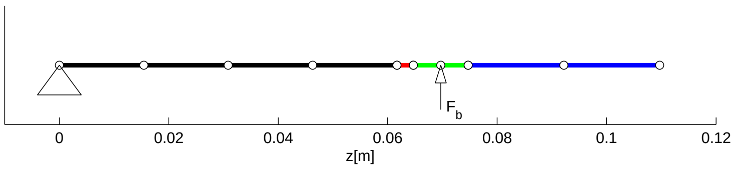

Figure 4.20: Finite element model of the demonstrator. The nodes are shown as circles and elements by colored lines. Different colors stand for different physical attributes.

Each element has a mass matrix $\mathbf{M_s}$, shaft inertia matrix $\mathbf{M_{s,s}}$, gyroscopic matrix $\mathbf{C_s}$ and stiffness matrix $\mathbf{K_s}$. These matrices can be found in appendix D.1. These element matrices are used to assemble the system matrices $\mathbf{M}$, $\mathbf{C}$ and $\mathbf{K}$ which are needed for the system of equations $\mathbf{M\ddot{u}} + \mathbf{C\dot{u}} + \mathbf{Ku} = \mathbf{F}$. The vector $\mathbf{u}$ contains the degrees of freedom of the system. The system has ten nodes; the two translational degrees of freedom of the first node are fixed, so the shaft has a total of 38 degrees of freedom. Three degrees of freedom are added to $\mathbf{u}$, which represent the x- and y-translation of the floating ring and the rotation of the floating ring.

The right hand side of this equation is the force vector $\mathbf{F}$, which contains all external forces working on the system. These forces are the forces as explained in chapter 2. All forces work on the degrees of freedom of the floating ring and the shaft node where the floating ring is located, except for the unbalance and gravity forces. The unbalance and gravity forces are modeled as distributed forces which work on every node of the shaft.

A run-up simulation for $0 - 40$kRPM is presented in this section; the operating range of the experimental setup. In the following sections the results of the simulation are presented.

Table 4.5: Overview of the physical properties of the different elements shown in figure 4.20

Element color	R[m]	A$[\mathrm{m}^2]$	I$[\mathrm{m}^4]$	L[m]
Black	$4 \cdot 10^{-3}$	$5.03 \cdot 10^{-5}$	$2.01 \cdot 10^{-10}$	$15.4 \cdot 10^{-3}$
Red	$6 \cdot 10^{-3}$	$1.13 \cdot 10^{-4}$	$1.02 \cdot 10^{-9}$	$3.0 \cdot 10^{-3}$
Green	$3 \cdot 10^{-3}$	$2.83 \cdot 10^{-5}$	$6.40 \cdot 10^{-11}$	$5.0 \cdot 10^{-3}$
Blue	$3 \cdot 10^{-3}$	$2.83 \cdot 10^{-5}$	$6.40 \cdot 10^{-11}$	$17.5 \cdot 10^{-3}$

4.3.2 Waterfall plots

Waterfall plots of the shaft and floating ring motion have been created and are shown in figures 4.21, 4.22 and 4.23. The results are similar to the results obtained with the shaft simulated as a point mass, as shown in the previous section. The frequencies which contribute most to the total motion are the synchronous frequency and two whirl frequencies; there is no supersynchronous frequency content. The waterfall plots of the floating ring, figure 4.21, and the shaft relative to the floating ring, figure 4.23, show that whirl 1 is the whirling frequency of the floating ring and whirl 2 is the whirling frequency of the shaft inside the floating ring.

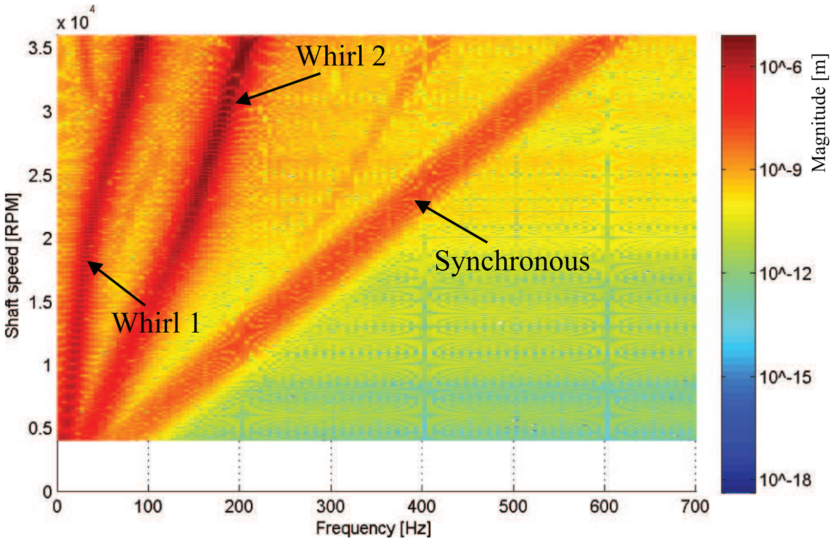

Figure 4.21: Waterfall plot of the position of the shaft at the floating ring bearing in x-direction

In this simulation no jumping behavior is seen, but this may occur at higher shaft rotational speeds and is not expected in the operating range of the demonstrator. The motion of the floating ring and the point of the shaft in the floating ring is displayed in figure 4.24. Due to the different whirl frequencies a spiraling effect can be seen.

4.3.3 Body displacement and velocity

The eccentricity of the shaft and floating ring is displayed in figure 4.25. With increasing shaft speed the unbalance force also increases, as can be seen in equation (2.4). During the first part of the run-up it is mainly the shaft which has moved out of the center position of the floating ring, the floating ring has not moved as much yet. Because the surface area of the outside of the floating is larger than the inside of the floating ring, ϵ_r will be smaller than ϵ_{s*} to obtain an equal force. However, when ϵ_{s*} increases, the reaction force on the inner

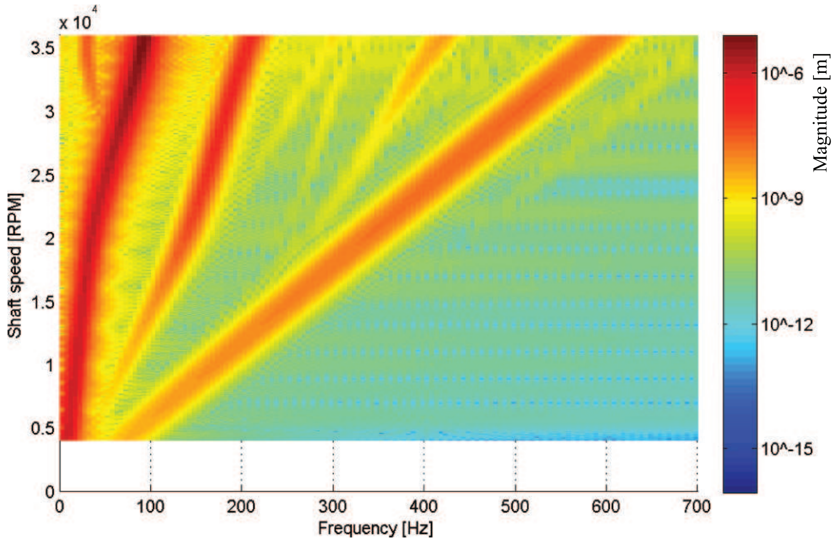

Figure 4.22: Waterfall plot of the position of the floating ring

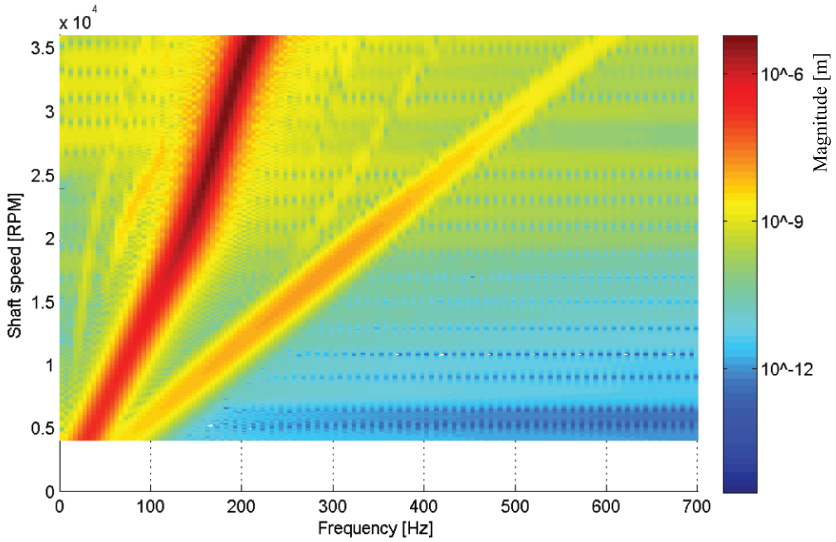

Figure 4.23: Waterfall plot of the position of the shaft relative to the floating ring

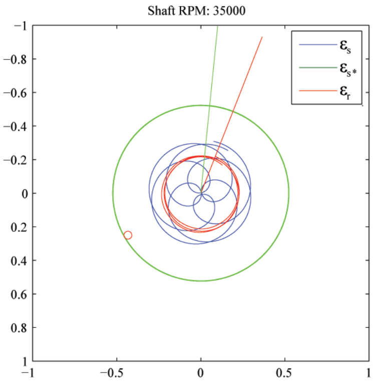

Figure 4.24: Trace of the movement of the shaft, floating ring and shaft motion relative to the floating ring. The red circle indicates the direction of the unbalance force at the time step of this configuration. The blue and green lines represent the directions of respectively ϵ_s and ϵ_{s^*}.

surface increases non-linearly due to the non-linear stiffness behavior of the oil film. This in turn causes ϵ_r to increase as well.

Near the end of the figure, at approximately 37kRPM a small jump is seen in ϵ_{s^*}. This jump is unfortunately at a shaft speed which is out of the range of the waterfall plot. The oscillating behavior of ϵ_s is caused by the difference in whirl frequencies of the shaft and floating ring.

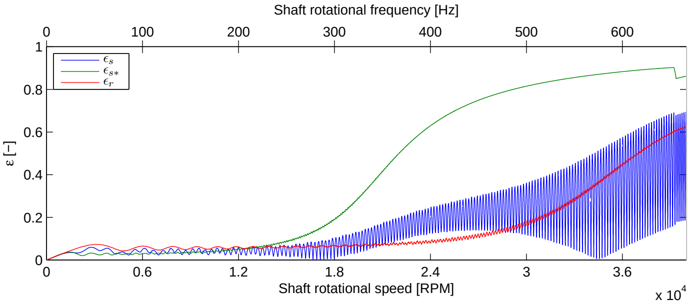

Figure 4.25: Eccentricities of the shaft (ϵ_s), floating ring (ϵ_r) and shaft relative to floating ring (ϵ_{s^*}) versus shaft rotational speed

The velocities of the shaft relative to the floating ring and the velocity of the floating ring itself in tangential and radial direction are shown in figures 4.26a to 4.26d. Figures 4.26b and 4.26d show that the sign of the tangential velocity of both bodies does not change. This indicates that the whirling direction stays the same. The jump mentioned in figure 4.25 is also seen in figures 4.26c and 4.26d.

The floating ring speed ratio is shown in figure 4.27. The ratio monotonically increases from 0 to 0.25 times the rotational speed and shows no eye-catching characteristics.

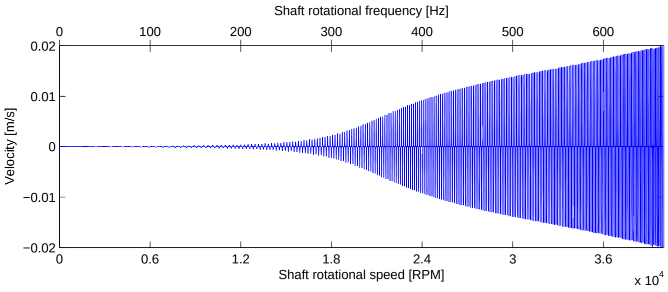

(a) Velocity of the shaft relative to the floating ring in radial direction

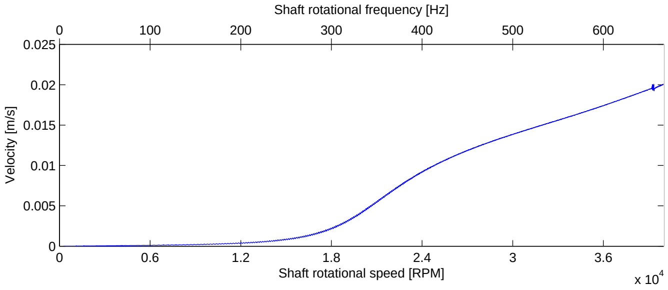

(b) Velocity of the shaft relative to the floating ring in tangential direction

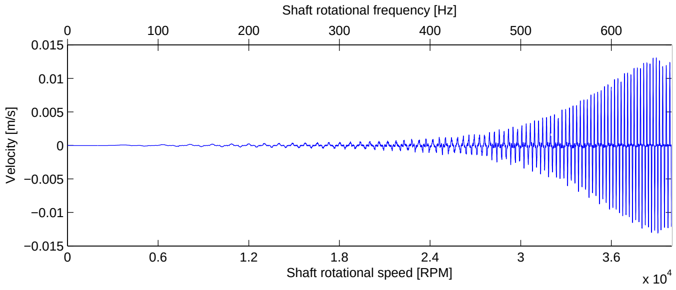

(c) Velocity of the floating ring in radial direction

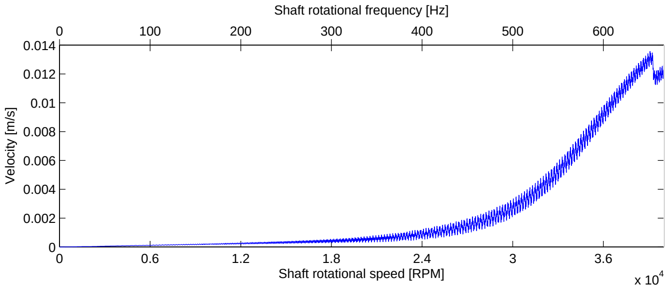

(d) Velocity of the floating ring in tangential direction

Figure 4.26: Velocities of the shaft and floating ring in radial and tangential directions

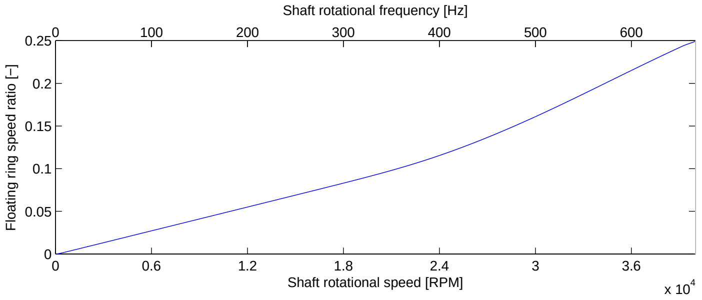

Figure 4.27: Ratio of the rotational speed of the floating ring to the speed of the shaft: $\frac{\omega_r}{\omega_s}$

4.3.4 Peak pressure development and fluid film forces

The peak pressure during the run-up and the resulting forces they generate are shown in figures 4.28 and 4.29. Both increase non-linearly with increasing shaft speed and a peak is seen at the jump at 37kRPM.

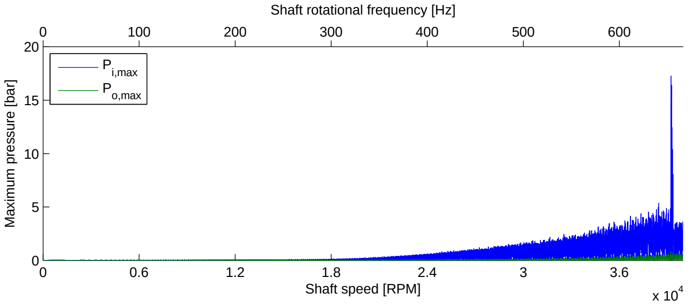

Figure 4.28: Peak pressures during the run-up in both the inner and outer oil film

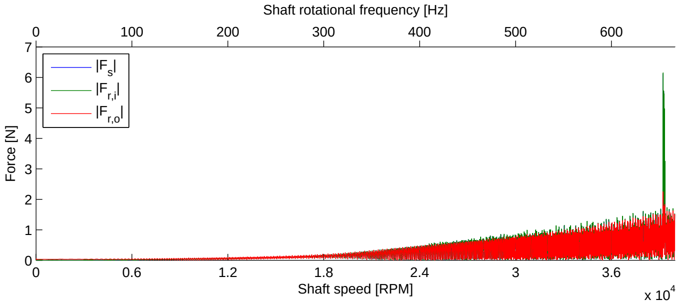

Figure 4.29: Force magnitude working on the shaft and the inner and outer surface of the floating ring

4.3.5 Comparison with the point mass simulation

The waterfall plots of the shaft of the demonstrator simulation and point mass simulation are shown in figures 4.30 and 4.31. The point mass simulation waterfall plot has been zoomed in so it can be compared with the demonstrator simulation waterfall plot. It can be seen that in both situations the whirl frequencies are large contributors to the total motion. The whirl frequencies of both simulations are in the same range, but show slightly different behavior. With increasing shaft rotational speed, whirl 1 of the demonstrator simulation becomes larger than whirl 1 of the point mass simulation. Regarding whirl 2 it is the other way around; the whirl 2 frequency of the point mass simulation grows larger than whirl 2 of the demonstrator simulation when the shaft speed is increased.

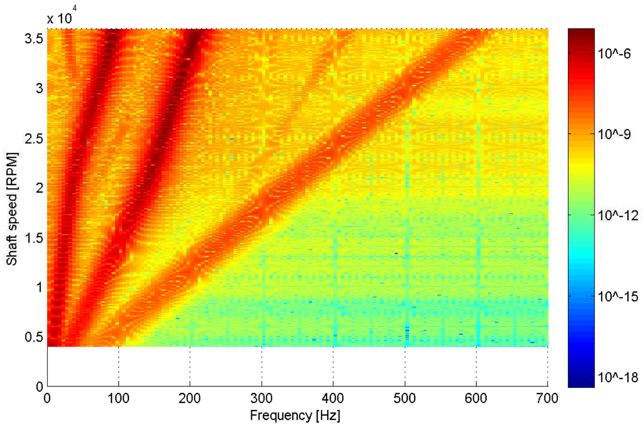

Figure 4.30: Shaft waterfall plot of the demonstrator model

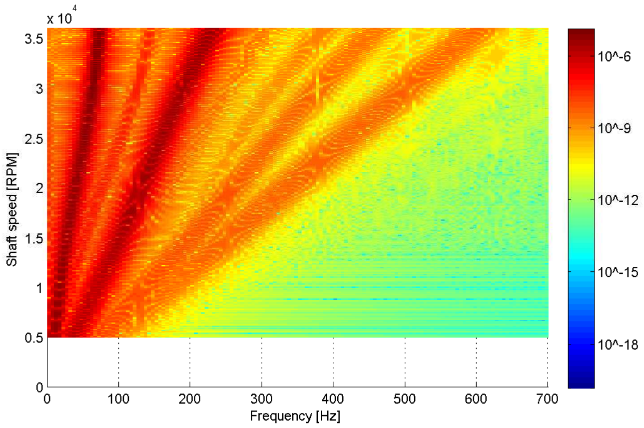

Figure 4.31: Zoomed in waterfall plot of the shaft of the point mass simulation, figure 4.7

4.4 Experimental results

In this section the measurement data will be discussed which is obtained with the setup from chapter 3. Run-up tests with shaft rotational speeds from approximately 2kRPM to 40kRPM have been performed and one of the measurements has been chosen to discuss in this section. Figure 4.32 shows the shaft rotational speed in time. The sensor lost the signal at a speed of 37kRPM.

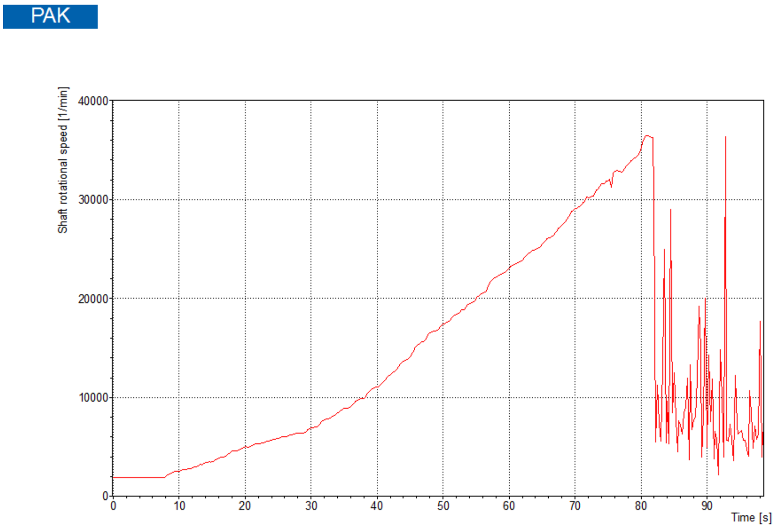

Figure 4.32: The measured shaft rotational speed; note that the measurement equipment lost track of the shaft rotational speed after 82s, at 37kRPM.

In section 4.4.1 the measured signals are discussed. An analysis of the frequency content of the measured signals is done in section 4.4.2.

4.4.1 Motion analysis

During the experiments the displacement has been measured of four positions of the shaft, one position of the floating ring, the acceleration level of the cartridge and the rotational speed of the shaft. The measured signals of the displacement sensors which measured in the x-direction are shown in figure 4.33. Only the dynamic part is measured; the displacement for all sensors at t = 0s is set to 0m. It can be seen that the amplitude of the shaft deflection close to the ball bearing decreases over time, while the deflection at the end of the shaft increases over time. Both signals show some additional amplitude fluctuations at $32s$, $68s$ and $77s$. The displacement level of the floating ring is misleading and can not be used in this way. When one of the oil feeding holes passes the sensor, the sensor measures “through” the hole and registers this as a large displacement. With post-processing the floating ring data does provide useful information, which will be discussed in section 4.4.2.

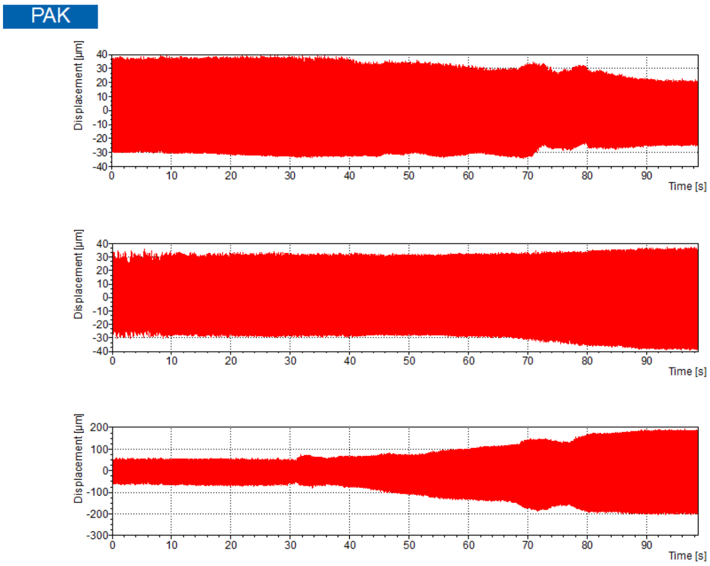

Figure 4.33: The dynamic part of the measured signal from the displacement sensors close to the ball bearing (top), at the floating ring (middle) and at the end of the shaft (bottom)

Because the displacement of the shaft has been measured with orthogonal pairs of sensors, circle diagrams can provide insight in the mode shapes of the shaft. In figure 4.34 circle diagrams at three different points in time are shown. The first observation is the shape of the motions which have been measured. The shapes are asymmetric and show repeating spikes and dips, especially at the ball bearing side at 17.4kRPM and 29.1kRPM. When comparing the motions of the shaft at the two position at 17.4kRPM, it appears that they have the same shape but a phase shift of approximately 180 degrees. This is the case at every point in the measurement.

The amplitudes of both motions in x- and y-direction are plotted in figure 4.35. The amplitude of the motion at the end of the shaft increases when the shaft rotational speed increases, while the amplitude of the shaft motion close to the ball bearing is much more stable.

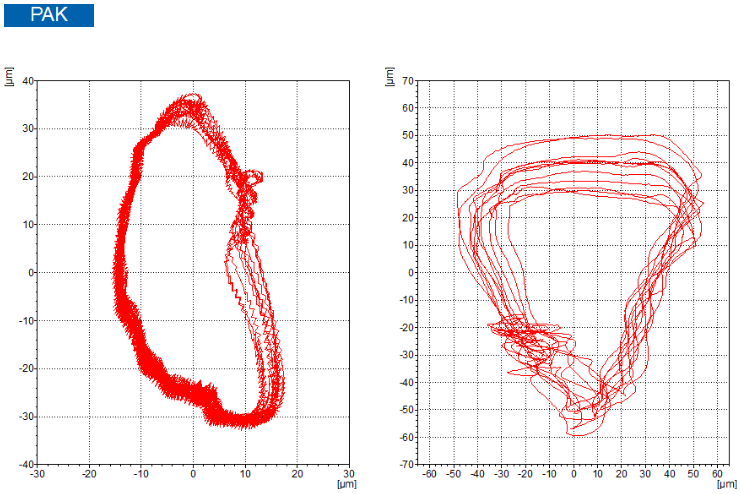

(a) Motion of the shaft measured at 6900RPM (t = $30 - 30.1s$)

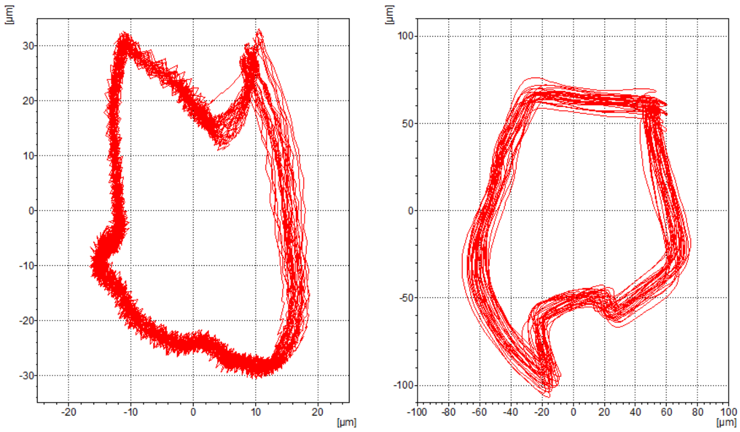

(b) Motion of the shaft measured at 17400RPM (t = $50 - 50.1s$)

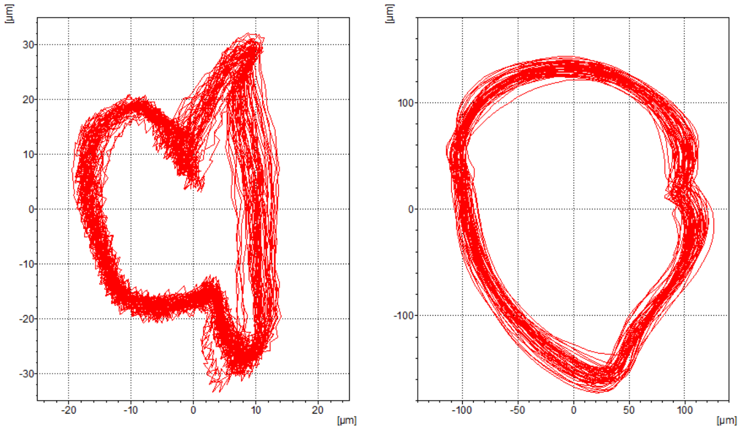

(c) Motion of the shaft measured at 29100RPM (t = $70 - 70.1s$)

Figure 4.34: Circle diagrams of the motion of the shaft measured close to the ball bearing (left) and at the end of the shaft (right).

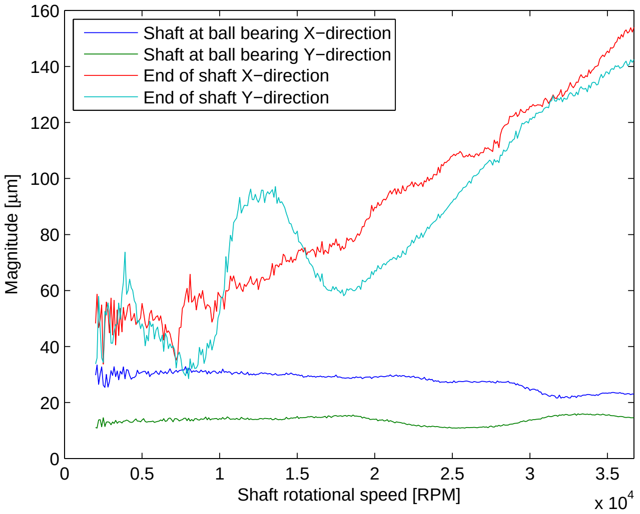

Figure 4.35: Level of the vibration of the shaft measured by the different sensors

4.4.2 Frequency content analysis

To identify the frequency content of the measured displacements, waterfall plots are created. In this section only the waterfall plots of the sensors which measure in the x-direction are shown because the waterfall plots of the sensors which measured in the y-direction show equal characteristics. The waterfall plots of the quantities measured in the y-direction are shown in appendix E.

Starting with the shaft motion, figure 4.36 and figure 4.37 show the waterfall plots of the shaft motion respectively close to the ball bearing and at the end of the shaft. In both cases the synchronous frequency, or first order, contributes most to the total displacement. In the supersynchronous area of both waterfall plots the higher orders are visible, with the second to fourth the most notable. Another phenomenon which at first looks remarkable are the constant frequencies which are present throughout the whole shaft rotational speed range in figure 4.37. These frequencies originate from the oil pump which is connected rigidly to the same rig as the test setup.

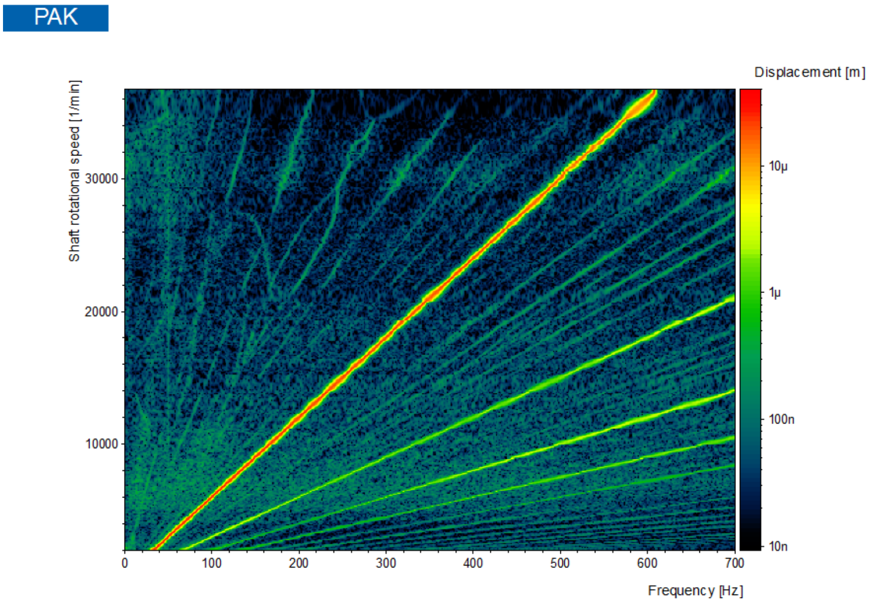

Figure 4.36: Waterfall plot of the measured signal of the shaft near the ball bearing

The third interesting waterfall plot is figure 4.38 and contains the waterfall plot of the displacement of the FRB. The dominating frequency line in this plot is mostly supersynchronous. The origin of this frequency line is the measurement of the oil feeding holes in the floating ring bearing. When one of these holes passes the sensor it overloads; the depth of the hole is 2.5mm, which is larger than the measuring range of the sensor. Because the output of the sensor is maximum when it measures an oil feeding hole, the frequency of the passing of the feeding holes is the dominating frequency in the waterfall plot. Since there

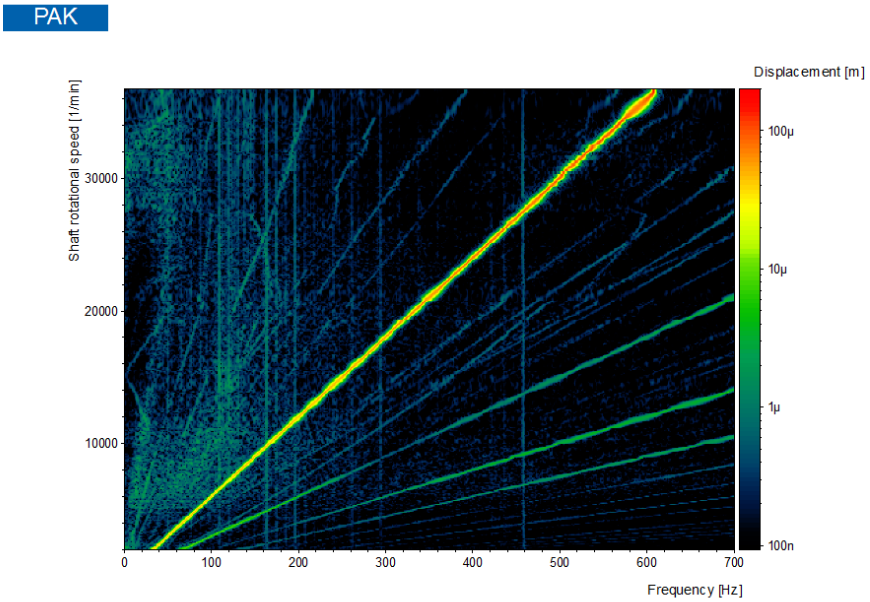

Figure 4.37: Waterfall plot of the measured signal at the end of the shaft

are six feeding holes in the floating ring, the measured rotational frequency of the floating ring is the feeding hole frequency divided by six; a frequency line which is also clearly present in the waterfall plot. This first order floating ring rotational speed frequency line in the waterfall plot originates from the unbalance level of the floating ring.

Floating ring rotational speed

The floating ring rotational speed, which can be derived from figure 4.38, is shown together with the shaft rotational speed in figure 4.39a. The floating ring speed increases over time, but shows jumping behavior at approximately 56s (21kRPM shaft speed) and 68s (28kRPM shaft speed). The sudden change in rotational speed of the floating ring at t $=$ 68s may be connected to the amplitude change which was seen in the throughput data of figure 4.33. An effect of the jump at t $=$ 56s can not be seen in the throughput data. The ratio of floating ring to shaft rotational speed is displayed in figure 4.39b. In this figure, one thing that stands out is that the FRSR decreases after the first jump and increases again after the second jump.

Order analysis

Another way of displaying frequency content is relating it to the orders of a certain frequency line and is called order analysis. Figure 4.40 shows how the

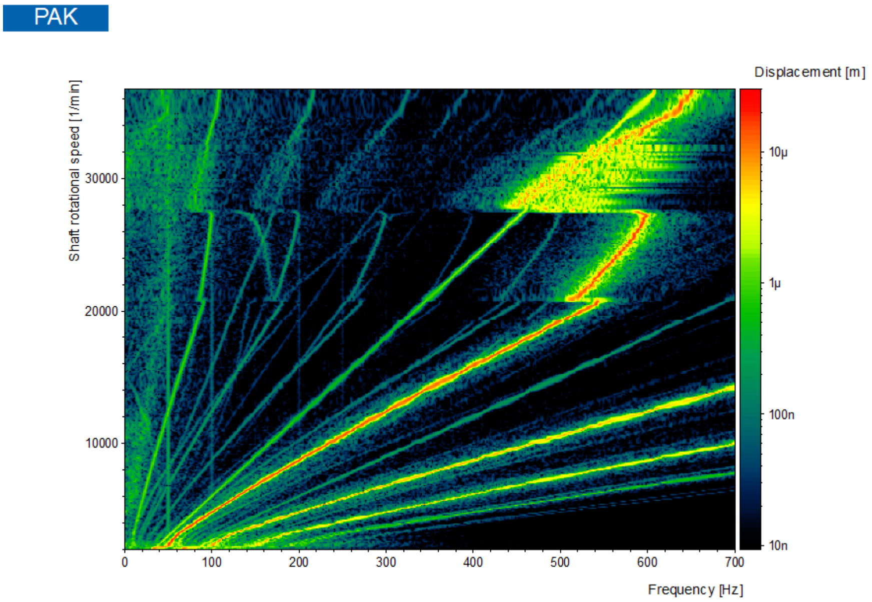

Figure 4.38: Waterfall plot of the measured signal of the floating ring

frequency content is related to the rotational speed of the floating ring. The first to fourth orders of the shaft rotational speed have been filtered out to have more contrast between the other frequencies. The figure shows that the frequency content of the floating ring displacement sensor mainly contains the first and sixth order of the floating ring rotational speed. This makes sense because, as previously mentioned, these are respectively the floating ring rotational speed and the frequency of feeding holes passing the sensor.

To investigate the influence of the floating ring on the shaft motion an order analysis is shown in figure 4.40, with again the shaft rotational speed on the vertical axis and the floating ring rotational speed orders on the horizontal axis. Again, the first to fourth shaft rotational speed orders have been filtered out for visibility purposes. The figure shows visible, but small contributions of the first and sixth orders. This means that the unbalance of the floating ring and the passing of the oil feeding holes influence the displacement of the shaft.

In the subsynchronous region of figure 4.36 a lot of frequency content looks to be linearly dependent of the shaft rotational speed at first sight. An order analysis of the displacement of the shaft measured close to the ball bearing is shown in figure 4.42. On the horizontal axis an order range from zero to one is displayed, which is the subsynchronous part. This order analysis shows that the subsynchronous content is not linearly dependent of shaft speed; i.e., in the order analysis there is no content which has a constant order throughout the run-up measurement. A curious phenomenon occurs after $18kRPM$ around the 0.5th order. Two frequency lines start at the 0.5th order and symmetrically move away from the order line and return to the 0.5th order at $29kRPM$. A source

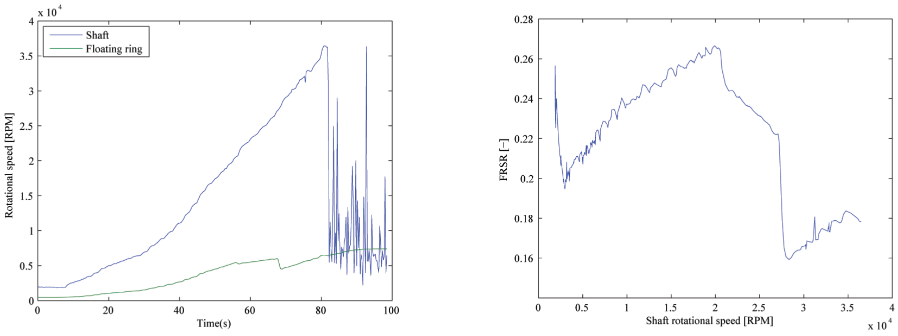

(a) Shaft and floating ring rotational speed in time

(b) Floating ring speed ratio versus shaft rotational speed

Figure 4.39: Measured rotational speed characteristics of the shaft and floating ring

of the 0.5th order line could be the “whirling” of the balls in the ball bearing. Due to the geometry it takes two rotations of the shaft to complete one rotation of the balls in the ball bearing, which therefore is the 0.5th order. However, the 0.5th order is not visible throughout the whole run-up and therefore the possible origin to be the ball bearing is just speculation.

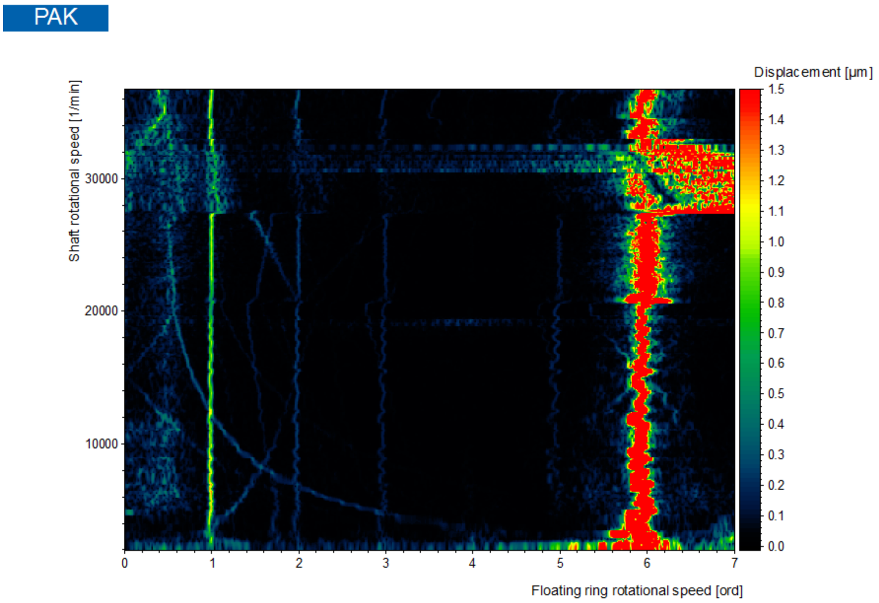

Figure 4.40: Floating ring order analysis of the signal of the floating ring. Note that the amplitude of the 6th order is mostly larger that the maximum value indicated by the color bar. This is done because of displaying purposes.

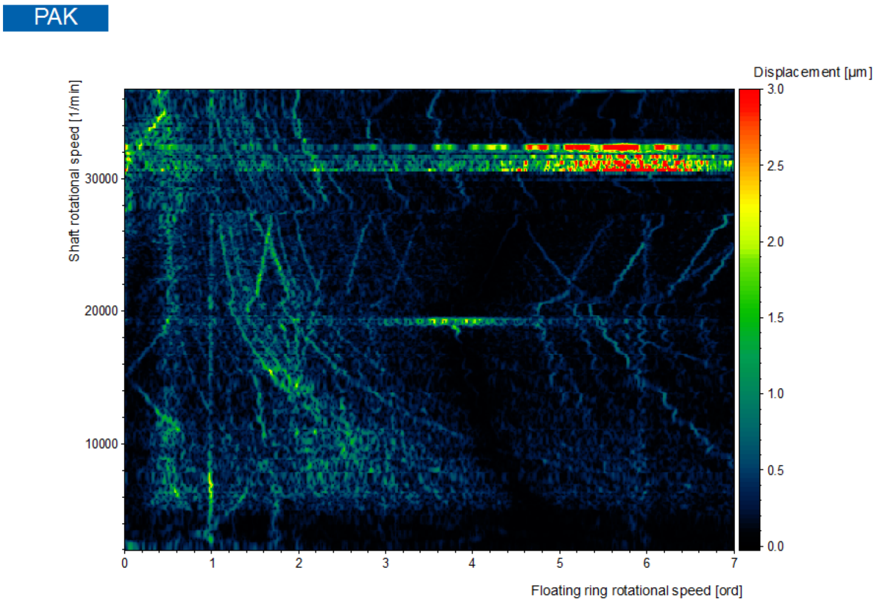

Figure 4.41: Floating ring order analysis of the displacement of the end of the shaft

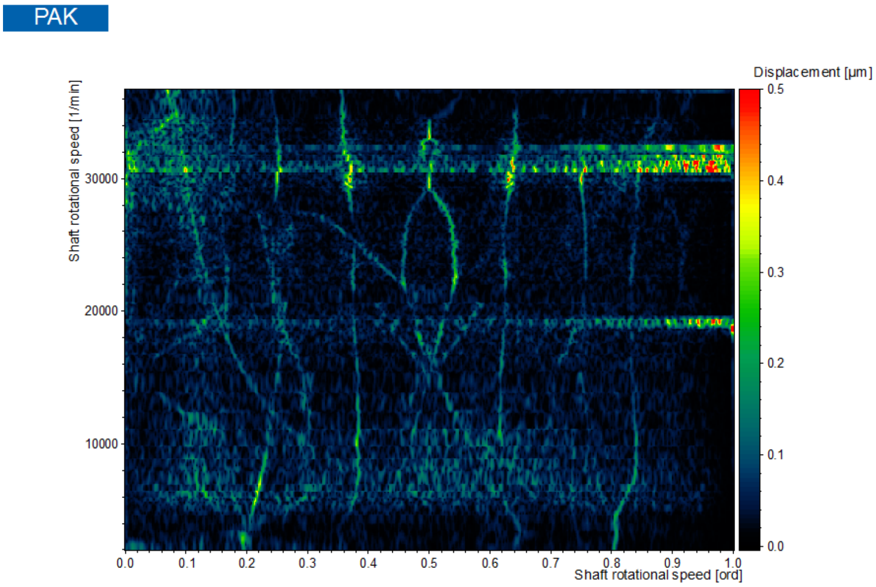

Figure 4.42: Subsynchronous order analysis of the displacement of the shaft close to the ball bearing

4.5 Results discussion

In this section the theoretical and experimental results will be discussed. This section is split in two. In 4.5.1 the results of the point mass simulation are compared to the turbocharger measurement done by Eling.[1] In the second section the theoretical and experimental results of the demonstrator are compared.

4.5.1 Comparison: Point mass simulation and turbocharger measurements

The waterfall plots of the turbocharger measurement shown in figure 1.2 and a waterfall plot resulting from the point mass simulation, shown in figure 4.7, are shown again in figures 4.43 and 4.44. Although the waterfall plots are not entirely comparable, because both are different systems, they do show some comparable behavior. Whirling behavior which is seen in the subsynchronous region of the measured waterfall plot is, although not at the same frequencies, also present in the theoretical model. Jumping behavior is also seen during a run-up simulation and understanding is created what happens before and after the jump.

The turbocharger measurement shows two jumps, one at 70kRPM and a jump at 175kRPM, while the simulation only shows one jump. Although the measurement contains a lot of subsynchronous dynamics, only one frequency line stands out. This is the whirl frequency between the two jump speeds. However, around the whirl frequency which is clearly seen a phenomenon called the beat phenomenon is seen.[10] The beat phenomenon occurs when the whirl frequency is not a unit fraction of the synchronous frequency. The beat phenomenon around the visible whirl frequency is indicated by “Beating 2” in figure 4.43. Another beat like phenomenon is seen in the subsynchronous area and is denoted by “Beating 1”. This may indicate, although not visible, the presence of a second whirl frequency.

Before the first jump there is no subsynchronous content which really stands out; after the second jump the whirl frequency jumps to approximately 350Hz, but decays in amplitude. A clear difference between the simulated and measured whirl is that the simulated whirl frequency increases much more with increasing shaft frequency than the measured whirl. The measured whirl frequency stays between 600 and 900Hz.

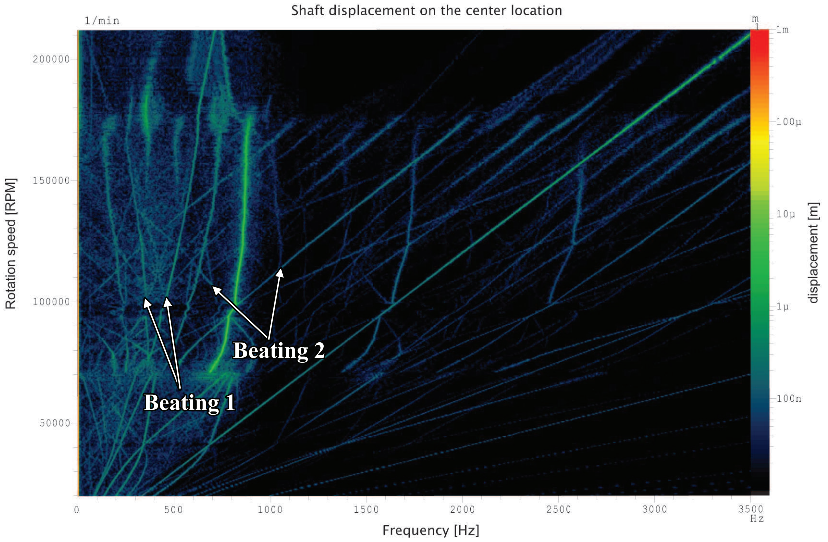

Figure 4.43: Figure 1.2; measured waterfall plot of turbocharger shaft motion

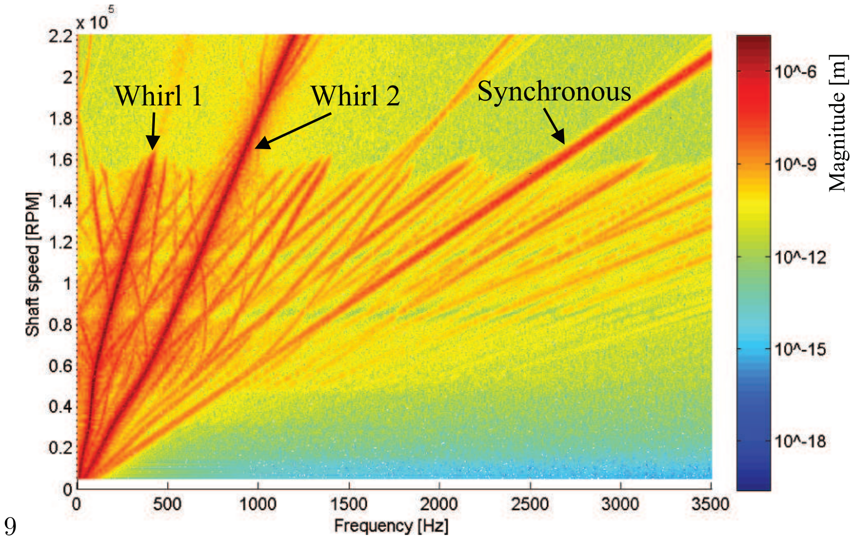

Figure 4.44: Figure 4.7; theoretical waterfall plot of a FRB simulation with the shaft modeled as a point mass

4.5.2 Comparison: Theoretical and experimental demonstrator results

In this section some of the results previously shown in sections 4.3 and 4.4 will be shown side by side. In figures 4.45 and 4.46 the theoretical and experimental waterfall plots of the demonstrator are shown. Both waterfall plots show the synchronous frequency, but there are no further clear similarities. The theoretical results show two whirl frequencies, but whirling does not clearly show in the experimental results.

When the circle diagrams of the theoretical and experimental results are compared, the same conclusion as with the waterfall plots is drawn. Due to the absence of whirling in the test setup, the circle diagrams look different. The shape of the shaft motion of the demonstrator close to the ball bearing, the left figure in 4.47b, is a shape which is not an explainable result if the demonstrator is in the perfect situation as it is modeled. The odd shape may be the result of physical imperfections in the demonstrator, such as misalignment of the demonstrator and drive shafts, a bended demonstrator shaft or ball bearing imperfections.

The floating ring speed ratios are shown in figure 4.48. The range of the simulated and measured ratio are comparable, however, the simulated ratio is monotonically increasing, while the measured ratio shows non-monotonic behavior.

The theoretical and experimental results show little similarities. Simulation showed whirling while this effect was absent in the experiments. The experimental results, especially the circle diagrams, indicate that the experimental configuration is probably far from the perfect situation which was simulated. Although the theoretical model could not be verified using this experimental setup, useful results have been obtained with the experiments. The method of measuring the floating ring displacement and rotational speed has proven to be feasible.

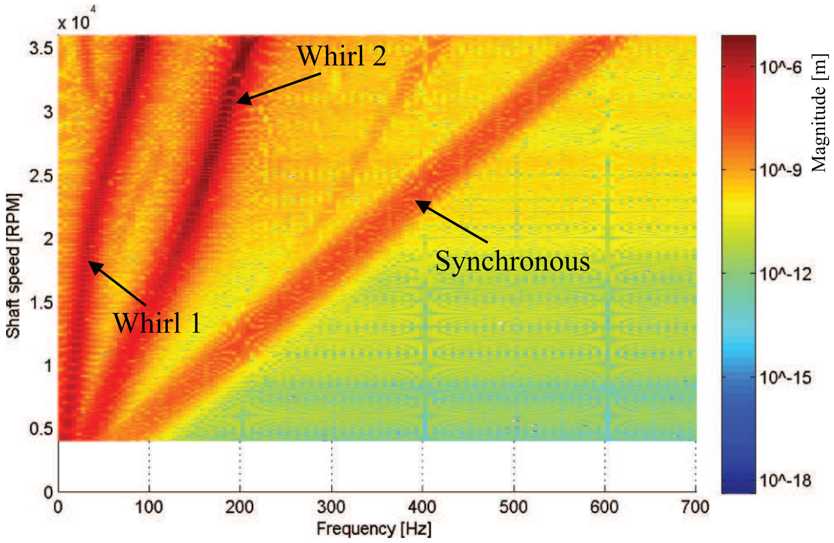

Figure 4.45: Figure 4.21; theoretical demonstrator waterfall plot

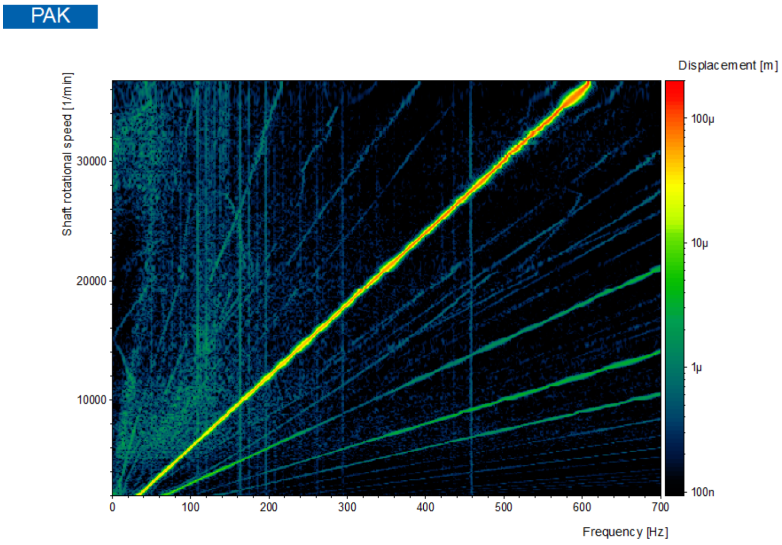

Figure 4.46: Theoretical and experimental waterfall plots of the demonstrator

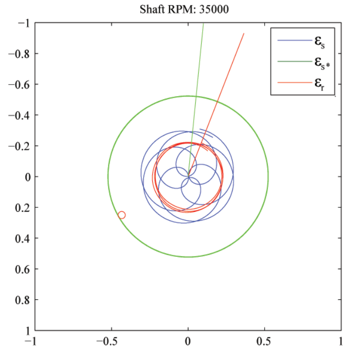

(a) Figure 4.24; motion of the shaft and floating ring at 35000RPM

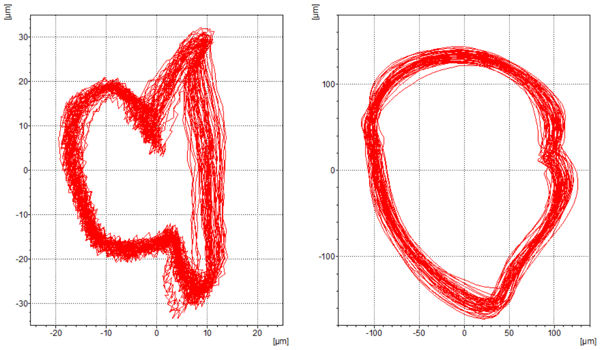

(b) Figure 4.34c; shaft motion at two locations of the demonstrator at 29100RPM

Figure 4.47: Shaft motion of the theoretical and experimental results of the demonstrator. The blue trace in figure 4.47a should be compared to the circle diagrams in figure 4.47b

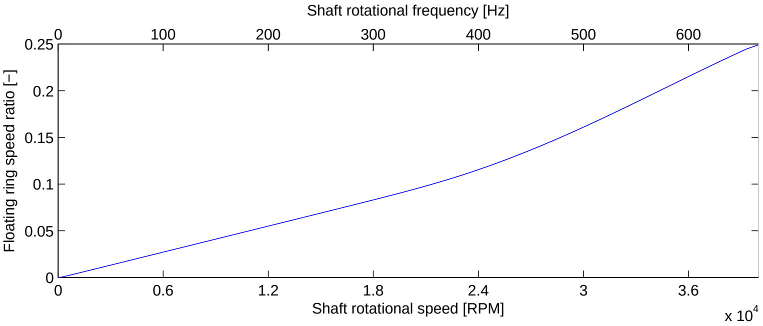

(a) Figure 4.27; floating ring speed ratio of the demonstrator simulation

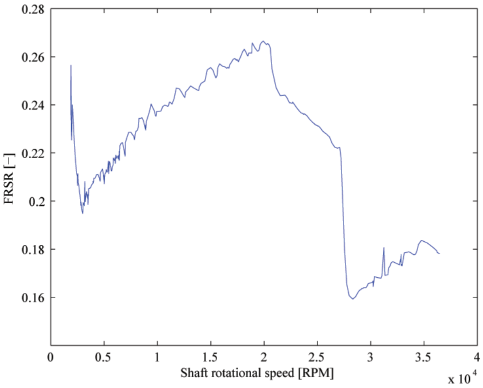

(b) Figure 4.39b; measured floating ring speed ratio of the demonstrator

Figure 4.48: Floating ring speed ratios of the theoretical and experimental results of the demonstrator

4.6 Sensitivity analysis

A first sensitivity analysis has been performed to see which effect changes in geometry and oil viscosity have on the behavior of the FRB.

The results of the simulations have been summarized in table 4.6. In this table the jump speed is shown, the whirl ratios and the floating ring speed ratio. The whirl 1 and 2 ratios are defined by equation 4.7. In this equation ω_1 and ω_2 represent the whirl frequencies at a shaft frequency ω_s. Several simulations failed due to tolerance errors; the ODE solver could not meet the tolerance requirements, not even when the smallest time step the computer could handle was used.

$$\mathrm{WR}_i = \frac{\omega_i}{\omega_s}, \qquad i = \{1, 2\} \tag{4.7}$$

Table 4.6: Parameter values used in the point mass simulation of section 4.2

Simulation	Jump speed [kRPM] ([Hz])	Whirl 1 ratio at $\omega_s = 1$kHz	Whirl 2 ratio at $\omega_s = 1$kHz	FRSR range
Reference	160 (2667)	0.105	0.400	$[0 - 0.33]$
Larger L_i	No jump	0.120	0.365	$[0 - 0.35]$
Larger L_o	160 (2667)	0.100	0.400	$[0 - 0.29]$
Smaller C_i	-	Simulation	failed	-
Larger C_i	100 (1667)	0.105	0.395	$[0 - 0.30]$
Smaller C_o	125 (2083)	0.095	0.400	$[0 - 0.32]$
Larger C_o	-	Simulation	failed	-
Lower μ_i, μ_o	210 (3500)	0.120	0.380	$[0 - 0.30]$
Higher μ_i, μ_o	-	Simulation	failed	-

The jump speed is largely influenced by the change of parameters, while the whirl ratios seem to be barely influenced by the change of parameters. The effects on the floating ring speed ratio are small, but feasible explanations are listed below.

- **Larger L_i:** Increasing the inner floating ring width L_i causes an increase of the inner floating ring surface. A larger surface increases the viscous torque. Because the inner torque is the driving torque of the floating ring rotation, the maximum FRSR increases.

- **Larger L_o:** A larger L_o results in a larger outer surface of the floating ring. This in turn leads to a higher viscous torque, increasing the drag and therefore lowering the maximum floating ring speed ratio.

- **Larger C_i:** A larger inner gap likely leads to a smaller $\frac{du}{dh}$, which is a term in the viscous drag equation. When this term decreases, the viscous drag decreases which results in a smaller driving torque.
- **Smaller C_o:** When the outer gap is decreased, the $\frac{du}{dh}$ term is increased. The effect is a higher drag torque on the outer surface of the floating ring, lowering the FRSR.
- **Lower μ:** Since viscous drag is linearly dependent of viscosity, a change in viscosity does not directly influence the FRSR. A lower viscosity may, however, allow larger eccentricities of the shaft and floating ring. This in turn influences $\frac{du}{dh}$ in a way that the maximum FRSR decreases.

Chapter 5

Conclusions and recommendations

In this chapter the conclusions from this research and recommendations for future research are shown. Section 5.1 shows the conclusions from the modeling and testing which has been done. In 5.2 recommendations for further research are done to further increase the understanding of the dynamics of turbochargers.

5.1 Conclusions

In the first chapter of this thesis the goal of the research was formulated as to create a realistic floating ring bearing model to be able to investigate the dynamics of a FRB under automotive turbocharger conditions. A parametrized FRB model has been made based on Reynolds' equation, which is used to calculate the pressure distribution in a fluid film. Because the model is parametrized, different geometries and conditions can be simulated to see the effect of changes on the dynamic behavior. A simplified cavitation model has been used, which assumes the pressure and viscosity to be zero in the cavitated region of the oil films. A thermal model has not been implemented; only the viscosity of the oil is dependent of the temperature.

The FRB model shows the whirling phenomenon as well as jumping behavior from one mode shape to another. Visualization of the simulation provides understanding of these mode shapes. Whirling and jumping behavior has also been seen in measurements of shaft motion of turbochargers under operating conditions.

The results of the simulation of the demonstrator and the measurements of the demonstrator do not match. In the simulation whirling frequencies were contributing significantly to the total motion, while in the measurement there were no notable contributing frequencies besides the synchronous frequency. The results of the measurements lead to the suspicion that the test setup is far from the perfect situation which has been simulated. This could be caused by, for example, alignment imperfections of the driving and driven shafts or ball bearing imperfections. Because of this suspicion the model has not been validated nor proven wrong.

Although the demonstrator did not validate the theoretical model, the measurements led to some useful results. The measurement method of sensing “through” a small amount of bearing housing material with an eddy-current sensor, has proven to be feasible. Using this measurement method the displacement of the floating ring and the floating ring rotational speed have been measured. The model has yet to be validated, but this measurement method can be used in another validation attempt.

5.2 Recommendations

A first step in the realistic modeling of a FRB has been done, but further modeling can be done to improve the simulation results.

Thermal effects are not taken into account in the model presented in this thesis. Temperature is an influencing factor of for example the viscosity of the oil and expansion of material. It is also possible that the oil films both have a different temperature and therefore a different viscosity. It is even possible that the temperature is not uniform within an oil film. A thermal model which predicts the temperature in the oil films would improve the estimation of the viscosity and therefore improve the results of the simulation.

Another aspect of the oil film which has been simplified is the effect of cavitation. In this model, the pressure of the oil film which is lower than the vapor pressure is assumed to be 0Pa. In the axial direction of a FRB there may be regions in the oil film which have cavitated and regions which are not cavitated. This effect is shown for a journal bearing in figure 5.1. Integrating a cavitation model will increase the definition of the fluid films.

Figure 5.1: Cavitation in a journal bearing [13]. A clear difference can be seen where the oil film has cavitated (the metal surface of the shaft can be seen) and where the oil film is still intact.

A third possible improvement of the model is to include tilting of the floating ring. In the current model the surfaces of the floating ring are always parallel to the surfaces of the shaft and bearing housing. In reality the floating ring and shaft may tilt and cause the oil film thickness to be non-uniform in the z-direction. The tilt of the shaft and floating ring can cause a moment and larger force on the shaft due to the non-linear characteristic of the pressure film equation.

Measurements of the shaft and floating ring dynamics showed that the direct influence of the oil feeding holes in the floating ring on the dynamics of the shaft were very limited; the amplitude of the sixth order floating ring rotational frequency is very small in the waterfall plot of the shaft vibrations. Because the oil feeding holes are meant to transfer oil from the outer film to the inner film, this also means that there may be “communication” between the inner and outer pressure distributions. In other words; the pressure on one side of a feeding hole may influence the pressure on the other side of the feeding hole. Whether or not this communication is significant to the pressure distributions in the oil films is another possible point of interest.

A recommendation on validation of the model is to build a cartridge out of polycarbonate, glass or a similar material which can be used with the measurement method explained. With such a test setup the floating ring dynamics can be measured under the operating conditions of a turbocharger. The FRB model should be integrated in the turbocharger rotor model of Eling[1] so the experimental and theoretical results can be compared.

The evaluation of the model may take, depending on the simulation settings, up to eight hours. To become a more useful tool for bearing designers it is preferable to reduce the evaluation time. Speed improvements may be achieved by improving the Matlab code or by using look-up tables for bearing configurations of shaft and floating ring positions which can be pre-calculated. An extensive sensitivity analysis of the design parameters can be done with this model and can point designers in the right direction of bearing improvement. The effect of parameter changes on for example vibration levels and jump speeds will give interesting information on the behavior of FRB's.

Bibliography

[1] Eling, R. The structural dynamics of a turbocharger rotor-bearing system. Master's thesis, Delft University of Technology, 2009.

[2] Exxon Mobil Corporation. *Mobil 1 5W-30 product sheet*, 2007.

[3] http://www.superstreetonline.com. visited 16-03-2010.

[4] Knoll, Seemann, Proppe, Koch, Backhaus, and Boyaci. Run-up of turbocharger rotors in nonlinearly modelled floating bush bearings. *Motortechnische Zeitschrift 71* (2010), 50–55.

[5] Lalanne, M., and Ferraris, G. *Rotordynamics prediction in Engineering.* Wiley, 1998.

[6] Lion Precision. Minimum recommended target thickness. Tech. rep., Lion Precision, 2008.

[7] The MathWorks Inc. *MATLAB R2010b Manual - ODEset error control properties.*

[8] Micro-Epsilon. Precise non-contact displacement sensors. Tech. rep., Micro-Epsilon, 2009.

[9] Mitsubishi Turbochargers. Turbowiki. Internal information source, 2010.

[10] NatHaz modeling laboratory. http://www.nd.edu/~nathaz/research/Swaroop_files/chapter4.pdf.

[11] Newkirk, B., and Grobel, L. Oil film whirl: A non-whirling bearing. *ASME transactions 56* (1934), 607–615.

[12] Newkirk, B., and Taylor, H. Shaft whipping due to oil action in journal bearings. *General Electric Review 28* (1925), 559–568.

[13] San Andrés, L. Lecture notes of modern lubrication theory, 2010.

[14] Schweizer, B. Total instability of turbocharger rotors - physical explanation of the dynamic failure of rotors with full-floating ring bearings. *Journal of sound and vibration 328* (2009), 156–190.

[15] Shaw, M., and Nussdorfer, T. An analysis of the full-floating journal bearing. *NASA Report NACA-RM-E7A28a* (1947).

[16] Trippett, R., and Li, D. High-speed floating ring bearing test and analysis. *ASLE transactions 27* (1984), 73–81.

[17] White, F. *Fluid Mechanics.* McGraw-Hill, 2003.

Appendix A

Turbocharger nomenclature

A.1 Turbo nomenclature

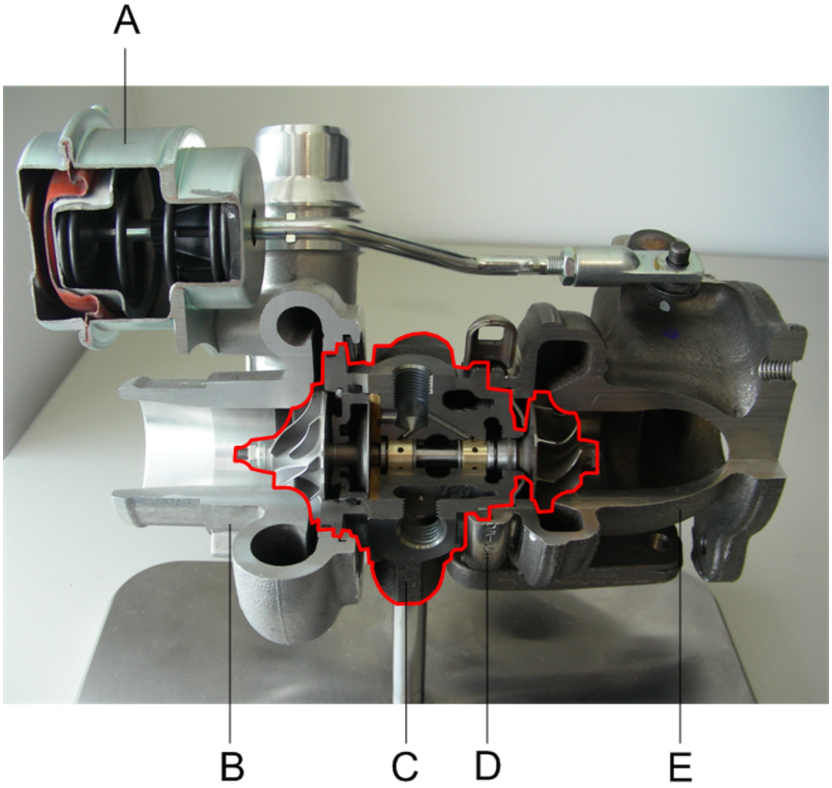

Figure A.1: General component names of a turbocharger [9]

Table A.1: Turbocharger component names

A	Actuator
B	Compressor cover
C	Cartridge assembly (outlined in red)
D	V-clamp
E	Turbine housing

A.2 Cartridge nomenclature

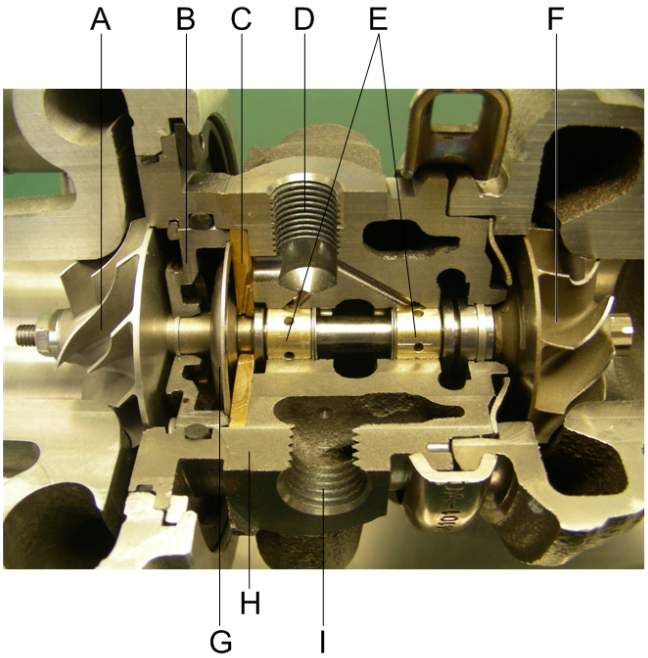

Figure A.2: Parts of the cartridge assembly [9]

Table A.2: Cartridge component names

A	Compressor wheel
B	Assembly insert
C	Axial bearing
D	Oil inlet
E	Floating ring bearings
F	Turbine rotor
G	Oil deflector
H	Bearing housing
I	Water cooling inlet

A.3 Floating ring geometry nomenclature

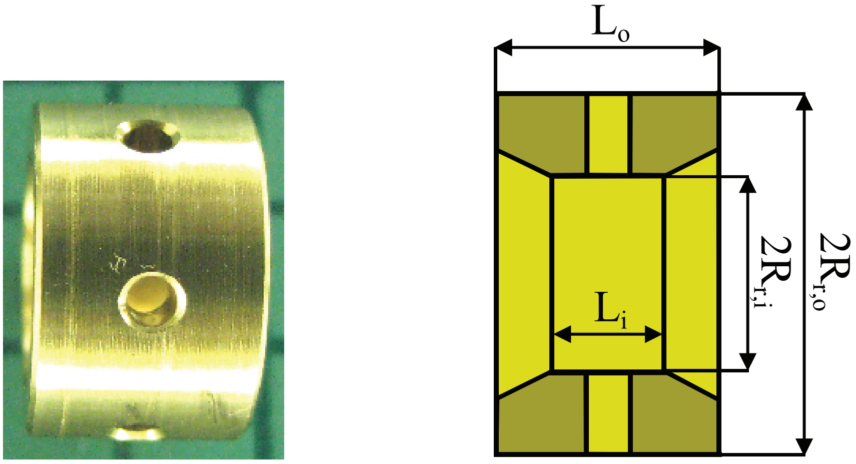

(a) Photograph of a floating ring

(b) Cross section of the floating ring with important geometry labeled

Figure A.3: The floating ring

A floating ring is shown in figure A.3a. A cross-section with the most important geometry labeled is shown in figure A.3b.

Appendix B

Modeling details

B.1 Journal bearing nomenclature

This section describes the nomenclature used throughout this appendix. Figure B.1 shows the coordinate system and the symbols used.

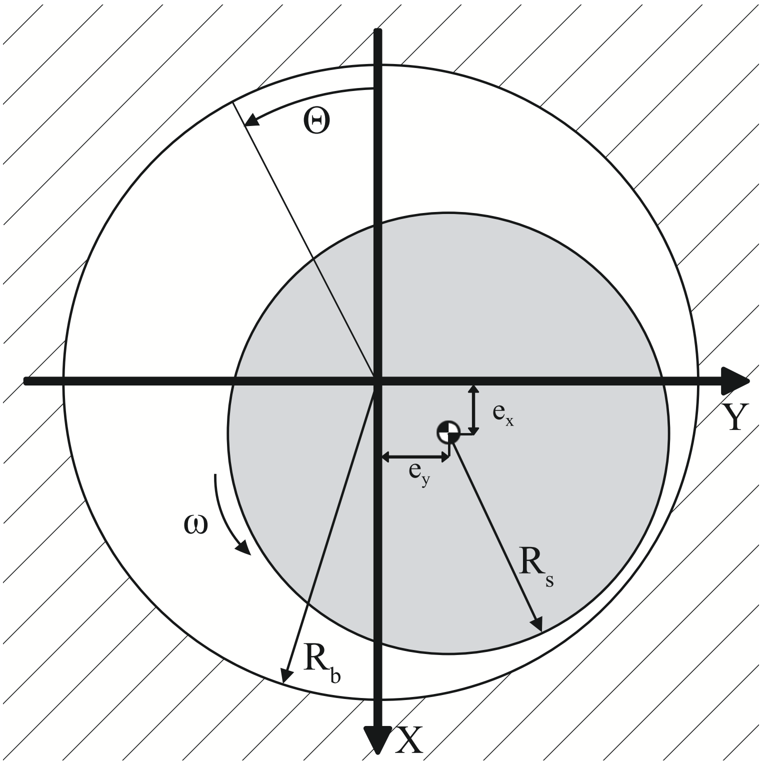

Figure B.1: Journal bearing coordinate system and units. Note that the dimensions are not to scale.

B.2 Fluid film forces

This section will show the derivation of the fluid film pressure equation of a plain journal bearing. In this context, the word “plain” indicates that features like lubricant feeding holes are not taken into account. The equation is based on the Reynolds equation of classical lubrication theory. This equation is valid for a thin film flow of a Newtonian, inertialess, isoviscous fluid. A derivation of the Reynolds equation is given by San Andrés [13]. The derivation of the fluid film pressure equation is also based on the work of San Andrés. In B.2.2 it is shown how the fluid film pressure equation is used to obtain the forces acting on the journal originating from the pressure in the fluid film.

B.2.1 The fluid film pressure equation

The Reynolds equation is described by

$$\frac{\partial}{\partial x}\left(\frac{\rho h^3}{12\mu}\frac{\partial p}{\partial x}\right)+\frac{\partial}{\partial z}\left(\frac{\rho h^3}{12\mu}\frac{\partial p}{\partial z}\right)=\frac{\partial}{\partial t}\rho h+\frac{1}{2}\frac{\partial}{\partial x}\rho h U \tag{B.1}$$

Because the clearance to journal ratio is very small, i.e. $\frac{C}{R} \ll 1$, the substitution $\delta x = R\delta\Theta$ can be made. Substitution of $\delta x = R\delta\Theta$, defining journal surface speed as $U = \omega R$ and dividing B.1 by ρ leads to

$$\frac{1}{R^2}\frac{\partial}{\partial\Theta}\left(\frac{h^3}{12\mu}\frac{\partial p}{\partial\Theta}\right)+\frac{\partial}{\partial z}\left(\frac{h^3}{12\mu}\frac{\partial P}{\partial z}\right)=\frac{\partial}{\partial t}h+\frac{\omega}{2}\frac{\partial}{\partial\Theta}h \tag{B.2}$$

The film thickness and its derivatives with respect to t and Θ are

$$h = C + e_x\cos\Theta + e_y\sin\Theta \tag{B.3}$$

$$\frac{\partial h}{\partial t} = \dot{e}_x\cos\Theta + \dot{e}_y\sin\Theta \tag{B.4}$$

$$\frac{\partial h}{\partial\Theta} = -e_x\sin\Theta + e_y\cos\Theta \tag{B.5}$$

Substitution of B.4 and B.5 in B.2 leads to the following equation.

$$\frac{1}{R^2}\frac{\partial}{\partial\Theta}\left(\frac{h^3}{12\mu}\frac{\partial p}{\partial\Theta}\right)+\frac{\partial}{\partial z}\left(\frac{h^3}{12\mu}\frac{\partial p}{\partial z}\right)=\left(\dot{e}_x+\frac{\omega}{2}e_y\right)\cos\Theta+\left(\dot{e}_y-\frac{\omega}{2}e_x\right)\sin\Theta \tag{B.6}$$

Equation B.6 is the equation which describes a plain journal bearing. To reduce computational time, the Reynolds equation is simplified by using the short length bearing assumption. The short length bearing model assumes that the lubricant flows in the axial direction, the flow in circumferential direction is neglected. This means that the pressure does not change in circumferential direction on an infinitesimal element. In mathematical terms this means $\frac{\partial p}{\partial\Theta} \cong 0$. Applying the short length bearing assumption and substitution of equation B.3 in equation B.6 leads to

$$\frac{\partial}{\partial z}\left(\frac{(C+e_x\cos\Theta+e_y\sin\Theta)^3}{12\mu}\right)\frac{\partial p}{\partial z}=\left(\dot{e}_x+e_y\frac{\omega}{2}\right)\cos\Theta+\left(\dot{e}_y-e_x\frac{\omega}{2}\right)\sin\Theta \tag{B.7}$$

Equation B.7 can be integrated twice with respect to z to obtain an equation for the pressure in the fluid film.

$$p\left(\Theta, z, t\right) - p_a = 6\mu \frac{\left(\dot{e}_x + e_y \frac{\omega}{2}\right)\cos\Theta + \left(\dot{e}_y - e_x \frac{\omega}{2}\right)\sin\Theta}{\left(C + e_x \cos\Theta + e_y \sin\Theta\right)^3} \left(z^2 - \left(\frac{L}{2}\right)^2\right) \tag{B.8}$$

The $-\left(\frac{L}{2}\right)^2$ term in the above equation is introduced to meet the boundary conditions of the pressure at the sides of the bearing in axial direction; the pressure at $z = \pm\frac{L}{2}$ should be equal to the ambient pressure p_a. Equation B.8 gives the film pressure at a point defined by $-\frac{L}{2} \leq z \leq \frac{L}{2}$ in the axial direction and $0 \leq \Theta \leq 2\pi$ in circumferential direction when the position and speed of the shaft is known.

B.2.2 Forces acting on the journal

The force in X and Y directions performed by the pressure of the fluid film on the journal can be calculated by integrating the film pressure equation with respect to z and Θ. Integration of equation B.8 with respect to z can be done analytically.

$$\begin{aligned} \int_{-\frac{L}{2}}^{\frac{L}{2}} p\left(\Theta, z, t\right)\, dz = &\left[6\mu \frac{\left(\dot{e}_x + e_y \frac{\omega}{2}\right)\cos\Theta + \left(\dot{e}_y - e_x \frac{\omega}{2}\right)\sin\Theta}{\left(C + e_x \cos\Theta + e_y \sin\Theta\right)^3} \cdot \ldots \right. \\ &\left. \left(\frac{1}{3}z^3 - \left(\frac{L}{2}\right)^2 z\right) + p_a z \right]\Bigg|_{-\frac{L}{2}}^{\frac{L}{2}} \end{aligned} \tag{B.9}$$

$$P\left(\Theta, t\right) = -8\mu \frac{\left(\dot{e}_x + e_y \frac{\omega}{2}\right)\cos\Theta + \left(\dot{e}_y - e_x \frac{\omega}{2}\right)\sin\Theta}{\left(C + e_x \cos\Theta + e_y \sin\Theta\right)^3} \left(\frac{L}{2}\right)^3 + p_a L \tag{B.10}$$

Using the rectangle rule, equation B.10 is numerically integrated to obtain the forces on the journal in x and y directions. With n being the number of steps in which the domain $0 \leq \Theta \leq 2\pi$ is split and where $\Delta\Theta = \frac{2\pi}{n}$, the forces are

$$F_{x,j} = \sum_{k=0}^{n} P\left(k\Delta\Theta, t\right) R_s \Delta\Theta \cos\left(k\Delta\Theta\right) \tag{B.11}$$

$$F_{y,j} = \sum_{k=0}^{n} P\left(k\Delta\Theta, t\right) R_s \Delta\Theta \sin\left(k\Delta\Theta\right) \tag{B.12}$$

B.3 Forces in and on the floating ring bearing

This appendix describes the forces which act on the shaft and floating ring in the floating ring bearing.

B.3.1 Pressure film force

The pressure distribution functions can be integrated with respect to area to obtain a force. Integrating equations 2.2 and 2.3 as described in section B.2.2 results in the forces working on the shaft, inner ring surface and outer ring surface.

This results in forces $F_{x,s}$ and $F_{y,s}$ working on the shaft, the forces $F_{x,r,i}$ and $F_{y,r,i}$ working on the inner area of the floating ring and the forces $F_{x,r,o}$ and $F_{y,r,o}$ working on the outer area of the floating ring. The pressure film forces working on the different surfaces can be calculated with equations B.13 to B.18, in which $\Delta\Theta = \frac{2\pi}{n}$. Since the assumption is made that the pressure film force working on both bodies a oil film is squeezed in between is equal, an average radius is used in calculating the pressure film forces. These average radii are calculated with equations B.19 and B.20.

$$F_{x,s} = \sum_{k=0}^{n} P_{in}\left(k\Delta\Theta, t\right) R_{\text{avg,in}} \Delta\Theta \cos\left(k\Delta\Theta\right) \tag{B.13}$$

$$F_{y,s} = \sum_{k=0}^{n} P_{in}\left(k\Delta\Theta, t\right) R_{\text{avg,in}} \Delta\Theta \sin\left(k\Delta\Theta\right) \tag{B.14}$$

$$F_{x,r,i} = -F_{x,s} \tag{B.15}$$

$$F_{y,r,i} = -F_{y,s} \tag{B.16}$$

$$F_{x,r,o} = \sum_{k=0}^{n} P_{out}\left(k\Delta\Theta, t\right) R_{\text{avg,out}} \Delta\Theta \cos\left(k\Delta\Theta\right) \tag{B.17}$$

$$F_{y,r,o} = \sum_{k=0}^{n} P_{out}\left(k\Delta\Theta, t\right) R_{\text{avg,out}} \Delta\Theta \sin\left(k\Delta\Theta\right) \tag{B.18}$$

$$R_{\text{avg,in}} = \frac{R_s + R_{r,i}}{2} \tag{B.19}$$

$$R_{\text{avg,out}} = \frac{R_{r,o} + R_b}{2} \tag{B.20}$$

The net forces working on the shaft and floating ring in x- and y-directions are

$$\begin{bmatrix} F_{x,s,p} \\ F_{y,s,p} \\ F_{x,r,p} \\ F_{y,r,p} \end{bmatrix} = \begin{bmatrix} F_{x,s} \\ F_{y,s} \\ F_{x,r,o} - F_{x,r,i} \\ F_{y,r,o} - F_{y,r,i} \end{bmatrix} \tag{B.21}$$

B.3.2 Gravitational force

Although of minor influence in translational direction, the gravitational effects of the shaft and floating ring are included. The gravitational forces of the shaft and floating ring in the y-direction are:

$$F_{x,s,g} = m_s g \tag{B.22}$$

$$F_{x,r,g} = m_r g \tag{B.23}$$

B.3.3 Unbalance force

Since it is almost impossible to perfectly balance the rotor assembly of a turbocharger, there will always be an unbalance residue. The amplitude of the force generated by the unbalance is a centrifugal force which is described by

$$|F_{s,u}| = mr\omega_s^2 \tag{B.24}$$

In this equation, mr represents the amount of unbalance and has a value in the order of $10^{-8} kg \cdot m$. This unbalance value may be very small, but with the high speeds a turbocharger can achieve, the amplitude of the force can be in the order of 10^1 or $10^2 N$. The direction of the unbalance force is described by the angle β, which is defined by

$$\beta = \int_0^t \omega_s \left(t\right) dt \tag{B.25}$$

The equations which describe the unbalance forces are

$$F_{x,s,u} = mr\omega_s^2 cos\left(\beta\right) \tag{B.26}$$

$$F_{y,s,u} = mr\omega_s^2 sin\left(\beta\right) \tag{B.27}$$

B.3.4 Viscous drag force

The shear stress between two surfaces is described by equation B.28. In this equation, τ is the shear stress and du is the difference in speed between the two surfaces.

$$\tau = \mu \frac{du}{dh} \tag{B.28}$$

The terms in equation B.28 can be substituted with terms related to floating ring bearings. This results in equation B.29 for the shear stress in the inner film and equation B.30 for the shear stress in the outer film.

$$\tau_{in} = \mu_{in} \frac{\omega_r R_{r,i} - \omega_s R_s}{C_i + \left(e_{x,r} - e_{x,s}\right) cos\left(\Theta\right) + \left(e_{y,r} - e_{y,s}\right) sin\left(\Theta\right)} \tag{B.29}$$

$$\tau_{out} = \mu_{out} \frac{\omega_r R_{r,o}}{C_o + e_{x,r} cos\left(\Theta\right) + e_{y,r} sin\left(\Theta\right)} \tag{B.30}$$

Multiplying the shear stress by $sin\left(\Theta\right)$ and integrate it over the area it works on, results in the viscous drag force in the x-direction. Multiplying the stress equation by $cos\left(\Theta\right)$ and integrating results in the viscous drag force in y-direction.

$$F_{x,k,v} = \int_0^{2\pi} \tau_k\left(\Theta\right) sin\left(\Theta\right) d\Theta, \qquad k = \{in, out\} \tag{B.31}$$

$$F_{y,k,v} = \int_0^{2\pi} \tau_k\left(\Theta\right) cos\left(\Theta\right) d\Theta, \qquad k = \{in, out\} \tag{B.32}$$

Appendix C

Measurement equipment details

The details of the measurement equipment which has been used for the experiments are shown in this appendix.

Table C.1: Measurement system

Property	Value
Manufacturer	Müller-BBM
Measurement system	PAK Mobile
Software	PAK 5.6 Service release 4

Table C.2: Properties of the eddy-current sensors

Property	Value
Manufacturer	AEC
Type	PU-03A
Measuring range	0-1 mm
Controller	AEC-5503A

Table C.3: Properties of the turbocharger speed sensor

Property	Value
Manufacturer	Picoturn
Type	SM5.7
Measuring range	$200 - 400.000$ RPM
Controller	BM

The calibration factors of the different sensors are shown in table C.4. The output of the eddy-current sensors is influenced by its environment and therefore these sensors have to be calibrated while they are mounted in the demonstrator. The calibration is done by slightly altering the sensor position and measuring the output voltage. This results in measured values at different measurement positions. A linear fit is applied to the measured points to determine the calibration factor.

Table C.4: Calibration factors

Sensor location	Value
End of shaft X	1504 V/m
End of shaft Y	1331 V/m
Floating ring X	4128 V/m
Floating ring Y	3680 V/m
Shaft at ball bearing X	6000 V/m
Shaft at ball bearing Y	4608 V/m
Acceleration sensor cartridge	0.298 pC/m/s^2

Appendix D

Theoretical modeling

D.1 Demonstrator simulation FEM matrices

In this section the finite element matrices for one element are displayed. Matrix D.1 shows the mass matrix of a shaft element and D.2 shows the shaft stiffening matrix of an element. Matrices D.3 and D.4 are respectively the damping and stiffness matrices of a shaft element. [5]

$$M_s = \frac{\rho A L}{420} \begin{bmatrix} 156 & 22L & 0 & 0 & 54 & -13L & 0 & 0 \\ 22L & 4L^2 & 0 & 0 & 13L & -3L^2 & 0 & 0 \\ 0 & 0 & 156 & 22L & 0 & 0 & 54 & -13L \\ 0 & 0 & 22L & 4L^2 & 0 & 0 & 13L & -3L^2 \\ 54 & 13L & 0 & 0 & 156 & -22L & 0 & 0 \\ -13L & -3L^2 & 0 & 0 & -22L & 4L^2 & 0 & 0 \\ 0 & 0 & 54 & 13L & 0 & 0 & 156 & -22L \\ 0 & 0 & -13L & -3L^2 & 0 & 0 & -22L & 4L^2 \end{bmatrix} \tag{D.1}$$

$$M_{ss} = \frac{\rho I}{30L} \begin{bmatrix} 36 & 3L & 0 & 0 & -36 & 3L & 0 & 0 \\ 3L & 4L^2 & 0 & 0 & -3L & -L^2 & 0 & 0 \\ 0 & 0 & 36 & 3L & 0 & 0 & -36 & 3L \\ 0 & 0 & 3L & 4L^2 & 0 & 0 & -3L & -L^2 \\ -36 & -3L & 0 & 0 & 36 & -3L & 0 & 0 \\ 3L & -L^2 & 0 & 0 & -3L & 4L^2 & 0 & 0 \\ 0 & 0 & -36 & -3L & 0 & 0 & 36 & -3L \\ 0 & 0 & 3L & -L^2 & 0 & 0 & -3L & 4L^2 \end{bmatrix} \tag{D.2}$$

$$C_s = \frac{\rho I}{15L} \begin{bmatrix} 0 & 0 & 36 & 3L & 0 & 0 & -36 & 3L \\ 0 & 0 & 3L & 4L^2 & 0 & 0 & -3L & -L^2 \\ -36 & -3L & 0 & 0 & 36 & -3L & 0 & 0 \\ -3L & -4L^2 & 0 & 0 & 3L & L^2 & 0 & 0 \\ 0 & 0 & -36 & -3L & 0 & 0 & 36 & -3L \\ 0 & 0 & 3L & -L^2 & 0 & 0 & -3L & 4L^2 \\ 36 & 3L & 0 & 0 & -36 & 3L & 0 & 0 \\ -3L & L^2 & 0 & 0 & 3L & -4L^2 & 0 & 0 \end{bmatrix} \tag{D.3}$$

$$K_s = \frac{EI}{L^3} \begin{bmatrix} 12 & 6L & 0 & 0 & -12 & 6L & 0 & 0 \\ 6L & 4L^2 & 0 & 0 & -6L & 2L^2 & 0 & 0 \\ 0 & 0 & 12 & 6L & 0 & 0 & -12 & 6L \\ 0 & 0 & 6L & 4L^2 & 0 & 0 & -6L & 2L^2 \\ -12 & -6L & 0 & 0 & 12 & -6L & 0 & 0 \\ 6L & 2L^2 & 0 & 0 & -6L & 4L^2 & 0 & 0 \\ 0 & 0 & -12 & -6L & 0 & 0 & 12 & -6L \\ 0 & 0 & 6L & 2L^2 & 0 & 0 & -6L & 4L^2 \end{bmatrix} \tag{D.4}$$

D.2 Sensitivity analysis waterfall plots

In this appendix the waterfall plots of the motion of the shaft in x-direction are shown which are obtained with the simulations done for the sensitivity analysis. Table D.1 shows the values of the parameters which have been altered. Figures D.1 to D.6 show the waterfall plots resulting from the simulations.

Table D.1: Parameter values used in the point mass simulation of section 4.2

Simulation	Reference simulation value	Simulation value
Reference	-	-
Larger L_i	4mm	7mm
Larger L_o	7mm	10.5mm
Larger C_i	15μm	25μm
Smaller C_o	36μm	25μm
Lower μ_i, μ_o	0.012Pa·s	0.0038Pa·s

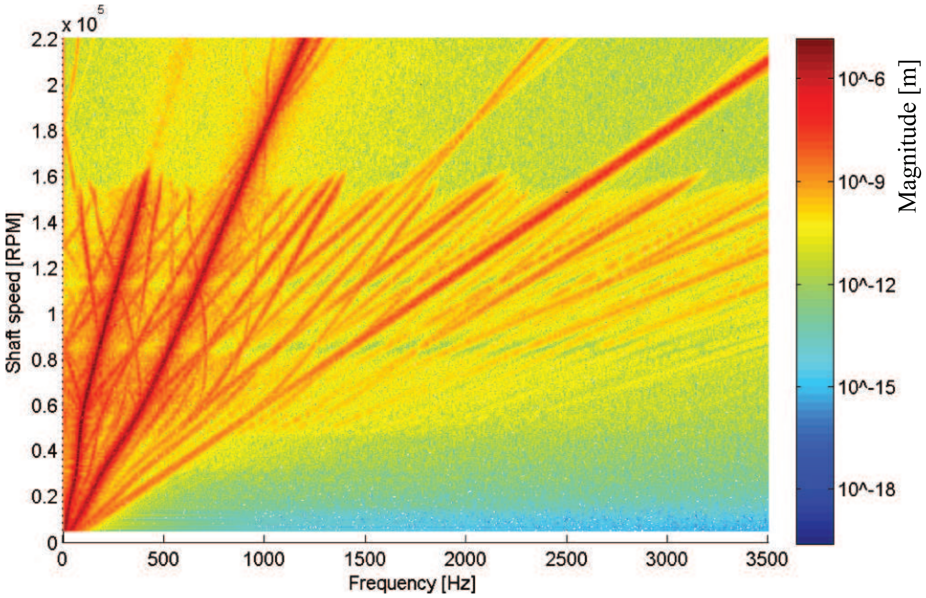

Figure D.1: Reference simulation

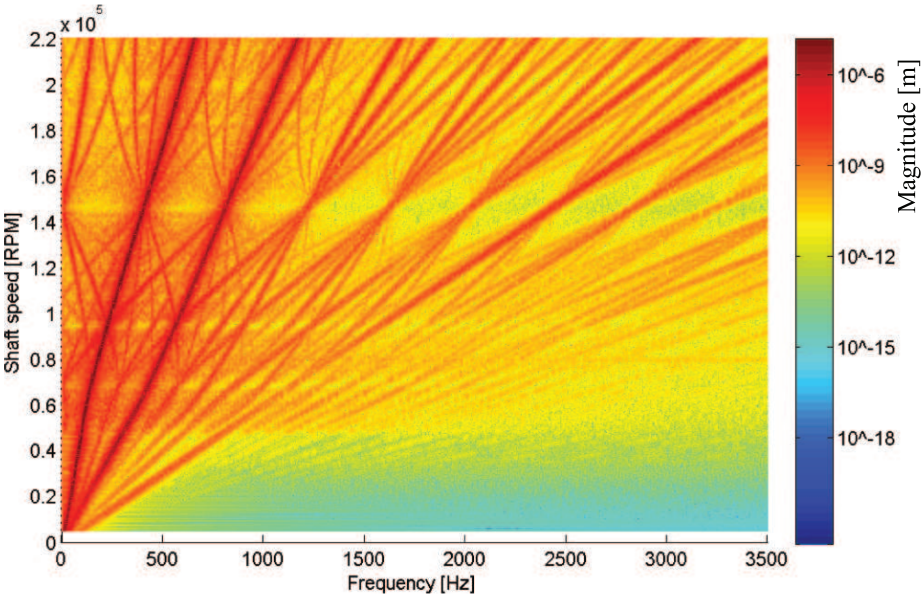

Figure D.2: Point mass simulation with an increased inner bearing width

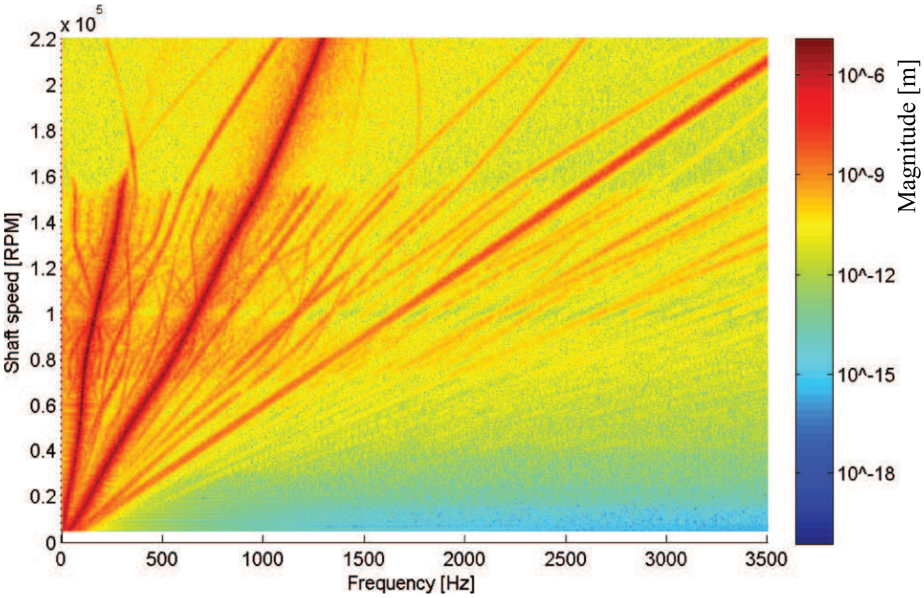

Figure D.3: Point mass simulation with an increased outer bearing width

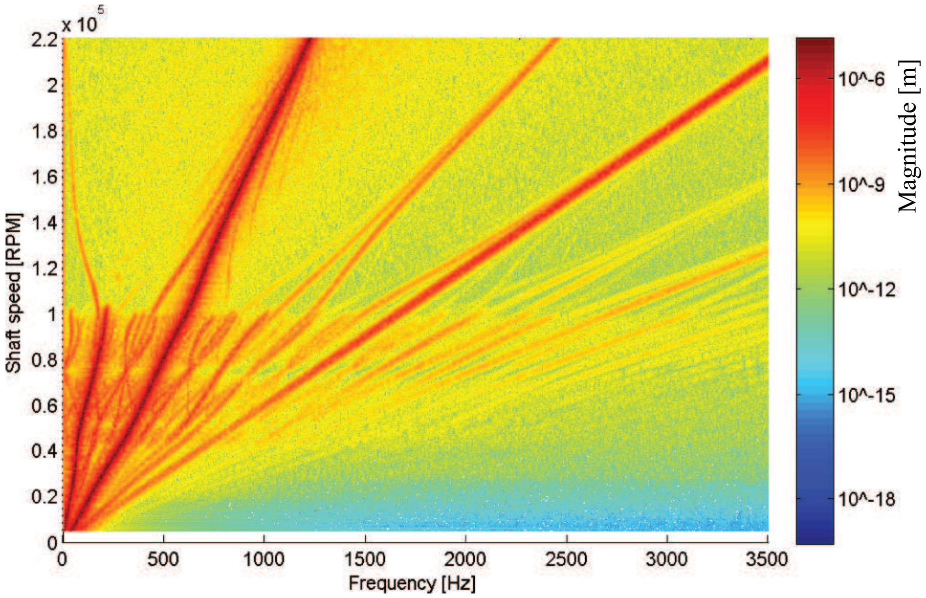

Figure D.4: Point mass simulation with an increased inner gap

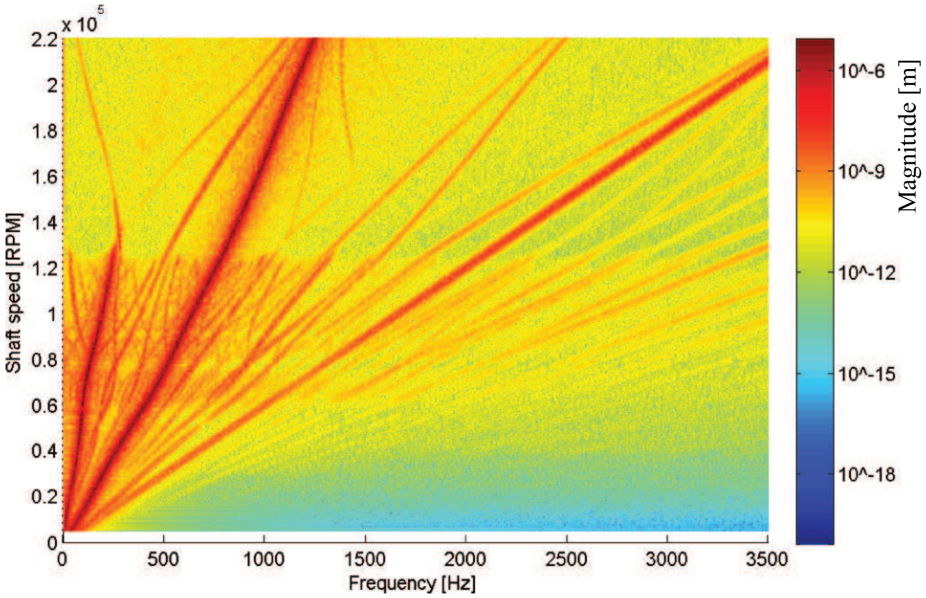

Figure D.5: Point mass simulation with a decreased outer gap

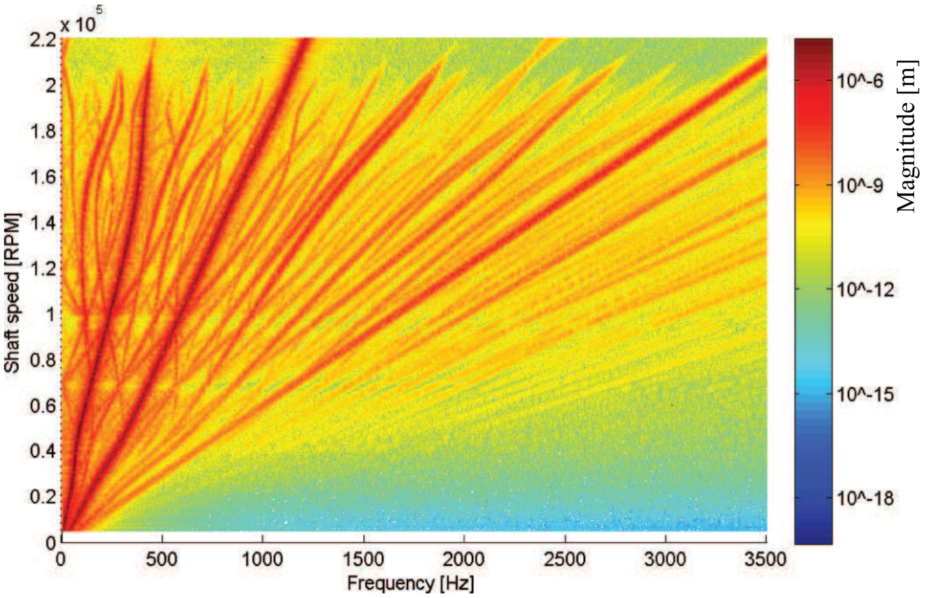

Figure D.6: Point mass simulation with decreased oil viscosity

Appendix E

Additional experimental results

In this section additional measurements results are shown. Figures E.1 and E.2 show the waterfall plots of the shaft motion in y-direction. The characteristics of these waterfall plots are the same as the waterfall plots of the motion in x-direction.

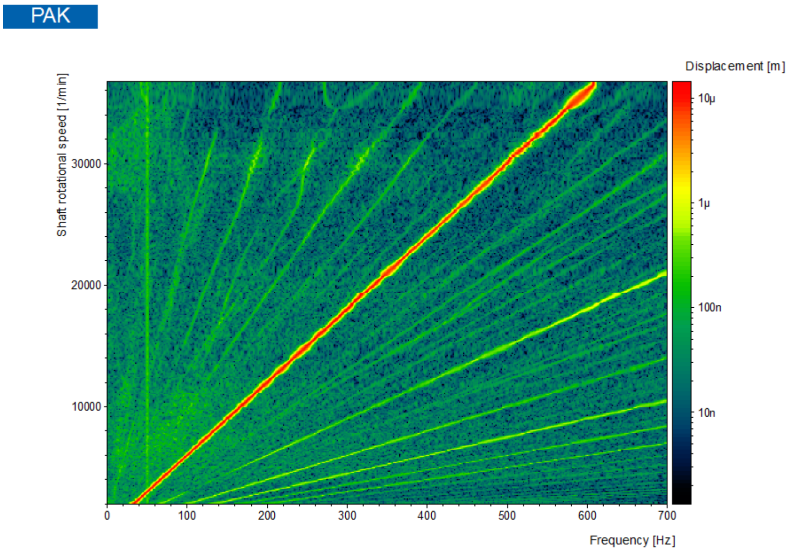

Figure E.1: Waterfall plot of the displacement of the shaft close to the ball bearing in y-direction

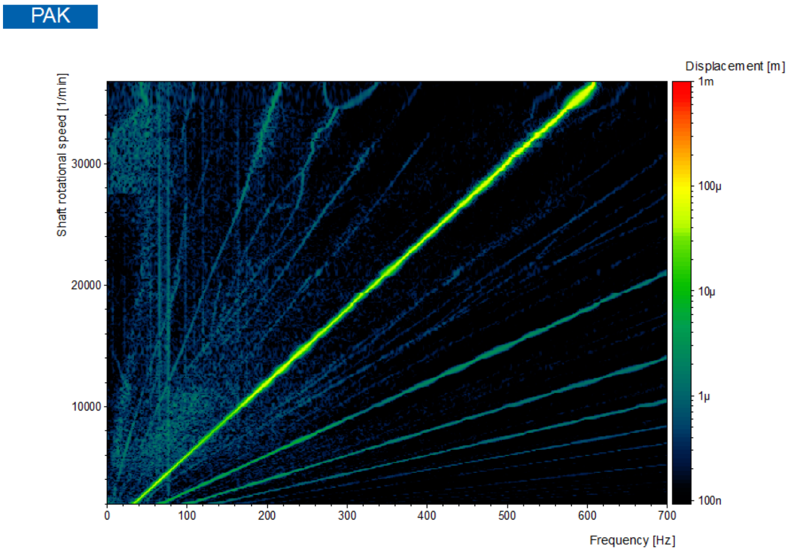

Figure E.2: Waterfall plot of the displacement of the shaft at the end of the shaft in y-direction